2017

High resolution mass spectrometry to explore molecular-level understanding of biomass pyrolysis

Carolyn P. Hutchinson
Iowa State University

High resolution mass spectrometry to explore molecular-level understanding of biomass pyrolysis

by

Carolyn P. Hutchinson

A dissertation submitted to the graduate faculty

in partial fulfillment of the requirements for the degree of

DOCTOR OF PHILOSOPHY

Major: Analytical Chemistry

Program of Study Committee:
Young-Jin Lee, Major Professor
Robert S. Houk
Emily Smith
Javier Vela
Wenyu Huang

The student author and the program of study committee are solely responsible for the content of this dissertation. The Graduate College will ensure this dissertation is globally accessible and will not permit alterations after a degree is conferred.

Iowa State University

Ames, Iowa

2017

TABLE OF CONTENTS

NOMENCLATURE

(+)	Positive Mode
(-)	Negative Mode
APCI	Atmospheric Pressure Chemical Ionization
APPI	Atmospheric Pressure Photoionization
BIO-OIL	Biomass Pyrolysis Oils
dAPCI	Dopant-Assisted Atmospheric Pressure Chemical Ionization
DBE	Double Bond Equivalency
ESI	Electrospray Ionization
FT-ICR	Fourier Transform Ion Cyclotron Resonance
GC	Gas Chromatography
HRMS	High Resolution Mass Spectrometry
MS	Mass Spectrometer
M/Z	Mass-to-Charge
TOF	Time-of-Flight
µPy	Micropyrolysis
PAH	Polyaromatic Hydrocarbon
PTFE	Polytetrafluoroethylene (Teflon)

ACKNOWLEDGMENTS

I would like to foremost thank my major professor, Young-Jin Lee, for the opportunity to join his group and this project in particular, allowing me to grow and succeed as a graduate student and an analytical chemist. I would also like to thank my committee members, Sam Houk, Emily Smith, Javier Vela, and Wenyu Huang. Without their guidance and support, this research and my success would not have been possible.

In addition, I would also like to thank my colleagues in the Lee group, especially Erica Dalluge and Evan Larson, for their insightful discussions, helpful suggestions, and much-needed support. I would also like to thank the Brown group for their many insightful discussions over the years. I also would like to extend my gratitude to the undergraduates who have helped me along the way, both in research and in growing as a mentor; in particular, I would like to thank Kaitlin Heinen and Jim Frank.

I would also like to thank the individuals in the Q*GSA, oSTEM ISU, and the Pride Summit for their encouragement and support. In particular, Nicci Port and Brad Freihoefer have given me opportunities which I never dreamed could be possible. Without these individuals, as well as other friends and mentors, my time at Iowa State would have been less rich and fulfilling. I have truly learned the meaning of looking around as well as up for mentors through these organizations.

I would like to thank Geoffrey Klein at Christopher Newport University for sparking my interest in analytical chemistry and especially mass spectrometry in the first place. He has remained a role model throughout my undergraduate and graduate career,

and I would not be where I am today if I had not met him. I would also like to thank the other educators who have encouraged my passions.

I would also like to thank my family for their unwavering love, confidence, and encouragement, no matter life has thrown at me over the last six years. I would like to thank Kelly Grzech for her steadfast friendship over the past two decades and for encouraging me even at the hardest times. Finally, I would thank Zack Ruff for his friendship, his love, his partnership, and his unwavering belief in my ability to succeed—which has helped me get here today.

ABSTRACT

In recent decades, thermochemical conversion of lignocellulosic biomass has gained popularity as a means to supplement or replace petroleum. Fast pyrolysis bio-oils have emerged as a potential source for transportation fuels and value-added chemicals. A lack of molecular-level understanding has stalled progress toward fast pyrolysis as an economically feasible option. To address this roadblock, this research focuses on high resolution mass spectrometry (HRMS) applications to molecular-level understanding of biomass pyrolysis.

Negative mode atmospheric pressure photionization (APPI) and Fourier transform ion cyclotron resonance (FTICR) mass spectrometry (MS) are applied to nitrogen-rich switchgrass bio-oil and gasification tar for characterization and comparison. When compared with (+) APPI and positive and negative electrospray ionization, (-) APPI ionizes a wider range of compounds and provides a more comprehensive overview of the compounds present. The compounds accessed by (-) APPI are also generally accessed by one of the other ionization methods, but (-) APPI ionizes them with less specificity for a single group of compounds.

A novel HRMS system for biomass pyrolysis analysis is introduced. Gas chromatography is coupled with dopant-assisted atmospheric pressure chemical ionization (dAPCI) for analysis by a time-of-flight mass spectrometer (TOF MS). Ammonia gas serves as the dopant. The ammonium adduct ions prevent the fragmentation observed in dopant-free APCI. Water plays a crucial role in the ionization

process; thus, a humidification system for dAPCI is created to provide constant humidity. All compounds demonstrate improved signal and ionization with controlled humidity.

A micropyrolyzer (μPy) is attached to the dAPCI-TOF MS system and thin-film glucose labeled on carbons 1, 3, or 6 with ^{13}C is pyrolyzed and analyzed in real-time to study reaction pathways. The real-time data acquired validates or invalidates previously proposed mechanisms. Alternative reaction pathways are suggested when the mechanism is invalidated. Glyceraldehyde, a C3 compound difficult to detect with traditional analytical methods, is shown to play an important role.

Single particles of whole biomass are pyrolyzed and analyzed with the μPy-dAPCI-TOF MS for a unique comparison of herbaceous, softwood, and hardwood lignocellulosic biomass. Different temporal profiles for holocellulose and lignin decomposition products are observed. A series of the most dominant phenolic compounds occurs at *m/z* 133, 163, and 193, related to the monolignol monomers. Smaller, highly oxygenated compounds are more abundant for the hemicellulose-rich herbaceous feedstock whereas levoglucosan is dominant in both hardwood and softwood.

CHAPTER 1

INTRODUCTION

A (Brief) Discussion of Fast Pyrolysis Biofuel Analysis

As global demands for energy continue to rise dramatically, there is increased interest in finding a viable replacement for fossil fuels. Fast pyrolysis of lignocellulosic biomass is one method which has garnered recent attention.[1-2] The thermochemical conversion process of fast pyrolysis occurs at a moderate temperature (400-600 °C) in the absence of oxygen in a short time frame (a few seconds) and produces high yields (>60 wt%) of condensable vapors, or bio-oils.[2-5] These bio-oils can then be upgraded to drop-in transportation fuels or commodity chemicals.[6-7] As a transportation fuel, bio-oil offers low NO_x and SO_x emissions as well as reducing net carbon emissions compared to petroleum fuels.[8] However, due to the oxygen content in lignin and holocellulose in the original biomass, bio-oil suffers from a number of problems not present in petroleum: it has an extremely high water and oxygen content, many of the compounds are polar, it is very acidic and corrosive, and it is very unstable and reactive.[9] As such, long term storage is difficult, and bio-oil requires extensive upgrading to serve as a feasible transportation fuel.[2, 8, 10]

Bio-oil itself is an extremely complex mixture. that typically contains both a water-soluble and a water-insoluble phase. Both of these phases contain both volatile and non-volatile species. Analyzing such a complex mixture in one step is a daunting challenge. Standard characterization relies largely on bulk property measurements, such as pH, water content, elemental analysis, density, viscosity, and heating values.[5, 9]

Structural and molecular data is commonly achieved using Fourier transform infrared (FTIR) spectroscopy, nuclear magnetic resonance (NMR), and gas chromatography coupled with mass spectrometry (GC-MS).[11-13] However, these techniques suffer from significant limitations. FTIR and NMR provide averaged information on the functional groups present.[11] GC-MS is limited to volatile compounds that can survive the time it takes to elute from the GC column, typically 45-60 minutes. ; this means that metastable intermediates and thermally labile compounds are lost or suppressed in addition to non-volatile species remaining undetected. Even when the data is collected directly from a pyrolyzer, it is only analyzed after separation and loss of these compounds. Additionally, electron impact (EI) ionization is a highly energetic process which creates extensive fragmentation. This fragmentation allows for reliable identification with the use of a database. However, if the compound is fragile and fragments too extensively, it will be unidentifiable using the database or will be misidentified. Compounds which are not found in the database and do not have commercially available standards for validation also cannot be identified with this method. This is especially problematic for compounds derived from holocellulose (e.g., levoglucosan, furans). High resolution mass spectrometry (HRMS) techniques have been adapted to address some of these shortcomings.

Atmospheric Pressure Ionization and High Resolution Mass Spectrometry

HRMS coupled with appropriate ionization methods has emerged as an alternative for whole bio-oil analysis. Much of whole bio-oil analysis has been adapted from methods for analyzing petroleum oils which use atmospheric pressure ionization (API)

techniques coupled with HRMS, proving that bio-oils can be handled with established petroleomic procedures. API techniques are typically most successful with biofuels due to their ability to ionize a wide range of compounds, especially non-volatiles unaccessed by GC-MS. However, these sources tend to have selectivity towards certain groups due to their ionization mechanisms. For example, negative mode electrospray ionization (ESI) strongly favors compounds with acidic protons due to its ionization mechanism by which a molecule is deprotonated; it is less effective for compounds which do not have acidic protons (e.g., hydrocarbons). This makes (-) ESI an excellent ionization source for bio-oil which contains many species with acidic protons; however, it will underestimate the presence of neutral and basic species present. Dopants can be used to alleviate some of this selectivity. In any API-HRMS analysis, the selectivity of the ionization technique must be taken into careful consideration when selecting an ionization source.

Our group has had great success in analyzing pyrolysis products with API-HRMS. Smith and Lee successfully used laser desportion ionization (LDI)-linear ion trap-Orbitrap to determine the chemical compositions of over 100 compounds in loblolly pine bio-oil, which were found to be mostly non-volatile phenolic compounds.[14] Smith et al. compared (-) ESI on three different HRMS instruments for analysis of red oak bio-oil, finding the (-) ESI is typically dominated by low mass (*m/z* 100-250) compounds.[15] (-) ESI was able to effectively characterize compounds from the pyrolysis of holocellulose, and they were able to assign chemical compositions to over 800 species. Cole et al. combined LDI, (-) ESI, and positive-mode atmospheric pressure photoionization (APPI) to analyze switchgrass biochar.[16] Fast pyrolysis biochar was found to contain compounds from the decomposition of lignin and of holocellulose similar to fast pyrolysis bio-oil

while gasification char was found to contain polyaromatic hydrocarbons (PAHs). Smith et al. utilized (-) ESI and (+) APPI coupled with HRMS to study bio-oil aging.[17] Lee et al. analyzed lipids extracted from algal bio-oils using positive mode ESI, APPI, APCI, and MALDI.[18] Cole et al. used (-) ESI, (+) ESI, and (+) APPI coupled with Orbitrap mass spectrometry (MS) to identify nitrogen-containing species in switchgrass bio-oil, successfully identifying nearly 300 nitrogen-containing compounds, including pyridine- and imidazole-based compounds.[19] Finally, Cole and Lee applied a novel system that couples a micropyrolyzer with GC to a time-of-flight mass spectrometry (TOF MS) to successfully evaluate *in situ* catalytic fast pyrolysis.[20]

In addition to the work by the Lee group, the Kenttämaa group at Purdue University has had seen success using API-HRMS to analyze pyrolysis products. A large number of projects were performed on a ThermoFinnigan LTQ linear quadrupole ion trap (LQIT) and utilize its tandem MS capabilities. Despite doing a significant amount of API-MS work,[21-25] little has been conducted with HRMS. Owen et al. characterized lignin degradation products with FT-ICR MS.[26] Jarrell et al. used LQIT/FT-ICR (-) ESI with a hydroxide dopant to characterize lignin.[27] Several other works attach a pyroprobe reactor to this system in order to study pyrolysis products. Hurt et al. and Degenstein et al. used this system to analyze cellulose and carbohydrate pyrolysis; Hurt et al. used the FT-ICR component while Degenstein et al. did not.[28-29] Degenstein et al. also used this pyroprobe-APCI-LQIT system to analyze ^{13}C-labeled cellobioses.[30]

Observing and Studying Kinetics in Fast Pyrolysis

A major roadblock to the forward progress of fast pyrolysis bio-oils has been a lack of experimentally validated fundamental understanding of the thermochemical conversion processes.[8] In order to solve this, the investigation of fast pyrolysis kinetics has been underway for over three decades now though knowledge remains very limited. Since cellulose is the least complex component of biomass and usually the most abundant building block (up to 60 wt%), it has become the most widely studied feedstock for kinetics.[1-2, 8, 31-33] Until recently, kinetics was only represented using a lump-sum model, such as the Broido-Shafizadeh model (Scheme 1).[31-33] As seen in Scheme 1, cellulose first forms an "active cellulose" form which then decomposes to produce products in one of two lumped categories: volatiles (i.e., bio-oil) or solid and gas (i.e., char and non-condensable gases). These lump-sum models are able to adequately explain volatilization rates and overall yields, but they fail to explain the decomposition pathways in any detail. These models also neglect important phenomena such as phase transitions, conduction effects, or aerosol formation/ejection. The simplification in these models results in extensive disagreement between the kinetics parameters obtained by different groups over the last several decades.[31-33]

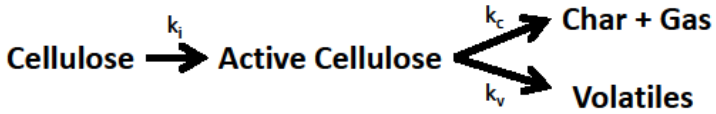

Scheme 1. The Broido-Shafizadeh lump-sum model.

Several recent improvements in pyrolysis have provided breakthroughs in the fundamental understanding of the pyrolysis process. Using a focused xenon lamp, Lédé and coworkers developed radiant flash pyrolysis which revealed the presence of non-volatile oligomers from intermediates when immediately quenched.[34] Dauenhauer and coworkers used high speed photography to visualize aerosol ejection from molten cellulose as well as a wetting effect in crystalline cellulose particles at fast pyrolysis temperatures (around 500 °C).[35-36] Most recently, the Dauenhauer group developed a thermal pulsing reactor, named the Pulse-Heated Analysis of Solid Reactions (PHASR). The PHASR allows for precise control of heating time on a millisecond timescale and analyzes the product distributions with GC-MS.[37] This system was successfully applied to cellulose pyrolysis and demonstrated the size-dependence of reaction kinetics (i.e., reaction-limited to transport-limited reaction kinetics at 60 μm thickness) and temperature-dependent change of reaction mechanisms (i.e., from chain-end cleavage to intra-chain cleavage at the temperature of 467 °C).

In light of these breakthroughs, there were several important advances in fast pyrolysis kinetics. These advances help to address the shortcomings of the lump-sum model revealed by the discoveries of the last 15 years. Seshadri and Westmoreland modeled glucose pyrolysis using gas-phase quantum-chemistry and statistical-mechanical calculations.[38] Agarwal et al. also performed ab initio simulations for cellulose pyrolysis, revealing important free energy barriers that explain the preferential formation of levoglucosan.[39] Vinu and Broadbelt proposed a mechanistic model for cellulose pyrolysis that utilizes a complex network of elementary reactions; this model was refined and fitted to experimental data by Zhou et al. in 2014.[40-44] Paulsen et al. and Mettler et al.

developed thin-film pyrolysis to explore the role of sample dimension in pyrolysis kinetics.[45-46] Despite these recent technical and mechanistic advances, there currently is no tool available that can monitor the pyrolysis reaction product in real-time, which would allow for true kinetics to be elucidated.

Research Objective and Approach

This research aims to further novel applications of API-HRMS for the analysis of fast pyrolysis biofuels. Novel ionization techniques and analytical platforms are investigated to provide information on fast pyrolysis and its products that is not achievable with more traditional analysis, such as GC-MS. These API-HRMS systems provide unparalleled abilities for molecular-level observations. For example, the ability to observe isotopically labeled products from glucose pyrolysis in real time provides evidence for reaction pathways which were not previously proposed. The information from this project can be used to improve fast pyrolysis processes, aid in feedstock selection, and help optimize downstream refining. This work takes the API-HRMS methodology further by applying it not only to carbohydrates but to a variety of whole biomass in a unique comparison of the pyrolysis behavior of herbaceous, hardwood, and softwood biomasses.

Dissertation Organization

This dissertation is organized into six chapters and one appendix. The first chapter (above) provides an introduction to fast pyrolysis and the analysis of biofuels, atmospheric pressure ionization (API) coupled with high resolution mass spectrometry

(HRMS) for the improved molecular-level analysis of these biofuels, and the current state of fast pyrolysis kinetics. The second chapter compares negative mode atmospheric pressure photoionization, a relatively new API technique, to more established techniques such as negative and positive mode electrospray ionization and positive mode atmospheric pressure photoionization for nitrogen-rich switchgrass biofuels in order to find an ionization technique that is able to ionize a wide range of compounds in Fourier transform ion cyclotron resonance MS. The third through fifth chapters and the appendix discuss a novel API-HRMS system which couples a micropyrolyzer (μPy) to a high resolution time-of-flight mass spectrometer (TOF MS) using a gas chromatograph (GC) with and without chromatographic separation and a dopant-assisted atmospheric pressure chemical ionization (dAPCI) source interface. Chapter three discusses the importance of humidity in the GC-[d]APCI system and introduces a setup built in-house to provide constant humidity to the source. Chapter four explores primary reaction pathways of glucose pyrolysis utilizing this μPy-[GC]-dAPCI-TOF MS system to study the behavior of glucose which has been selectively labeled with ^{13}C. Chapter five explores the pyrolysis behavior of herbaceous, hardwood, and softwood whole biomass on the single particle level in real time. The sixth chapter provides a general discussion of the works presented here, general conclusions, and future directions and applications for the μPy-[GC]-dAPCI-TOF MS system. The appendix discusses an application of the μPy-dAPCI-TOF MS system to carbohydrate pyrolysis to probe the pyrolysis behavior of glucose-based carbohydrates in real time.

References

1. Bridgwater, A. V., Review of fast pyrolysis of biomass and product upgrading. *Biomass Bioenerg* **2012,** *38*, 68-94.

2. Huber, G. W.; Iborra, S.; Corma, A., Synthesis of transportation fuels from biomass: Chemistry, catalysts, and engineering. *Chem Rev* **2006,** *106* (9), 4044-4098.

3. Czernik, S.; Bridgwater, A. V., Overview of applications of biomass fast pyrolysis oil. *Energ Fuel* **2004,** *18* (2), 590-598.

4. Mohan, D.; Pittman, C. U.; Steele, P. H., Pyrolysis of wood/biomass for bio-oil: A critical review. *Energ Fuel* **2006,** *20* (3), 848-889.

5. Bridgwater, A. V.; Czernik, S.; Meier, D.; Piskorz, J., Fast pyrolysis technology. *Biomass: A Growth Opportunity in Green Energy and Value-Added Products, Vols 1 and 2* **1999**, 1217-1223.

6. Vispute, T. P.; Zhang, H. Y.; Sanna, A.; Xiao, R.; Huber, G. W., Renewable Chemical Commodity Feedstocks from Integrated Catalytic Processing of Pyrolysis Oils. *Science* **2010,** *330* (6008), 1222-1227.

7. Regalbuto, J. R., Cellulosic Biofuels-Got Gasoline? *Science* **2009,** *325* (5942), 822-824.

8. Mettler, M. S.; Vlachos, D. G.; Dauenhauer, P. J., Top ten fundamental challenges of biomass pyrolysis for biofuels. *Energ Environ Sci* **2012,** *5* (7), 7797-7809.

9. Gellerstedt, G.; Li, J. B.; Eide, I.; Kleinert, M.; Barth, T., Chemical Structures Present in Biofuel Obtained from Lignin. *Energ Fuel* **2008,** *22* (6), 4240-4244.

10. DOE In *Conversion Technologies for Advanced Biofuels: Preliminary Roadmap & Workshop Report*, Arlington, VA, Arlington, VA, 2011.

11. Pan, S. B.; Pu, Y. Q.; Foston, M.; Ragauskas, A. J., Compositional Characterization and Pyrolysis of Loblolly Pine and Douglas-fir Bark. *Bioenerg Res* **2013,** *6* (1), 24-34.

12. White, J. E.; Catallo, W. J.; Legendre, B. L., Biomass pyrolysis kinetics: A comparative critical review with relevant agricultural residue case studies. *J Anal Appl Pyrol* **2011,** *91* (1), 1-33.

13. Mettler, M. S.; Mushrif, S. H.; Paulsen, A. D.; Javadekar, A. D.; Vlachos, D. G.; Dauenhauer, P. J., Revealing pyrolysis chemistry for biofuels production: Conversion of cellulose to furans and small oxygenates. *Energ Environ Sci* **2012,** *5* (1), 5414-5424.

14. Smith, E. A.; Lee, Y. J., Petroleomic Analysis of Bio-oils from the Fast Pyrolysis of Biomass: Laser Desorption Ionization-Linear Ion Trap-Orbitrap Mass Spectrometry Approach. *Energ Fuel* **2010,** *24*, 5190-5198.

15. Smith, E. A.; Park, S.; Klein, A. T.; Lee, Y. J., Bio-oil Analysis Using Negative Electrospray Ionization: Comparative Study of High-Resolution Mass Spectrometers and Phenolic versus Sugaric Components. *Energ Fuel* **2012,** *26* (6), 3796-3802.

16. Cole, D. P.; Smith, E. A.; Lee, Y. J., High-Resolution Mass Spectrometric Characterization of Molecules on Biochar from Pyrolysis and Gasification of Switchgrass. *Energ Fuel* **2012,** *26* (6), 3803-3809.

17. Smith, E. A.; Thompson, C.; Lee, Y. J., Petroleomic Characterization of Bio-Oil Aging using Fourier-Transform Ion Cyclotron Resonance Mass Spectrometry. *B Korean Chem Soc* **2014,** *35* (3), 811-814.

18. Lee, Y. J.; Leverence, R. C.; Smith, E. A.; Valenstein, J. S.; Kandel, K.; Trewyn, B. G., High-Throughput Analysis of Algal Crude Oils Using High Resolution Mass Spectrometry. *Lipids* **2013,** *48* (3), 297-305.

19. Cole, D. P.; Smith, E. A.; Dalluge, D.; Wilson, D. M.; Heaton, E. A.; Brown, R. C.; Lee, Y. J., Molecular characterization of nitrogen-containing species in switchgrass bio-oils at various harvest times. *Fuel* **2013,** *111*, 718-726.

20. Cole, D. P.; Lee, Y. J., Effective evaluation of catalytic deoxygenation for in situ catalytic fast pyrolysis using gas chromatography-high resolution mass spectrometry. *J Anal Appl Pyrol* **2015,** *112*, 129-134.

21. Amundson, L. M.; Gallardo, V. A.; Vinueza, N. R.; Owen, B. C.; Reece, J. N.; Habicht, S. C.; Fu, M. K.; Shea, R. C.; Mossman, A. B.; Kenttamaa, H. I., Identification and Counting of Oxygen Functionalities and Alkyl Groups of Aromatic Analytes in Mixtures by Positive-Mode Atmospheric Pressure Chemical Ionization Tandem Mass Spectrometry Coupled with High-Performance Liquid Chromatography. *Energ Fuel* **2012,** *26* (5), 2975-2989.

22. Haupert, L. J.; Owen, B. C.; Marcum, C. L.; Jarrell, T. M.; Pulliam, C. J.; Amundson, L. M.; Narra, P.; Aqueel, M. S.; Parsell, T. H.; Abu-Omar, M. M.; Kenttamaa, H. I., Characterization of model compounds of processed lignin and the lignome by using atmospheric pressure ionization tandem mass spectrometry. *Fuel* **2012,** *95* (1), 634-641.

23. Vinueza, N. R.; Gallardo, V. A.; Klimek, J. F.; Carpita, N. C.; Kenttamaa, H. I., Analysis of xyloglucans by ambient chloride attachment ionization tandem mass spectrometry. *Carbohyd Polym* **2013,** *98* (1), 1203-1213.

24. Vinueza, N. R.; Gallardo, V. A.; Klimek, J. F.; Carpita, N. C.; Kenttamaa, H. I., Analysis of carbohydrates by atmospheric pressure chloride anion attachment tandem mass spectrometry. *Fuel* **2013,** *105*, 235-246.

25. Vinueza, N. R.; Kim, E. S.; Gallardo, V. A.; Mosier, N. S.; Abu-Omar, M. M.; Carpita, N. C.; Kenttamaa, H. I., Tandem mass spectrometric characterization of the conversion of xylose to furfural. *Biomass Bioenerg* **2015,** *74*, 1-5.

26. Owen, B. C.; Haupert, L. J.; Jarrell, T. M.; Marcum, C. L.; Parsell, T. H.; Abu-Omar, M. M.; Bozell, J. J.; Black, S. K.; Kenttamaa, H. I., High-Performance Liquid Chromatography/High-Resolution Multiple Stage Tandem Mass Spectrometry Using Negative-Ion-Mode Hydroxide-Doped Electrospray Ionization for the Characterization of Lignin Degradation Products. *Anal Chem* **2012,** *84* (14), 6000-6007.

27. Jarrell, T. M.; Marcum, C. L.; Sheng, H. M.; Owen, B. C.; O'Lenick, C. J.; Maraun, H.; Bozell, J. J.; Kenttamaa, H. I., Characterization of organosolv switchgrass lignin by using high performance liquid chromatography/ high resolution tandem mass spectrometry using hydroxide-doped negative-ion mode electrospray ionization. *Green Chem* **2014,** *16* (5), 2713-2727.

28. Hurt, M. R.; Degenstein, J. C.; Gawecki, P.; Borton, D. J.; Vinueza, N. R.; Yang, L.; Agrawal, R.; Delgass, W. N.; Ribeiro, F. H.; Kenttamaa, H. I., On-Line Mass Spectrometric Methods for the Determination of the Primary Products of Fast Pyrolysis of Carbohydrates and for Their Gas-Phase Manipulation. *Anal Chem* **2013,** *85* (22), 10927-10934.

29. Degenstein, J. C.; Hurt, M.; Murria, P.; Easton, M.; Choudhari, H.; Yang, L. N.; Riedeman, J.; Carlsen, M. S.; Nash, J. J.; Agrawal, R.; Delgass, W. N.; Ribeiro, F. H.; Kenttamaa, H. I., Mass spectrometric studies of fast pyrolysis of cellulose. *Eur J Mass Spectrom* **2015,** *21* (3), 321-326.

30. Degenstein, J. C.; Murria, P.; Easton, M.; Sheng, H. M.; Hurt, M.; Dow, A. R.; Gao, J. S.; Nash, J. J.; Agrawal, R.; Delgass, W. N.; Ribeiro, F. H.; Kenttamaa, H. I., Fast Pyrolysis of C-13-Labeled Cellobioses: Gaining Insights into the Mechanisms of Fast Pyrolysis of Carbohydrates. *J Org Chem* **2015,** *80* (3), 1909-1914.

31. Burnham, A. K.; Zhou, X. W.; Broadbelt, L. J., Critical Review of the Global Chemical Kinetics of Cellulose Thermal Decomposition. *Energ Fuel* **2015,** *29* (5), 2906-2918.

32. Di Blasi, C., Modeling chemical and physical processes of wood and biomass pyrolysis. *Prog Energ Combust* **2008,** *34* (1), 47-90.

33. Kawamoto, H., Review of Reactions and Molecular Mechanisms in Cellulose Pyrolysis. *Curr Org Chem* **2016,** *20* (23), 2444-2457.

34. Lede, J.; Blanchard, F.; Boutin, O., Radiant flash pyrolysis of cellulose pellets: products and mechanisms involved in transient and steady state conditions. *Fuel* **2002,** *81* (10), 1269-1279.

35. Teixeira, A. R.; Mooney, K. G.; Kruger, J. S.; Williams, C. L.; Suszynski, W. J.; Schmidt, L. D.; Schmidt, D. P.; Dauenhauer, P. J., Aerosol generation by reactive boiling ejection of molten cellulose. *Energ Environ Sci* **2011,** *4* (10), 4306-4321.

36. Teixeira, A. R.; Krumm, C.; Vinter, K. P.; Paulsen, A. D.; Zhu, C.; Maduskar, S.; Joseph, K. E.; Greco, K.; Stelatto, M.; Davis, E.; Vincent, B.; Hermann, R.; Suszynski, W.; Schmidt, L. D.; Fan, W.; Rothstein, J. P.; Dauenhauer, P. J., Reactive Liftoff of Crystalline Cellulose Particles. *Sci Rep-Uk* **2015,** *5*.

37. Krumm, C.; Pfaendtner, J.; Dauenhauer, P. J., Millisecond Pulsed Films Unify the Mechanisms of Cellulose Fragmentation. *Chem. Mater.* **2016,** *28* (9), 3108-3114.

38. Seshadri, V.; Westmoreland, P. R., Concerted Reactions and Mechanism of Glucose Pyrolysis and Implications for Cellulose Kinetics. *J Phys Chem A* **2012,** *116* (49), 11997-12013.

39. Agarwal, V.; Dauenhauer, P. J.; Huber, G. W.; Auerbach, S. M., Ab Initio Dynamics of Cellulose Pyrolysis: Nascent Decomposition Pathways at 327 and 600 degrees C. *J Am Chem Soc* **2012,** *134* (36), 14958-14972.

40. Vinu, R.; Broadbelt, L. J., A mechanistic model of fast pyrolysis of glucose-based carbohydrates to predict bio-oil composition. *Energ Environ Sci* **2012,** *5* (12), 9808-9826.

41. Zhou, X. W.; Nolte, M. W.; Mayes, H. B.; Shanks, B. H.; Broadbelt, L. J., Experimental and Mechanistic Modeling of Fast Pyrolysis of Neat Glucose-Based Carbohydrates. 1. Experiments and Development of a Detailed Mechanistic Model. *Ind Eng Chem Res* **2014,** *53* (34), 13274-13289.

42. Zhou, X. W.; Nolte, M. W.; Shanks, B. H.; Broadbelt, L. J., Experimental and Mechanistic Modeling of Fast Pyrolysis of Neat Glucose-Based Carbohydrates. 2. Validation and Evaluation of the Mechanistic Model. *Ind Eng Chem Res* **2014,** *53* (34), 13290-13301.

43. Mayes, H. B.; Broadbelt, L. J., Unraveling the Reactions that Unravel Cellulose. *J Phys Chem A* **2012,** *116* (26), 7098-7106.

44. Mayes, H. B.; Nolte, M. W.; Beckham, G. T.; Shanks, B. H.; Broadbelt, L. J., The Alpha-Bet(a) of Glucose Pyrolysis: Computational and Experimental Investigations of 5-Hydroxymethylfurfural and Levoglucosan Formation Reveal Implications for Cellulose Pyrolysis. *Acs Sustain Chem Eng* **2014,** *2* (6), 1461-1473.

45. Mettler, M. S.; Paulsen, A. D.; Vlachos, D. G.; Dauenhauer, P. J., Pyrolytic conversion of cellulose to fuels: levoglucosan deoxygenation via elimination and cyclization within molten biomass. *Energ Environ Sci* **2012,** *5* (7), 7864-7868.

46. Paulsen, A. D.; Mettler, M. S.; Dauenhauer, P. J., The Role of Sample Dimension and Temperature in Cellulose Pyrolysis. *Energ Fuel* **2013,** *27* (4), 2126-2134.

CHAPTER 2

EXPLORING NEGATIVE ATMOSPHERIC PRESSURE PHOTOIONIZATION FOURIER TRANSFORM ION CYCLOTRON RESONANCE MASS SPECTROMETRY FOR NITROGEN-RICH BIOFUELS

A manuscript to be submitted to *Energy & Fuels*

Carolyn P. Hutchinson[a], Amy McKenna[b], and Young Jin Lee[a]*

a: Department of Chemistry, Iowa State University, Ames, IA 50011

b: National High Magnetic Field Laboratory, Florida State University, Tallahassee, FL 32310

Abstract

Fast pyrolysis conversion of biomass offers a promising source of drop-in transportation fuels, and gasification of biomass offers a potential alternative to fossil fuels for commercial power production. However, both thermochemical processes currently suffer limitations due to bottlenecks in reactor design which result in fuel problems, such as tar buildup in gasification and bio-oil which requires extensive upgrading. Analyzing these fuels on a molecular level can provide insight to help solve the design bottlenecks but ionization remains a problem. In this work, negative-mode atmospheric pressure photoionization (APPI) is compared to three more common ionization modes (positive APPI, positive electrospray ionization, and negative electrospray ionization) in order to determine whether it is a less selective ionization source for whole biofuel analysis when coupled with high resolution Fourier transform

ion cyclotron resonance mass spectrometry (FT-ICR MS). Negative APPI-FT-ICR MS is able to ionize a range of compounds which encompasses those ionized by (+) APPI, (+) ESI, and (-) ESI. Additionally, (-) APPI shows less selectivity towards any one heteroatom class than the other three ionization methods, providing a more complete molecular-level view of the biofuels without using multiple ionization methods.

Introduction

Thermochemical conversion of biomass offers a promising alternative to petroleum products, such as transportation fuels from fast pyrolysis bio-oils and syngas from gasification.[1-4] Fast pyrolysis is a process by which biomass is rapidly heated at moderate temperatures (around 500 °C) in the absence of oxygen to produce condensable bio-oil. By gaining a thorough understanding of bio-oil on a molecular rather than bulk level, reactor designs can be refined and techniques for upgrading bio-oils to drop-in fuels can be developed.[1, 5] Gasification converts biomass into syngas (primarily CO and H_2) at high temperatures (above 700 °C) with sub-stoichiometric amounts of oxygen.[4] In addition to syngas, biotar and char are also produced, both of are problematic in reactor systems; much research has been devoted over the last two decades to eliminating the production of these additional products.[4] Biotar is particularly problematic as it can clog reactors. Understanding its chemical composition at a molecular level is crucial to prevent condensation and clogging in future reactors.[4, 6-7]

Currently, chemical analysis for biofuels is largely conducted by bulk analysis methods such as NMR, FTIR, and TGA.[2-3, 7] These methods are not sufficient to gain a complete understanding of the molecular-level complexity of biofuels. GC-MS is also

often applied but it can only detect volatile compounds; this fails to completely characterize biofuels since a large portion of these are nonvolatile.[1, 3, 7] While a relationship between temperature and the structures present in biofuels is known, the exact relationship between temperature and structure is still under debate, due in large part to the lack of good detection of nonvolatiles.[7]

Recent advancements in atmospheric pressure ionization (API), especially when coupled with high resolution mass spectrometry (HRMS), offer an alternative to the traditional bulk characterization of biofuels. Our group, in particular, has had great success coupling API with HRMS. Smith et al. compared (-) ESI on three different HRMS instruments for analysis of red oak bio-oil, finding the (-) ESI is typically dominated by low mass (*m/z* 100-250) compounds.[8] Cole et al. compared LDI, (-) ESI, and (+) APPI to compare switchgrass biochar from fast pyrolysis and gasification.[9] Smith et al. utilized (-) ESI and (+) APPI coupled with HRMS to study bio-oil aging.[10] Lee et al. analyzed lipids extracted from algal bio-oils using positive mode ESI, APPI, APCI, and MALDI.[11] Cole et al. were able to identify nearly 300 nitrogen-containing compounds in switchgrass bio-oil using (-) ESI, (+) ESI, and (+) APPI coupled with Orbitrap MS, including pyridine- and imidazole-based compounds.[12] Finally, Cole and Lee applied a novel system that couples a micropyrolyzer with GC to a time-of-flight mass spectrometry to successfully evaluate *in situ* catalytic fast pyrolysis.[13]

However, effectively ionizing all compounds with minimal specificity remains a problem. One of the more recently developed ionization techniques, atmospheric pressure photoionization (APPI), may be able to solve this problem. APPI-FT-ICR MS has recently gained popularity in petroleomics due to its ability to ionize large molecules not

accessible by other ionization methods.[14] APPI was first introduced as positive-mode in 2000[15] and then negative-mode in 2004.[16-17] (-) APPI offers reduced background noise and can ionize a more comprehensive range of molecule types than any other API method.[18] (+) APPI was able to effectively ionize nonpolar compounds not accessed by ESI in order to extend sulfur speciation of petroleum mixtures by Purcell et al.[19] and later was positive and negative APPI were also used to extend nitrogen-containing aromatic speciation as well.[20] Qian et al. used APPI to observe vanadyl porphyrins and sulfur-containing vanadyl porphyrins.[21] Huba et al. compared positive and negative APPI, ESI, and atmospheric pressure chemical ionization (APCI) coupled with an Orbitrap Q Exactive for model petroleum compounds; APPI in both polarities ionized the widest range of compounds, had the smallest suppression effects, and provided the best results regarding ionization efficiency. They also observed especially good ionization for nitrogen-containing compounds in both (+) APPI and (-) APPI.[22] Huba and Gardianli compared (-) ESI and (-) APPI to characterize weathered Mocando crude oil released during the *Deepwater Horizon* accident finding that both ionization methods provided different but complementary information about oxygen-containing species.[23] (-) APPI has been successfully applied to characterize asphaltenes in petroleum oil by Pereira et al and by Rogel et al.[24-25] With the exception of Huba et al., all of these experiments were performed using FT-ICR MS.

Positive-mode APPI-FT-ICR MS has also had measured success in bio-oil analysis. Chiaberge et al. compared (+) ESI, (+) APPI, and (+) APCI for hydrothermal liquefaction bio-oil and found that (+) APPI was able to best describe the molecular composition of the actual elemental composition.[26] Hertzog et al. compared (+) and (-)

ESI to (+) APPI as well as laser desportion ionization, finding that all three atmospheric sources were necessary for exhaustive characterization.[27] However, negative-mode APPI has not been thoroughly explored, especially for biofuel applications. In this work, (-) APPI is compared to both positive- and negative-mode ESI as well as (+) APPI for bio-oil and biotar from nitrogen-rich switchgrass feedstocks. We hypothesize that (-) APPI coupled with FT-ICR MS will ionize less preferentially in order to provide a more complete picture of biofuel composition.

Experimental Section

Samples & Handling

Fast pyrolysis bio-oil is the same as previously reported by Wilson et al.[28] Briefly, the was switchgrass grown in Boone County, IA, USA and was harvested on June 20, 2010 then dried to a constant weight, ground, and sieved using a mesh size of 200-700 μm. This biomass was subjected to fast pyrolysis at 550 °C in a freefall reactor, and the resultant bio-oil was fractionated to reduce water content and acidity. Stage fraction 3 was used in this study as it has been shown to typically contain the largest amount of nitrogen, according to previous elemental analysis. The June harvest dates assures that the switchgrass is collected at the peak of the growing season, when the nitrogen content is highest (0.51 wt% in bio-oil).[28]

The biotar is the same as previously reported by Broer and Brown.[29] Briefly, this switchgrass was grown near Centerville, IA, USA then was dried, ground, and sieved (mesh size 212-500 μm). This biomass underwent gasification at 750 °C in a fluidized

bed reactor with an equivalence ratio of 0.2 using a mix of O_2 and CO_2 as the fluidizing agents. The biotar was collected at three points of the previously described gasifier; the sample being analyzed in this study was collected at electrostatic precipitator body (part 2, figure 2 in reference 23).

The raw bio-oil and biotar were stored in nalgene bottles at -4 °C until analysis to minimize chemical changes. Stock solutions were prepared at 1 mg mL^{-1} in methanol and then diluted to appropriate concentrations. For FT-ICR analysis, ESI solutions were prepared at 250 µg mL^{-1} in 100% methanol and APPI solutions were prepared at 125 µg mL^{-1} in 75:25 (v/v) methanol and toluene. Gasification tar was handled identically except that APPI solutions for analysis were prepared in 50:50 (v/v) methanol and toluene and 75:25 (v/v) methanol and water for ESI. High purity methanol and toluene were used as solvents.

Instrumentation & Data Analysis

Samples were sent to the National High Magnetic Field Laboratory at Florida State University for analysis. A previously described 9.4T FT-ICR was used to collect data for all samples in both positive and negative APPI and ESI modes.[30] Atmospheric pressure chemical ionization was not used as it was unsuccessful in initial tests on a Bruker 7T SolariX FT-ICR MS housed at Iowa State University. All spectra were collected with a transient of 6.8 s, giving a resolving power of approximately 1.3 M at *m/z* 400. Multiple time-domain acquisitions (100-150) were averaged for each sample. All data was analyzed in absorption mode, zero-filled, and Hanning-apodized. PetroOrg (Future Fuels Institute, Tallahassee, FL, USA) was used to calibrate spectra, assign

chemical compositions, and generate double bond equivalence versus carbon number graphs.

Results and Discussion

Heteroatom Distributions

The four ionization modes investigated produced similar mass spectra for either bio-oil (Figure S1) or biotar (Figure S2), though spectra from either APPI polarity cover a larger *m/z* range than spectra from either ESI polarity. Additionally, both ESI polarities display a handful of single, high intensity ions due to the intrinsic selectivity of the ionization processes. Chemical composition analysis was performed in order to explore the differences between ionization modes more in depth. The heteroatom distributions for bio-oil are shown in Figure 1. Both (+) APPI (Figure 1B) and (+) ESI (Figure 1D) are dominated by N_xO compounds. (+) ESI is known to be highly selective towards basic compounds which can readily accept protons and (+) APPI, though less selective, can suffer from this same issue. (-) ESI (Figure 1C) is dominated by O_x compounds. These compounds tend to be more acidic than N_xO compounds, which means they are preferentially ionized by the deprotonation mechanism of (-) ESI. Unlike the other three ionization methods, however, (-) APPI (Figure 1A) is not dominated by one type of heteroatom to the exclusion of others. The O_x heteroatom class is more abundant than the nitrogen-containing species; however, the amount of oxygen present is much greater than the amount of nitrogen present in the bio-oil sample (35-40 wt% compared to 0.51 wt%).[28]

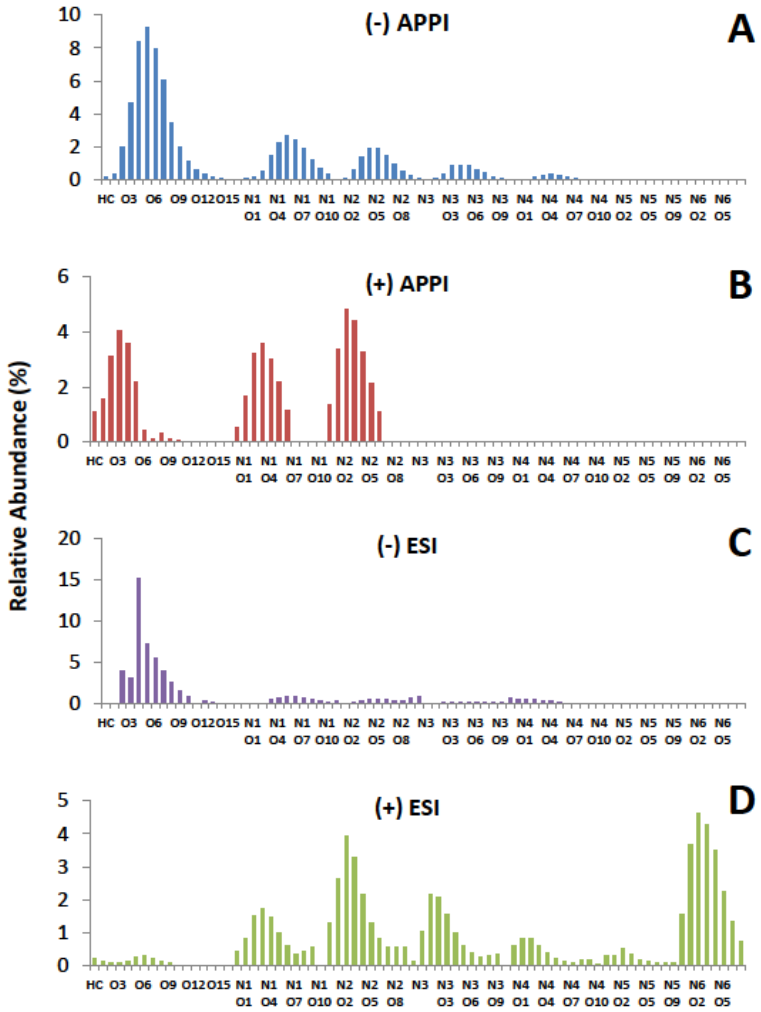

Figure 1. Heteroatom distributions for switchgrass fast pyrolysis bio-oil in (A) (-) APPI, (B) (+) APPI, (C) (-) ESI, and (D) (+) ESI.

Chemical composition analysis was also performed for biotar, and the heteroatom distributions are shown in Figure 2. As with bio-oil, (+) ESI (Figure 2D) is dominated by N_xO compounds and (-) ESI (Figure 2C) is dominated by O_x compounds. However, O_x compounds in biotar are more abundant than N_xO compounds in (+) APPI of biotar (Figure 2B). However, there is less nitrogen in the biotar than in the bio-oil, which may explain this difference rather than suppression effects specific to biotar. As with bio-oil, (-) APPI (Figure 2A) is able to detect O_x and N_xO with less discrimination between the

classes and generally provides a broader picture of the biofuel with a single ionization mode.

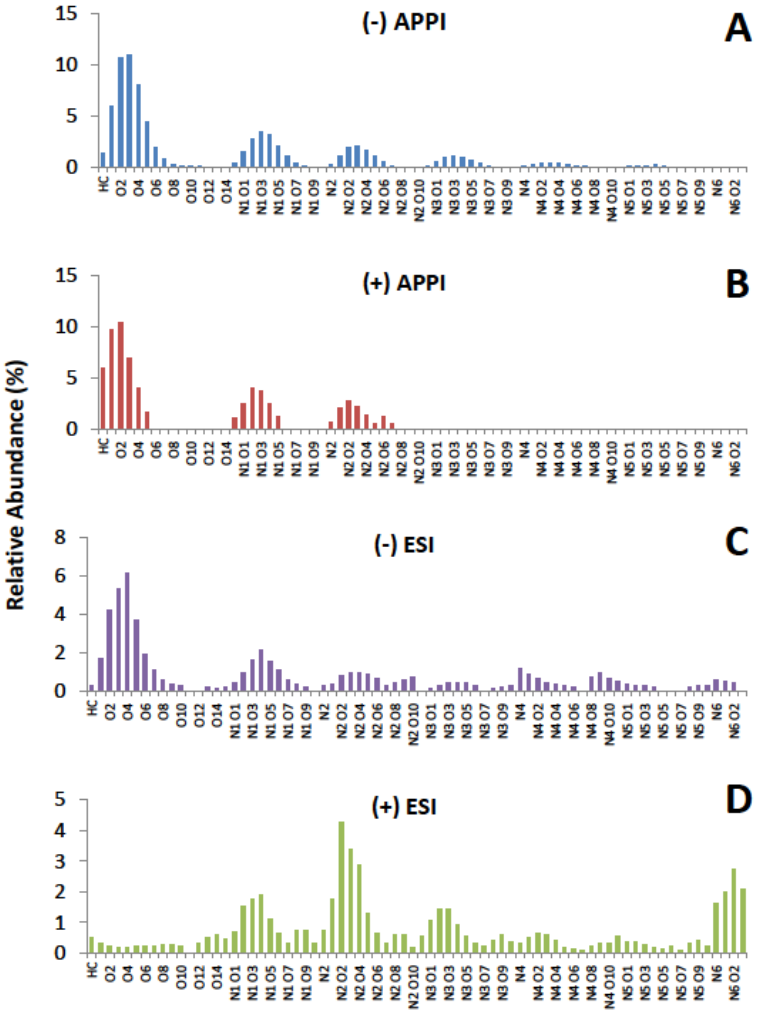

Figure 2. Heteroatom distributions for switchgrass gasification biotar in (A) (-) APPI, (B) (+) APPI, (C) (-) ESI, and (D) (+) ESI.

Contour Plots

In order to further investigate the claim that (-) APPI ionizes compounds accessed by (+) APPI, (+) ESI, and (-) ESI, double bond equivalence (DBE) versus carbon number plots were constructed. In particular N_xO (x=1-4) classes were compared between (-) APPI, (+) APPI, and (+) ESI in bio-oil (Figure 3), and Ox classes were compared for (-) APPI, (+) APPI, and (-) ESI in biotar (Figure 5). These classes were chosen for their

significant differences and known selectivity between ionization methods. The dashed red line in the figures denotes the theoretical DBE limit; the closer to the theoretical limit a molecule, the more aromatic and nonpolar it is.

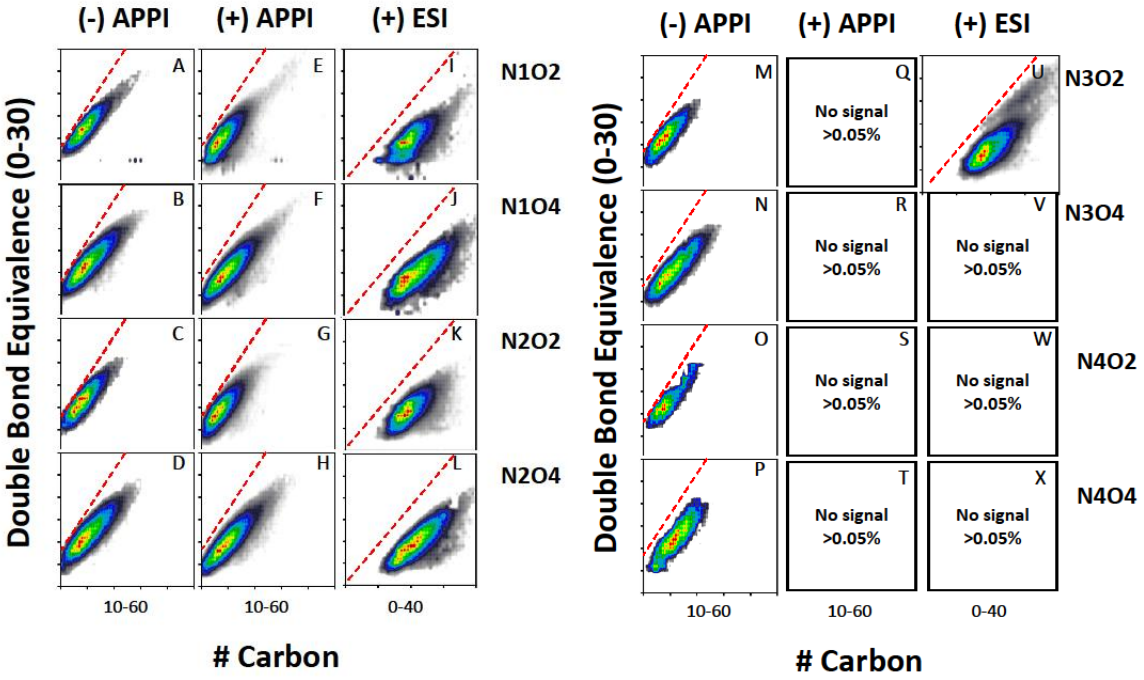

Figure 3. Double bond equivalence versus carbon number plots from switchgrass fast pyrolysis bio-oil for N_1O_2, N_1O_4, N_2O_2, N_2O_4, N_3O_2, N_3O_4, N_4O_2, and N_4O_4 in (-) APPI (A-D, M-P), (+) APPI (E-H, Q-T), and (+) ESI (I-L, U-X).

The DBE versus #C plots for select N_xO heteroatom classes in bio-oil are shown in Figure 3. These classes were chosen due to the high abundance of nitrogen compounds in switchgrass bio-oil in all ionization methods. (-) APPI and (+) APPI were compared to (+) ESI for its selectivity towards basic molecules. It is readily obvious that (-) APPI and (+) APPI access a different region of compounds than (+) ESI. The compounds ionized by (-) APPI are generally lower #C but higher DBE than those ionized by (+) ESI, suggesting they are far more nonpolar which is why they are not ionized by (+) ESI. (-) APPI is able to ionize some of the compounds (+) ESI does, it is also able to access some

of the nitrogen compounds ionized by (+) APPI. This means that (-) APPI can be used to detect compounds that would normally require both (+) ESI and (+) APPI to detect with little loss of information.

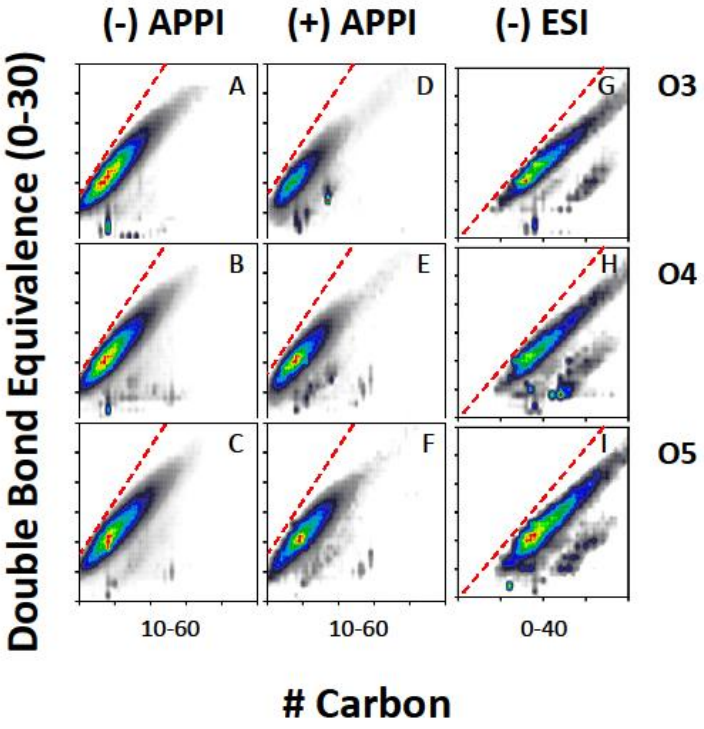

Figure 4. Double bond equivalence versus carbon number contour plots for O3, O4, and O5 heteroatom classes from FT-ICR MS analysis of switchgrass biotar with (-) APPI (A-C), (+) APPI (D-F), and (-) ESI (G-I).

In Figure 4, the O3, O4, and O5 heteroatom DBE versus #C plots for biotar are compared in (-) APPI, (+) APPI, and (-) ESI. (-) ESI was chosen for its selectivity towards acidic compounds, such as highly oxygenated species. These are highly abundant in all biofuels derived from lignocellulosic biomass due to the large amount of oxygen

present in lignocellulose. All three ionization methods cover similar #C and DBE ranges but both APPI polarities are more tightly clustered near the theoretical limit while (-) ESI is more even distributed along the entire #C range. Although (-) ESI is able to ionize more O-heteroatom compounds due to its selectivity than (-) APPI, (-) APPI is still able to ionize most of the same highly abundant compounds as (-) ESI compounds. A second grouping at lower #C and higher DBE can be seen that become more abundant. This second group overlaps slightly with the low abundance portion of the (-) APPI DBE versus #C plots but not the (+) APPI plots; as discussed previously, O4 compounds can be found in (-) APPI as well as (-) ESI. The species accessed by (-) APPI are low #C and high DBE compared to (-) ESI. In general, unlike (+) APPI which heavily favors nonpolar molecules, (-) APPI is able to ionize both polar and nonpolar compounds, making it an excellent general ionization technique for biofuels.

Conclusions

The use of (-) APPI allows for a single ionization method to provide a less selective view of nitrogen-rich switchgrass biofuels, such as bio-oil and gasification biotar. While the compounds detected with (-) APPI can be detected with other ionization methods, these other methods are highly selective towards one class of compounds and result in suppression of other. In switchgrass bio-oil, (-) APPI can ionize nitrogen-heteroatom species in the high mass region accessed by FT-ICR MS as well as highly oxygenated species. Highly conjugated, low oxygen-heteroatom molecules make up the majority of switchgrass gasification tar in (-) APPI, which is not significantly ionized by more common ionization methods such as ESI. By using (-) APPI, a more complete

picture of bio-oils can be constructed. A compound profile of gasification tar can be built for the first time using (-) APPI. In general, biotar is more highly conjugated and has larger carbon numbers than bio-oil, showing that it is composed of large, nonpolar molecules. Further study is needed to explore its structure and possible uses more in depth.

Acknowledgments

Work performed at the National High Magnetic Field Laboratory was supported by the National Science Foundation. The authors would also like to thank Karl Broer for the biotar samples and the Brown group for the switchgrass bio-oil samples, as well as Kaitlin Heinen for the work on dopants during her time as a SULI student.

References

1. Bridgwater, A. V., Review of fast pyrolysis of biomass and product upgrading. *Biomass Bioenerg* **2012,** *38*, 68-94.

2. Bridgwater, A. V.; Czernik, S.; Meier, D.; Piskorz, J., Fast pyrolysis technology. *Biomass: A Growth Opportunity in Green Energy and Value-Added Products, Vols 1 and 2* **1999**, 1217-1223.

3. Czernik, S.; Bridgwater, A. V., Overview of applications of biomass fast pyrolysis oil. *Energ Fuel* **2004,** *18* (2), 590-598.

4. Claude, V.; Courson, C.; Kohler, M.; Lambert, S. D., Overview and Essentials of Biomass Gasification Technologies and Their Catalytic Cleaning Methods. *Energ Fuel* **2016,** *30* (11), 8791-8814.

5. DOE In *Conversion Technologies for Advanced Biofuels: Preliminary Roadmap & Workshop Report*, Arlington, VA, Arlington, VA, 2011.

6. Milne, T. A. A., N.; Evans, R. J. *Biomass gasification "tars": their nature, formation, and conversion*; National Renewable Energy Laboratory: Golden, CO, USA, 1998.

7. Prando, D.; Ail, S. S.; Chiaramonti, D.; Baratieri, M.; Dasappa, S., Characterisation of the producer gas from an open top gasifier: Assessment of different tar analysis approaches. *Fuel* **2016,** *181*, 566-572.

8. Smith, E. A.; Park, S.; Klein, A. T.; Lee, Y. J., Bio-oil Analysis Using Negative Electrospray Ionization: Comparative Study of High-Resolution Mass Spectrometers and Phenolic versus Sugaric Components. *Energ Fuel* **2012,** *26* (6), 3796-3802.

9. Cole, D. P.; Smith, E. A.; Lee, Y. J., High-Resolution Mass Spectrometric Characterization of Molecules on Biochar from Pyrolysis and Gasification of Switchgrass. *Energ Fuel* **2012,** *26* (6), 3803-3809.

10. Smith, E. A.; Thompson, C.; Lee, Y. J., Petroleomic Characterization of Bio-Oil Aging using Fourier-Transform Ion Cyclotron Resonance Mass Spectrometry. *B Korean Chem Soc* **2014,** *35* (3), 811-814.

11. Lee, Y. J.; Leverence, R. C.; Smith, E. A.; Valenstein, J. S.; Kandel, K.; Trewyn, B. G., High-Throughput Analysis of Algal Crude Oils Using High Resolution Mass Spectrometry. *Lipids* **2013,** *48* (3), 297-305.

12. Cole, D. P.; Smith, E. A.; Dalluge, D.; Wilson, D. M.; Heaton, E. A.; Brown, R. C.; Lee, Y. J., Molecular characterization of nitrogen-containing species in switchgrass bio-oils at various harvest times. *Fuel* **2013,** *111*, 718-726.

13. Cole, D. P.; Lee, Y. J., Effective evaluation of catalytic deoxygenation for in situ catalytic fast pyrolysis using gas chromatography-high resolution mass spectrometry. *J Anal Appl Pyrol* **2015,** *112*, 129-134.

14. Witt, M.; Timm, W., Determination of Simulated Crude Oil Mixtures from the North Sea Using Atmospheric Pressure Photoionization Coupled to Fourier Transform Ion Cyclotron Resonance Mass Spectrometry. *Energ Fuel* **2016,** *30* (5), 3707-3713.

15. Robb, D. B.; Covey, T. R.; Bruins, A. P., Atmospheric pressure photoionisation: An ionization method for liquid chromatography-mass spectrometry. *Anal Chem* **2000,** *72* (15), 3653-3659.

16. Basso, E.; Marotta, E.; Seraglia, R.; Tubaro, M.; Traldi, P., On the formation of negative ions in atmospheric pressure photoionization conditions. *J Mass Spectrom* **2003,** *38* (10), 1113-1115.

17. Kauppila, T. J.; Kotiaho, T.; Kostiainen, R.; Bruins, A. P., Negative ion-atmospheric pressure photoionization-mass spectrometry. *J Am Soc Mass Spectr* **2004,** *15* (2), 203-211.

18. Fredenhagen, A.; Kuhnol, J., Evaluation of the optimization space for atmospheric pressure photoionization (APPI) in comparison with APCI. *J Mass Spectrom* **2014,** *49* (8), 727-736.

19. Purcell, J. M.; Hendrickson, C. L.; Rodgers, R. P.; Marshall, A. G., Atmospheric pressure photoionization proton transfer for complex organic mixtures investigated by fourier transform ion cyclotron resonance mass spectrometry. *J Am Soc Mass Spectr* **2007,** *18* (9), 1682-1689.

20. Purcell, J. M.; Rodgers, R. P.; Hendrickson, C. L.; Marshall, A. G., Speciation of nitrogen containing aromatics by atmospheric pressure photoionization or electrospray ionization Fourier transform ion cyclotron resonance mass spectrometry. *J Am Soc Mass Spectr* **2007,** *18* (7), 1265-1273.

21. Qian, K.; Mennito, A. S.; Edwards, K. E.; Ferrughelli, D. T., Observation of vanadyl porphyrins and sulfur-containing vanadyl porphyrins in a petroleum asphaltene by atmospheric pressure photonionization Fourier transform ion cyclotron resonance mass spectrometry. *Rapid Commun Mass Sp* **2008,** *22* (14), 2153-2160.

22. Huba, A. K.; Huba, K.; Gardinali, P. R., Understanding the atmospheric pressure ionization of petroleum components: The effects of size, structure, and presence of heteroatoms. *Sci Total Environ* **2016,** *568*, 1018-1025.

23. Huba, A. K.; Gardinali, P. R., Characterization of a crude oil weathering series by ultrahigh-resolution mass spectrometry using multiple ionization modes. *Sci Total Environ* **2016,** *563*, 600-610.

24. Pereira, T. M. C.; Vanini, G.; Oliveira, E. C. S.; Cardoso, F. M. R.; Fleming, F. P.; Neto, A. C.; Lacerda, V.; Castro, E. V. R.; Vaz, B. G.; Romao, W., An evaluation of the aromaticity of asphaltenes using atmospheric pressure photoionization Fourier transform ion cyclotron resonance mass spectrometry - APPI(+/-)FT-ICR MS. *Fuel* **2014,** *118*, 348-357.

25. Rogel, E.; Moir, M.; Witt, M., Atmospheric Pressure Photoionization and Laser Desorption Ionization Coupled to Fourier Transform Ion Cyclotron Resonance Mass Spectrometry To Characterize Asphaltene Solubility Fractions: Studying the Link between Molecular Composition and Physical Behavior. *Energ Fuel* **2015,** *29* (7), 4201-4209.

26. Chiaberge, S.; Leonardis, I.; Fiorani, T.; Cesti, P.; Reale, S.; De Angelis, F., Bio-Oil from Waste: A Comprehensive Analytical Study by Soft-Ionization FTICR Mass Spectrometry. *Energ Fuel* **2014,** *28* (3), 2019-2026.

27. Hertzog, J.; Carre, V.; Le Brech, Y.; Mackay, C. L.; Dufour, A.; Masek, O.; Aubriet, F., Combination of electrospray ionization, atmospheric pressure photoionization and laser desorption ionization Fourier transform ion cyclotronic resonance mass spectrometry for the investigation of complex mixtures - Application to the petroleomic analysis of bio-oils. *Anal Chim Acta* **2017,** *969*, 26-34.

28. Wilson, D. M.; Dalluge, D. L.; Rover, M.; Heaton, E. A.; Brown, R. C., Crop Management Impacts Biofuel Quality: Influence of Switchgrass Harvest Time on Yield, Nitrogen and Ash of Fast Pyrolysis Products. *Bioenerg Res* **2013,** *6* (1), 103-113.

29. Broer, K. M.; Brown, R. C., The role of char and tar in determining the gas-phase partitioning of nitrogen during biomass gasification. *Appl Energ* **2015,** *158*, 474-483.

30. Senko, M. W.; Hendrickson, C. L.; PasaTolic, L.; Marto, J. A.; White, F. M.; Guan, S. H.; Marshall, A. G., Electrospray ionization Fourier transform ion cyclotron resonance at 9.4 T. *Rapid Commun Mass Sp* **1996,** *10* (14), 1824-1828.

Supplemental Information

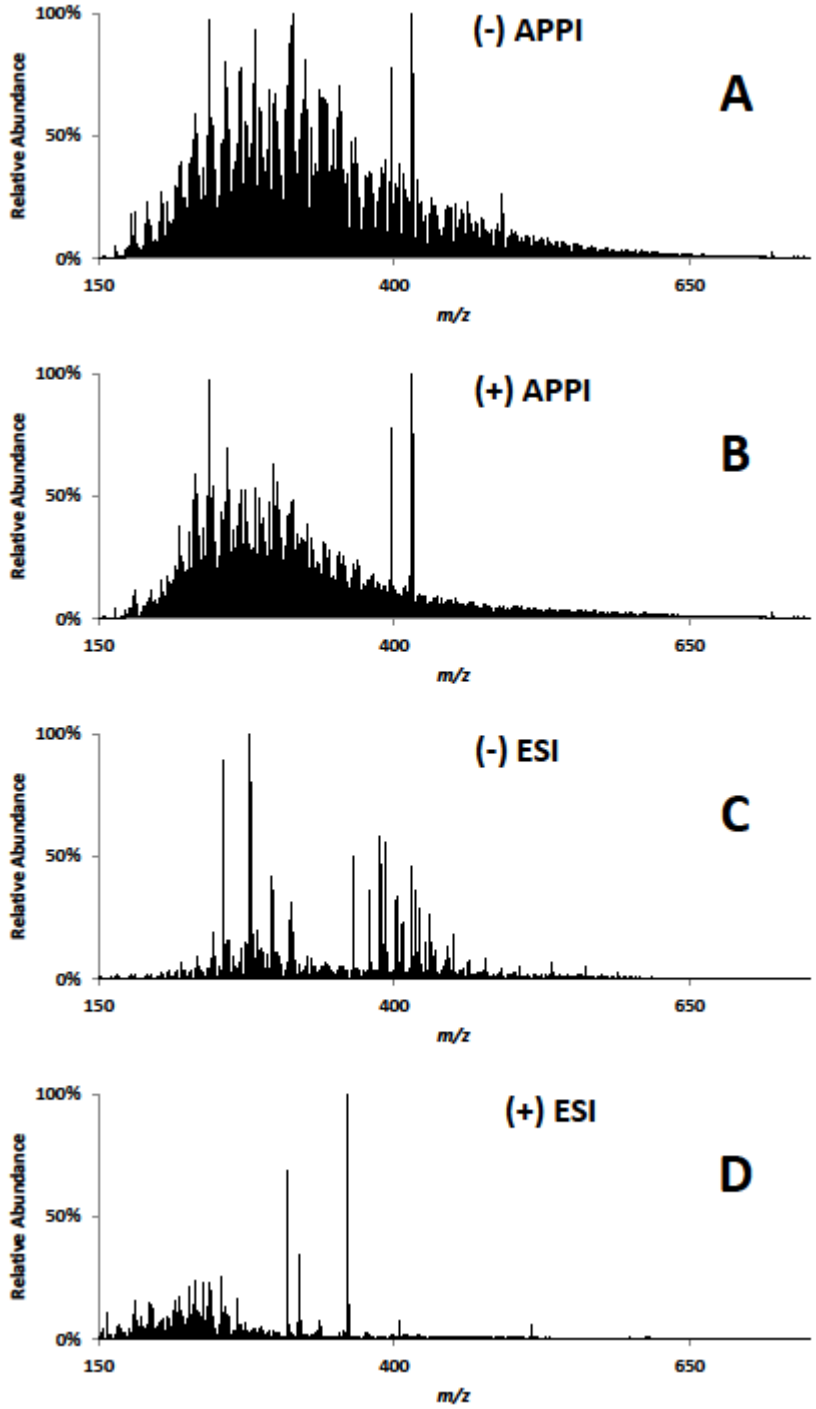

Figure S1. FT-ICR MS spectra from switchgrass fast pyrolysis bio-oil, analyzed with (-) APPI (A), (+) APPI (B), (-) ESI (C), or (+) ESI (D).

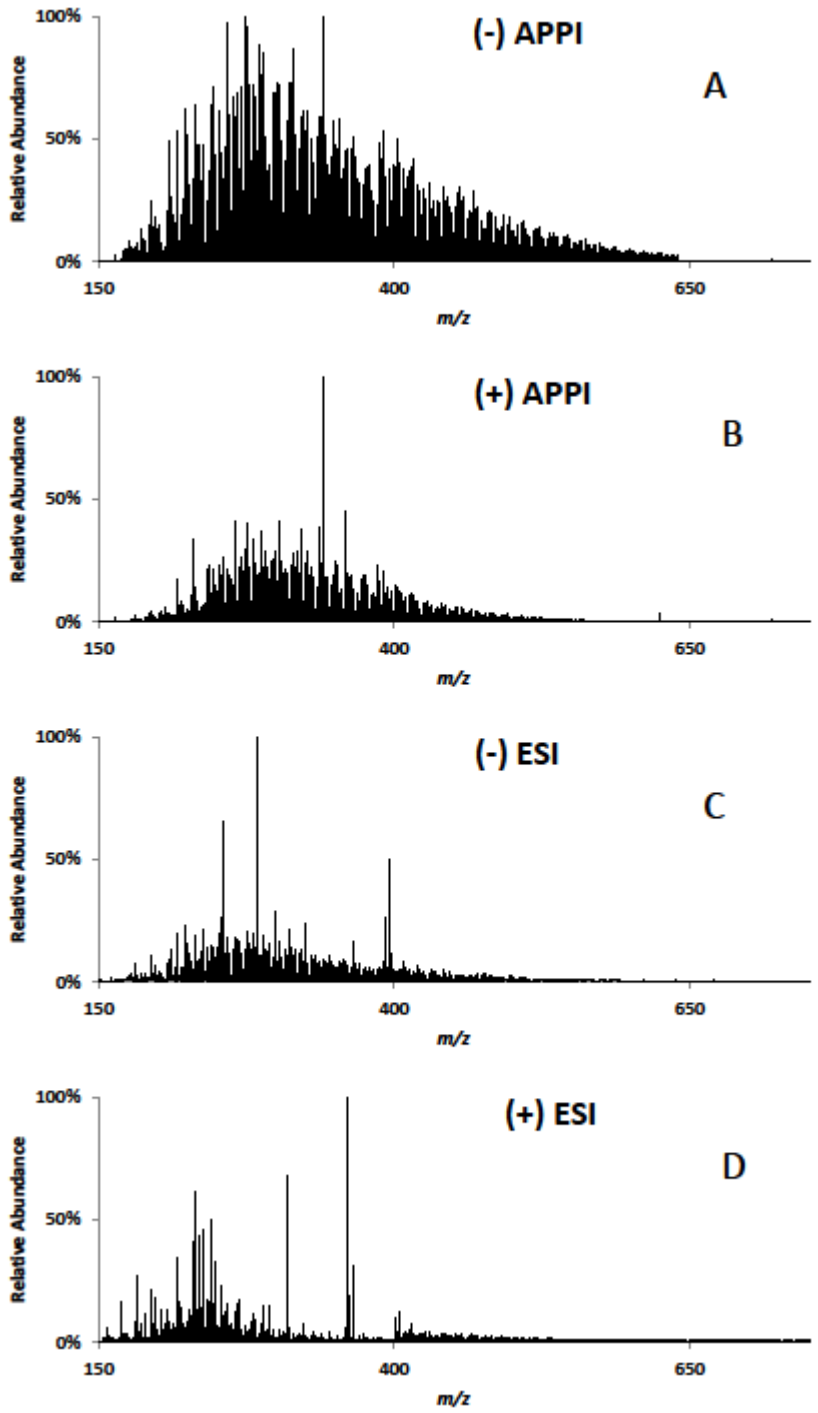

Figure S2. FT-ICR MS spectra from switchgrass gasification biotar, analyzed with (-) APPI (A), (+) APPI (B), (-) ESI (C), or (+) ESI (D).

CHAPTER 3

IMPACT OF HUMIDIFICATION ON DOPANT-ASSISTED ATMOSPHERIC PRESSURE CHEMICAL IONIZATION TIME-OF-FLIGHT MASS SPECTROMETRY

A manuscript to be submitted to *Rapid Communications in Mass Spectrometry*

Carolyn P. Hutchinson and Young Jin Lee

Abstract

Rationale

Water molecules play an important role in the ionization reactions of atmospheric pressure chemical ionization sources (APCI). Sources of water are limited in APCI sources coupled with gas chromatography (GC), so studying the impact of a humidification system on GC-APCI is crucial.

Methods

A simple, robust system is built to introduce humidified nitrogen gas into a GC-dopant-assisted APCI (dAPCI) source with ammonia as the dopant gas. The impact of humidity on the formation of radical, protonated, and ammonium adduct ions is explored using a standard mixture.

Results

The addition of controlled humidity reduces but does not eliminate fragmentation in fragile, highly oxygenated compounds such as levoglucosan. Humidification does generally increase the signal and promotes the formation of protonated ions over radical ions. When the ammonia dopant is added, fragmentation of highly oxygenated compounds is eliminated as they form stable ammonium ion adducts. The combination of

humidification and ammonia dopant in GC-dAPCI promotes protonated ions in phenols and ammonium ion adducts in highly oxygenated compounds. The ion signal generally increases with increasing humidity until the dry nitrogen to humidified nitrogen ratio is one-to-one, at which point the signal increase plateaus.

Conclusions

Controlling humidity in GC-APCI sources is important for promoting protonated ions over radical ions; when an ammonia dopant is added, the addition of water promotes ammonium adduct ion formation. The optimum ratio is a one-to-one ratio between dry nitrogen and humidified nitrogen in the current humidification control system.

Introduction

Gas chromatography coupled with mass spectrometry (GC-MS) has proven to be one of the most important and powerful tools for the analysis of volatile and thermally stable analytes since its introduction in the early 20th century. By combining the efficiency of GC separation with the spectral information and identification capability of MS, GC-MS has found applications ranging from foods to fuels to environmental applications.[1] Electron ionization (EI) is the most widely used ionization source in GC-MS due to its ability to ionize a wide range of organic molecules. During ionization, the molecule is typically fragmented extensively to produce a characteristic mass spectrum which can be identified using a spectral library. However, several problems persist with EI-MS: fragile compounds can be fragmented too extensively for confident identification; the molecular ion is often absent meaning that co-eluting species are difficult to identify; compounds which are not present in databases pose significant identification problems.

Chemical ionization (CI) has considerably less fragmentation but suffers from reduced ionization and less reliable database identification. Interest in the soft ionization offered by atmospheric pressure ionization (API) MS has grown recently due to the limitations of EI-MS and CI-MS. GC-API MS offers many advantages including the preservation of GC separation, interfacing with high resolution MS typically used for liquid chromatography (LC), generation and preservation of a molecular or pseudomolecular ions, chemical composition determination, and the potential to detect compounds not amenable to EI or CI.

Atmospheric pressure chemical ionization (APCI) coupled with gas chromatography was debuted by Horning, et al. in 1973 using ^{63}Ni β decay for ionization and a packed column.[2] Later GC-APCI systems adapted the corona discharge source and open capillary columns.[3] However, GC-APCI remained an exotic technique due to technical issues until roughly 15 years ago when sources that could operate in both GC and LC modes were introduced by McEwen and McKay and Schiewek, et al.[4-5] Since then, GC-APCI has been paired with time-of-flight mass spectrometry (TOF MS) with and without quadrupole(s) for a wide variety of applications including metabolomics, pharmaceuticals, pesticides, foodstuffs, and biological samples.[6-11] There have been technological advances as well including source miniaturization and the construction of a GC-APCI-QqTOF spectral library, similar to what exists for traditional GC-EI-MS.[12-13]

The importance of water in the ionization mechanisms for the formation of protonated molecules has been recognized since 1976.[3] Sunneret al. showed in 1988 that hydronium-water clusters play an important role in the formation of protonated ions in LC-APCI.[14] Klee, et al. discussed the importance of water clusters not only as proton

donors but as sites where ionization can occur in LC-API-MS systems.[15] Newsome, et al. showed that regulating humidity is important for direct analysis in real time MS analysis and plasma-based ambient ion sources as well.[16-17] Several recent GC-APCI-(Q)TOF MS manuscripts have included work on the importance of water as well. Portolés, et al. used an uncapped vial of water in a specially designed holder inside the source door to increase the sensitivity for pesticide residue analysis.[9] Wachsmuth, et al. found that continuous water infusion using a syringe pump yielded a 16.6-fold intensity increase for MCF-derviatized metabolite standards due to suppressed in-source fragmentation though MO-TMS derivatives were not significantly affected.[18] Raro, et al. found that the presence of water promoted the formation of protonated molecules for anabolic androgenic steroids.[6] However, no work has explored the impact of water in GC-APCI-MS systems when it is introduced in the gaseous state rather than relying on evaporation or introducing water as a liquid.

In this work, we build a simple, robust humidification introduction system for the Agilent GC-APCI source that interfaces through the source window and introduces water in the gaseous state. This humidification introduction system is used to provide constant humidity all year. Additionally, dilute ammonia gas is introduced to serve as a dopant in a system developed by our group. Dopant-assisted atmospheric pressure chemical ionization (dAPCI) TOF MS prevents fragmentation, creates ammonium adduct ions on otherwise fragile sugars, and promotes protonated ions. This means that our system does not require derivatization commonly used with GC-APCI-(Q)TOF MS. In this study, this system is applied to standard compounds commonly found in bio-oil, covering a range of furans, sugar-like compounds, and phenols.

Experimental Section

Materials & Sample Preparation

Pyrene, 3,5-dimethoxytoluene, levoglucosan, 5-hydroxymethyl furfural, furfuryl alcohol, *p*-cresol, syringol, apocynin, coniferyl aldehyde, syringaldehyde, acetosyringone, and eugenol were acquired from Sigma-Aldrich (St. Louis, MO) at the highest available purity (≥98%). An equimolar mixture (0.4 mM each) of these compounds in 1:1 methanol and water serves as a representative mixture of bio-oil and pyrolysis compounds.

Mass Spectrometry Analysis

Using an automatic liquid sampler (ALS, Agilent G4513A, Palo Alto, CA), 5 mL of the equimolar mixture is injected into to the GC-dAPCI-TOF MS system via the back inlet of a gas chromatograph (GC) (7890A, Agilent). The back inlet, interface, and oven temperatures are all set to 280 °C and the inlet split is set at 5:1. A low/mid polarity column (DB-1701, 30 m x 0.25 mm x 0.25 μm, Agilent) is used for the GC separation. The temperature is programmed to 35 °C for 3 min, ramped to 260 °C at 20 °C/min, then held for 2 min. A dopant-assisted APCI (dAPCI) source is used with a GC-APCI interface (Agilent) with ammonia (500 ppm in helium) serving as a dopant gas. Ammonia is pre-heated using approximately 1 m of 1/16" I.D. stainless steel tubing coiled inside the GC oven so that the ammonia dopant gas is heated to the same temperature as the column effluent, and it is introduced as a sheath gas around the capillary. The APCI source temperature is 325 °C, the corona discharge needle is set to 1.0 μA, the capillary voltage is -1000 V, the fragmentor voltage is 95 V, and the skimmer voltage is 65 V.

The GC-dAPCI source is shown in detail in Figure 1. The column or transfer line (D) extends 4-6 mm beyond the GC-APCI interface (B). Since the ammonia dopant is introduced as a sheath gas (C), the dopant and analytes can only interact inside the APCI source in the presence of the corona discharge needle (A). This allows for unique dopant-assisted atmospheric pressure chemical ionization (dAPCI). Once these reactions have occurred, they are attracted to the negatively charged TOF MS interface (F) and enter the TOF MS (E). The humidity is introduced off-axis through a threaded port in the source viewing window (G).

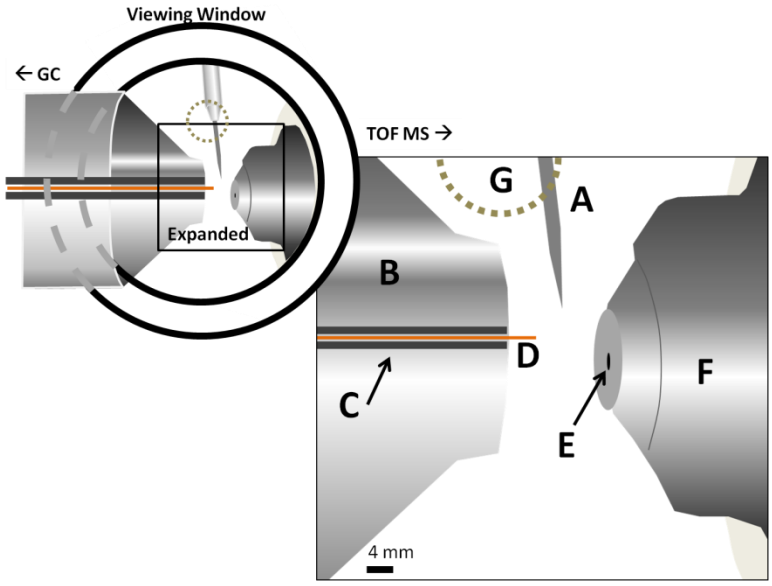

Figure 1. Diagram of the GC-APCI source as seen from the viewing window. The expanded view includes the (A) corona discharge needle, (B) GC-APCI coupling, (C) stainless steel transfer line extending from the GC through the GC-APCI coupling, (D) GC column extending 4 mm beyond GC-APCI coupling, (E) entrance to TOF MS, and (F) GC-APCI spray shield. Humidity is introduced into the source off-axis via a port in the viewing window (G).

Humidification System

Humidity is introduced from the side of the GC-APCI source. A detailed schematic of the humidification system can be found in the Supplemental Information (Figure S1). The quartz window in the source is replaced with a modified plexiglass window of the same dimensions for all humidity experiments except for those performed at standard conditions. Both windows are 2 inch round circles, 0.5 inch height; the plexiglass window has a threaded hole drilled 0.5 inch from the side to allow for a PTFE open fitting to be threaded in. Into this open fitting, a length of 1/16" outer diameter PTFE tubing is extended. On the dAPCI end of this tubing, a plastic ferrule and a small o-ring allow for a snug fit and optimization of the length inside the source. The opposite end is attached to a brass tee Swagelok fitting. This is split between the dry N_2 and the wet N_2 lines. The dry N_2 line goes from the final tee through a mass-controlled flow meter (Alicat Scientific, Tucson, AZ) to a humidity trap (SGE Incorporated, Pflugerville, TX) to another tee immediately after the UHP N_2 tank. The wet N_2 line goes from the final tee through a rotameter into the headspace of a 2 L PTFE liquid chromatography (LC) bottle containing 1500 mL of DI water. A second PTFE line runs from the UHP N_2 tank tee into the bottom of the LC bottle, providing agitation and creating an atmospheric of N_2 saturated with water. There is a vent on top of the bottle to prevent over pressurization. The combined flow is held constant at 10 mL/min. This system provides a simple, robust means of providing constant humidity to the dAPCI source regardless of external conditions.

Results and Discussion

Ionization Mechanisms

Dopant-assisted atmospheric pressure chemical ionization (dAPCI) is a soft ionization technique which is able to ionize molecules with minimal fragmentation. Figure 2 shows the effect of ammonia adduct formation on a fragile molecule. As seen in Figure 2A, GC-APCI produces large amounts of fragmentation in fragile compounds, such as levoglucosan, without the presence of an ammonia dopant. Losses of one and two waters are observed as well as dimmers formed from two levoglucosans as well as one levoglucosan and one dehydrated levoglucosan. When the dopant is introduced (Figure 2B), fragmentation is no longer observed and levoglucosan is observed as an ammonium ion adduct at *m/z* 180.087, corresponding to $[C_6H_{10}O_5+NH_4]^+$. Most compounds (with the exception of hydrocarbons) form ammonium ion adducts in the presence of the ammonia dopant gas. Ammonium ions also are able to act as a proton donor to increase the amount of protonated molecules. This allows for ionization of compounds with minimal fragmentation due to the stabilization effect provided by the ammonium ion, unlike the large amount of fragmentation typically seen with electron ionization commonly used in GC-MS. Since the molecular ion is preserved, GC-dAPCI can be combined with the high mass resolution capabilities of TOF MS and chemical compositions can be calculated for unknown identification.

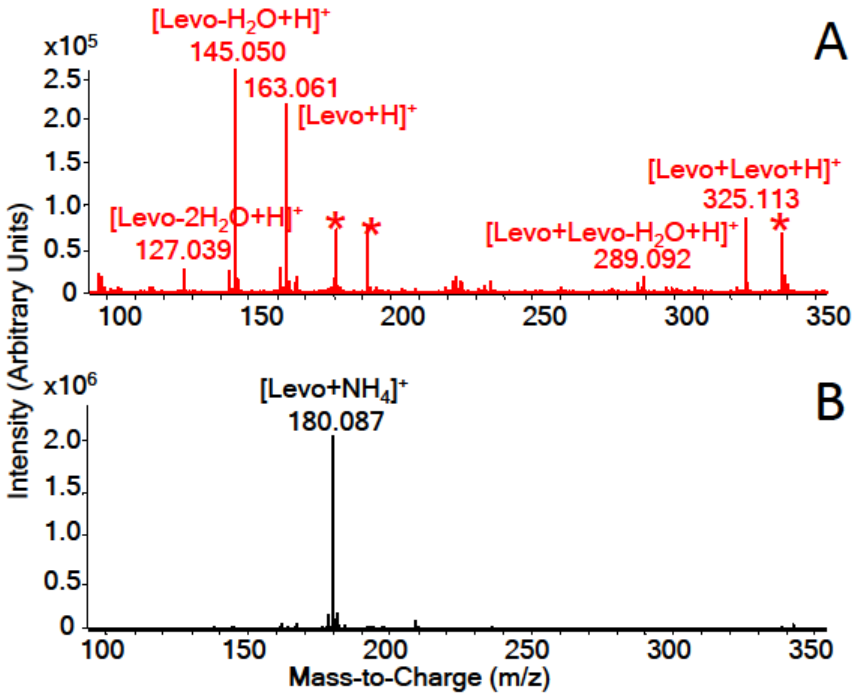

Figure 2. Comparison of spectra for levoglucosan (A) without ammonia dopant showing extensive fragmentation and (B) with ammonia dopant showing only a single peak corresponding to an ammonium adduct ion.

While the addition of ammonium ion adducts is a crucial component of analyzing fragile compounds in GC-dAPCI-TOF MS, gas-phase water ions have been shown to play an important role in the ionization mechanisms of APCI systems.[14] Scheme 1 describes the dominant system of ionization mechanisms in a dopant-free GC-APCI source. Atmospheric water first reacts with free electrons generated by the corona discharge needle to form radical H_2O cations, shown in reaction 1.1. In reaction 1.2, these radical cations then react with neutral ambient water molecules to provide hydronium cations and hydroxide anions. These hydronium ions can take one of two competing pathways: the hydronium ion can react with an analyte molecule which has a proton affinity equal to or greater than that of water (691 kJ/mol).[19] This reaction forms protonated ions (reaction 1.3a). The hydronium ion can alternatively react with other

neutral water molecules to form water clusters (reaction 1.3b). Reaction 1.3b will only occur when the water concentration is significantly higher than necessary for the APCI process.

$$H_2O + e^- \rightarrow H_2O^{+\bullet} + 2\ e^- \quad (1)$$
$$H_2O^{+\bullet} + H_2O \rightarrow H_3O^+ + OH^- \quad (2)$$
$$H_3O^+ + M \rightarrow [M+H]^+ + H_2O \quad (3a)$$
$$H_3O^+ + nH_2O \rightarrow H^+(H_2O)_{n+1} \quad (3b)$$

Scheme 1. Reactions of water in APCI sources.

$$NH_3 + e^- \rightarrow NH_3^{+\bullet} + 2\ e^- \quad (1)$$
$$NH_3^{+\bullet} + H_2O \rightarrow NH_4^+ + OH^- \quad (2)$$
$$NH_3 + H_3O^+ \rightarrow NH_4^+ + H_2O \quad (3)$$
$$NH_3 + H_2O \rightarrow NH_4^+ + OH^- \quad (4)$$

Scheme 2. Reactions of ammonia and ambient water in dAPCI sources.

$$NH_4^+ + M \rightarrow [M+H]^+ + NH_3 \quad (1)$$
$$NH_4^+ + M \rightarrow [M+NH_4]^+ \quad (2)$$
$$M + e^- \rightarrow M^{+\bullet} + 2\ e^- \quad (4)$$

Scheme 3. Formation of various ions in dAPCI sources.

When ammonia is introduced, it can be ionized to form ammonium through several reactions, shown in Scheme 2. Ammonia first reacts with free elections to generate radical cations in reaction 2.1. In reaction 2.2, these radical cations react with atmospheric water to produce the ammonium cation and a hydroxide anion. Alternatively, as seen in reaction 2.3, ammonia reacts with a hydroxide cation produced through a reaction pathway in Scheme 1 to produce ammonium and neutral water. Similarly, in reaction 2.4, neutral ammonia can react with neutral water to produce the ammonium cation and a hydroxide anion. Ammonium is preferentially formed in reaction 2.4 since the proton affinity of ammonia (853.6 kJ/mol)[19] is much higher than the proton affinity of water.

After the ammonium ions are formed, they can react with analyte molecules to form ions in one of two ways, shown in Scheme 3. If the analyte has a higher proton affinity than ammonia, a proton will be transferred to form the $[M+H]^+$ pseudomolecular ion, shown in reaction 3.1. Protonated ions can also form from proton transfer from hydronium, as seen in reaction 1.3a. Alternatively, as seen in reaction 3.2, if the ammonia affinity is sufficient then the analyte will be detected as an ammonium ion adduct. Radical formation from the reaction with free electrons from the corona discharge needle is also possible, shown in reaction 3.3.

Levoglucosan has a proton affinity calculated to be between 803.9 kJ/mol to 818.2 kJ/mol.[20] The fragmentation in levoglucosan can be explained by the difference in energy between the proton affinity for water (691 kJ/mol)[19] and levoglucosan. When the proton from hydronium is transferred to levoglucosan, the excess energy causes fragmentation. Other compounds investigated such as pyrene (869.2 kJ/mol),[19] furfuryl alcohol (849.4 kJ/mol),[19] and *p*-cresol (814 kJ/mol)[19] have similar proton affinities to levoglucosan. However, their ionization behavior and efficiency is extremely different without the presence of a dopant. While levoglucosan fragments extensively, as seen in figure 3A, pyrene forms a radical ion (*m/z* 202) and a protonated ion (*m/z* 203) in a nearly 1:1 ratio. Furfuryl alcohol exhibits a radical ion at *m/z* 98, peak at *m/z* 97 corresponding to $[M-H]^+$ formed by hydride abstraction (a common CI behavior in furans), and a water loss at *m/z* 81. The phenol *p*-cresol forms both a radical ion (*m/z* 108) and a protonated ion (*m/z* 109) in a 1:2 ratio (radical:protonated). Step 1 in Scheme 1 offers an explanation for the radical ions, though the difference in ionization energy between pyrene and *p*-cresol is only about 1 eV (7.4256 eV for pyrene compared to 8.31 eV for *p*-cresol).[21]

Due to its similar proton affinity to most analytes of interest, ammonia (853.6 kJ/mol)[19] was chosen as a positive-mode dopant. Since ammonia has a proton affinity larger than that of water, it is readily protonated by ambient water in the APCI source. Additionally, it has been shown that the ammonium ion can form hydrogen bonds.[22] This allows for extremely stable adduct formation with molecules containing groups available for hydrogen bonding (e.g., alcohols and acids) that are common in the analytes of interest.

Humidity Control & Optimization

An initial experiment was performed by adding water to the source with a cotton swab and introducing levoglucosan using a micropyrolyzer and a 0.6 m length deactivated fused silica transfer line (100 µm I.D.); spectra were collected before and after the uncontrolled addition of water (Figure S2). Before adding water, the signal is about 5E+5, and after there is a 17-fold increase to 8.5E+6. However, since this addition of water was uncontrolled, levoglucosan dimers and trimers were observed at *m/z* 342 and *m/z* 504 respectively. Over time as the water exits the source, these multimers decrease in abundance then cease to form. These experiments were performed in November, when the ambient humidity is low, showing the necessity of this humidification system.

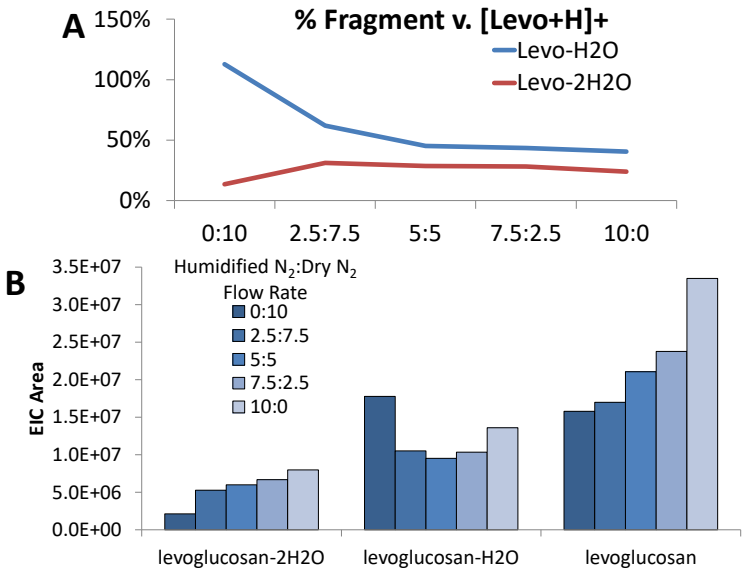

Figure 3. Effect of humidity on levoglucosan without ammonia dopant. (A) Comparison of EIC area for fragments to EIC area for protonated levoglucosan. (B) EIC areas for major fragments and protonated levoglucosan ions.

In order to optimize and explore the effects of humidity in the dAPCI environment, an equimolar mixture of standard compounds was injected into the GC and separated using a mid/low-polarity column. For all experiments, the gas flows were investigated with the humidified N_2 at five different flow rates (0, 2.5, 5, 7.5, 10 mL/min) with dry N_2 making up the rest of the total 10 mL/min flow. When no humidified N_2 is flowing, the source is assumed to be dehumidified. Humidity was first investigated without the ammonia dopant. Figure 3 shows the effects of humidity on fragmentation using levoglucosan as a representative of other fragile compounds. The two main fragments consisting of one and two water losses, respectively, are compared to the protonated levoglucosan peak in Figure 3A. As humidity increases, the fragmentation decreases until it levels off when the flow rates are set at 5:5. The signal of the singly dehydrated ion, $[C_6H_{10}O_5\text{-}H_2O\text{+}H]^+$ (*m*/z 145), decreases from 120% to 45% between 0 mL/min and 5 mL/min humidified N_2 flow then from 45% to 41% between 5 mL/min

and 10 mL/min humidified N_2 flow. The signal of the doubly dehydrated on, $[C_6H_{10}O_5\text{-}2H_2O+H]^+$ (*m/z* 127), increases initially from 13% to 31% between 0 mL/min and 2.5 mL/min humidified N_2 flow then decreases to 24% at 10 mL/min humidified N_2 flow. Even though the doubly dehydrated fragment increases, it does not dominate the protonated ion unlike the singly dehydrated fragment, as seen in Figure 3B. The signal increases as the humidified N_2 flow is increased and the fragmentation decreases relative to protonated levoglucosan. This means that even though the signal of all ions is generally increasing, the amount of fragmentation is decreasing as humidity increases.

When ammonia is introduced, several compounds, especially phenols, exhibit both protonated and radical ions as well as ammonium adduct ions in dAPCI. The delocalized π-electrons reduce the partial negativity on the phenol group and decrease its ability to form hydrogen bonds with the ammonium ion. This complicates spectra and will hinder identification of unknowns, especially in complex samples such as whole bio-oil or unseparated biomass pyrolyzates. This behavior still occurs when ammonia dopant is added. Thus, driving these compounds toward one dominant ion species is highly desirable. Using extracted ion chromatograms (EICs), the ratios of protonated-to-radical areas for several representative phenols and pyrene are shown in Figure 4A. An increase in the protonated ion compared to the radical ion is observed for all compounds except for coniferyl aldehyde, which increases until 5 mL/min humidified N_2 flow then ceases to increase further. The observed increases over the total flow rate range vary from 60% for *p*-cresol to 83% for acetosyringone and from 49% for *p*-cresol to 72% for coniferyl aldehyde over the 0 mL/min to 5 mL/min range, showing that most of the protonated-to-radical signal increase occurs between 0 mL/min and 5 mL/min humidified N_2 flow rate.

As seen in Figure 4B, there is also an increase in the ratio of the protonated ion to the ammonium adduct ion for these compounds, with the exception of coniferyl aldehyde which has a 2% decrease in protonated-to-ammonium adduct ratio, though the increase is less dramatic than the protonated-to-radical ratio increase and generally plateaus after 5 mL/min humidified nitrogen flow. 5-hydroxymethylfurfural (not shown) exhibits similar behavior to most phenols, with an increase in both protonated-to-radical ratio and protonated-to-ammonium ion adduct ratio observed.

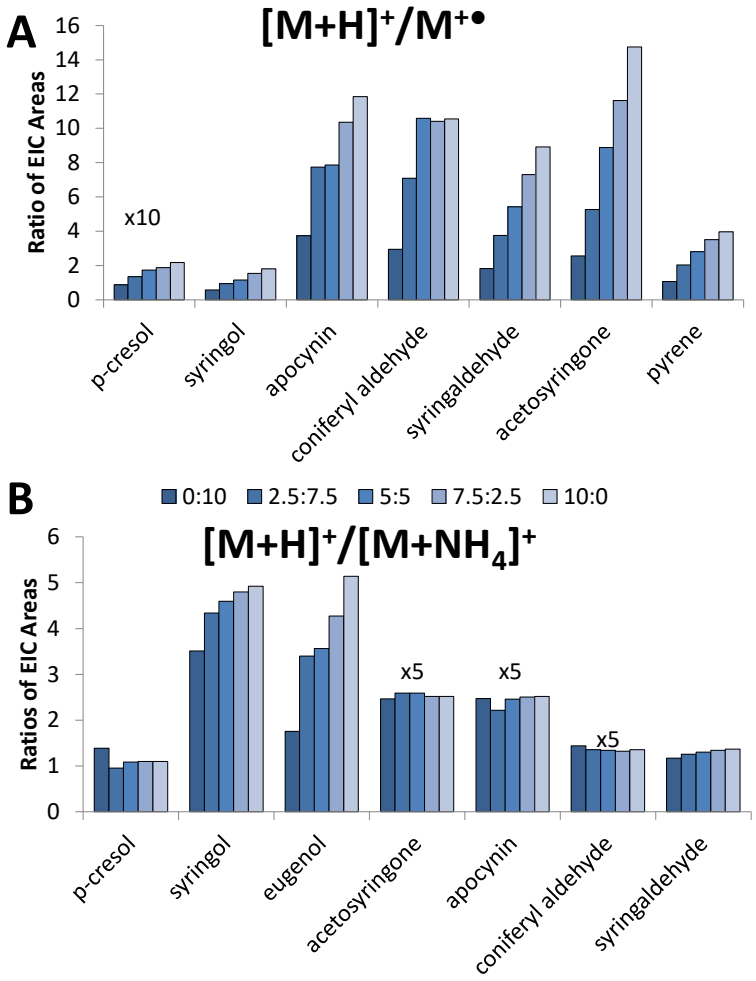

Figure 4. Ratios of EIC areas for (A) protonated and radical ions for several phenols and pyrene and (B) protonated and ammonium adduct ions for several phenols.

Highly oxygenated compounds such as furfuryl alcohol and levoglucosan preferentially make only ammonium adduct ions; the fragmentation observed without the dopant even in the presence of ample humidity is prevented by the stabilization provided by the ammonium adduct. 3,5-dimethoxytoluene only forms a radical. Since methoxy functionalities are unable to participate in hydrogen bonding, 3,5-dimethoxytoluene is unable to form ammonium ion adducts. Without a good site for protonation, 3,5-dimethoxytoluene favors the radical cation formation over the protonated ion formation regardless of ambient conditions.

Conclusions

A simple, robust humidification system was built and optimized for the dopant-assisted atmospheric pressure chemical ionization (dAPCI) source for GC-dAPCI-TOF MS analysis. Water molecules play an extremely important role in APCI sources and by providing reliable source of constant humidity, we are able to improve ionization of many molecules similar to those typically found in bio-oils and biomass pyrolyzates. Ammonia gas, with a proton affinity close to or slightly lower than most analytes of interest, serves as an excellent dopant. The ammonium ion adducts prevent fragmentation of fragile compounds (e.g., levoglucosan) while serving as a proton donor to increase protonated ion formation in compounds which preferentially form protonated ions. The decrease in other ion species compared to protonated ions will be beneficial for the confident chemical identification of unknown analytes and for interpreting spectra from whole biomass pyrolysis. When both optimal humidity and ammonia dopant are provided, the signal of all analytes is increased compared to an environment where humidity is

uncontrolled. This system has been routinely used with great success for over two and a half years by our group now. Measuring the humidity in the source has proved challenging, as hygrometers do not perform well at such high temperatures. In the future, providing a humidity-controlled enclosure for the dAPCI-TOF MS system, such as the one used at the US Naval Research Laboratory for their DART-MS instrument, that excludes the GC for easy access could ensure even more control over the ambient conditions affecting dAPCI.[16]

Acknowledgements

This work is supported by National Science Foundation, Division of Chemical, Bioengineering, Environmental and Transport Systems, Energy for Sustainability Program.

References

1. Li, D. X.; Gan, L.; Bronja, A.; Schmitz, O. J., Gas chromatography coupled to atmospheric pressure ionization mass spectrometry (GC-API-MS): Review. *Anal Chim Acta* **2015,** *891*, 43-61.

2. Horning, E. C.; Horning, M. G.; Carroll, D. I.; Dzidic, I.; Stillwell, R. N., New Picogram Detection System Based on a Mass-Spectrometer with an External Ionization Source at Atmospheric-Pressure. *Anal Chem* **1973,** *45* (6), 936-943.

3. Dzidic, I.; Carroll, D. I.; Stillwell, R. N.; Horning, E. C., Comparison of Positive-Ions Formed in Nickel-63 and Corona Discharge Ion Sources Using Nitrogen, Argon, Isobutane, Ammonia and Nitric-Oxide as Reagents in Atmospheric-Pressure Ionization Mass-Spectrometry. *Anal Chem* **1976,** *48* (12), 1763-1768.

4. Schiewek, R.; Lorenz, M.; Giese, R.; Brockmann, K.; Benter, T.; Gab, S.; Schmitz, O. J., Development of a multipurpose ion source for LC-MS and GC-API MS. *Anal Bioanal Chem* **2008,** *392* (1-2), 87-96.

5. McEwen, C. N.; McKay, R. G., A combination atmospheric pressure LC/MS : GC/MS ion source: Advantages of dual AP-LC/MS : GC/MS instrumentation. *J Am Soc Mass Spectr* **2005,** *16* (11), 1730-1738.

6. Raro, M.; Portoles, T.; Sancho, J. V.; Pitarch, E.; Hernandez, F.; Marcos, J.; Ventura, R.; Gomez, C.; Segura, J.; Pozo, O. J., Mass spectrometric behavior of anabolic androgenic steroids using gas chromatography coupled to atmospheric pressure chemical ionization source. Part I: Ionization. *J Mass Spectrom* **2014,** *49* (6), 509-521.

7. Hurtado-Fernandez, E.; Pacchiarotta, T.; Longueira-Suarez, E.; Mayboroda, O. A.; Fernandez-Gutierrez, A.; Carrasco-Pancorbo, A., Evaluation of gas chromatography-atmospheric pressure chemical ionization-mass spectrometry as an alternative to gas chromatography-electron ionization-mass spectrometry: Avocado fruit as example. *J Chromatogr A* **2013,** *1313*, 228-244.

8. Wachsmuth, C. J.; Almstetter, M. F.; Waldhier, M. C.; Gruber, M. A.; Nurnberger, N.; Oefner, P. J.; Dettmer, K., Performance Evaluation of Gas Chromatography-Atmospheric Pressure Chemical Ionization-Time-of-Flight Mass Spectrometry for Metabolic Fingerprinting and Profiling. *Anal Chem* **2011,** *83* (19), 7514-7522.

9. Portoles, T.; Sancho, J. V.; Hernandez, F.; Newton, A.; Hancock, P., Potential of atmospheric pressure chemical ionization source in GC-QTOF MS for pesticide residue analysis. *J Mass Spectrom* **2010,** *45* (8), 926-936.

10. Pacchiarotta, T.; Nevedomskaya, E.; Carrasco-Pancorbo, A.; Deelder, A. M.; Mayboroda, O. A., Evaluation of GC-APCI/MS and GC-FID as a complementary platform. *J Biomol Tech* **2010,** *21* (4), 205-13.

11. Matysik, S.; Schmitz, G.; Bauer, S.; Kiermaier, J.; Matysik, F. M., Potential of gas chromatography-atmospheric pressure chemical ionization-time-of-flight mass spectrometry for the determination of sterols in human plasma. *Biochem Bioph Res Co* **2014,** *446* (3), 751-755.

12. Pacchiarotta, T.; Derks, R. J. E.; Hurtado-Fernandez, E.; van Bezooijen, P.; Henneman, A.; Schiewek, R.; Fernandez-Gutierrez, A.; Carrasco-Pancorbo, A.; Deelder, A. M.; Mayboroda, O. A., Online spectral library for GC-atmospheric pressure chemical ionization-ToF MS. *Bioanalysis* **2013,** *5* (12), 1515-1525.

13. Ostman, P.; Luosujarvi, L.; Haapala, M.; Grigoras, K.; Ketola, R. A.; Kotiaho, T.; Franssila, S.; Kostiainen, R., Gas chromatography-microchip atmospheric pressure chemical ionization-mass spectrometry. *Anal Chem* **2006,** *78* (9), 3027-3031.

14. Sunner, J.; Nicol, G.; Kebarle, P., Factors Determining Relative Sensitivity of Analytes in Positive Mode Atmospheric-Pressure Ionization Mass-Spectrometry. *Anal Chem* **1988,** *60* (13), 1300-1307.

15. Klee, S.; Derpmann, V.; Wissdorf, W.; Klopotowski, S.; Kersten, H.; Brockmann, K. J.; Benter, T.; Albrecht, S.; Bruins, A. P.; Dousty, F.; Kauppila, T. J.; Kostiainen, R.; O'Brien, R.; Robb, D. B.; Syage, J. A., Are Clusters Important in Understanding the Mechanisms in Atmospheric Pressure Ionization? Part 1: Reagent Ion Generation and Chemical Control of Ion Populations. *J Am Soc Mass Spectr* **2014,** *25* (8), 1310-1321.

16. Newsome, G. A.; Ackerman, L. K.; Johnson, K. J., Humidity Effects on Fragmentation in Plasma-Based Ambient Ionization Sources. *J Am Soc Mass Spectr* **2016,** *27* (1), 135-143.

17. Newsome, G. A.; Ackerman, L. K.; Johnson, K. J., Humidity Affects Relative Ion Abundance in Direct Analysis in Real Time Mass Spectrometry of Hexamethylene Triperoxide Diamine. *Anal Chem* **2014,** *86* (24), 11977-11980.

18. Wachsmuth, C. J.; Dettmer, K.; Lang, S. A.; Mycielska, M. E.; Oefner, P. J., Continuous Water Infusion Enhances Atmospheric Pressure Chemical Ionization of Methyl Chloroformate Derivatives in Gas Chromatography Coupled to Time-of-Flight Mass Spectrometry-Based Metabolomics. *Anal Chem* **2014,** *86* (18), 9186-9195.

19. Hunter, E. P.; Lias, S. G., Proton Affinity Evaluation. In *NIST Chemistry WebBook, NIST Standard Reference Database Number 69*, Linstrom, P. J.; Mallard, W. G., Eds. National Institute of Standards and Technology: Gaithersburg MD, 20899.

20. Rocha, I. M.; Galvão, T. L. P.; Sapei, E.; Ribeiro da Silva, M. D. M. C.; Ribeiro da Silva, M. A. V., Levoglucosan: A Calorimetric, Thermodynamic, Spectroscopic, and Computational Investigation. *Journal of Chemical & Engineering Data* **2013,** *58* (6), 1813-1821.

21. Lias, S. G., Ionization Energy Evaluation. In *NIST Chemistry WebBook, NIST Standard Reference Database Number 69*, Linstrom, P. J.; Mallard, W. G., Eds. National Institute of Standards and Technology: Gaithersburg MD, 20899.

22. Brown, R. J. C., Hydrogen bonding of the ammonium ion. *Journal of Molecular Structure* **1995,** *345*, 77-81.

Supplemental Information

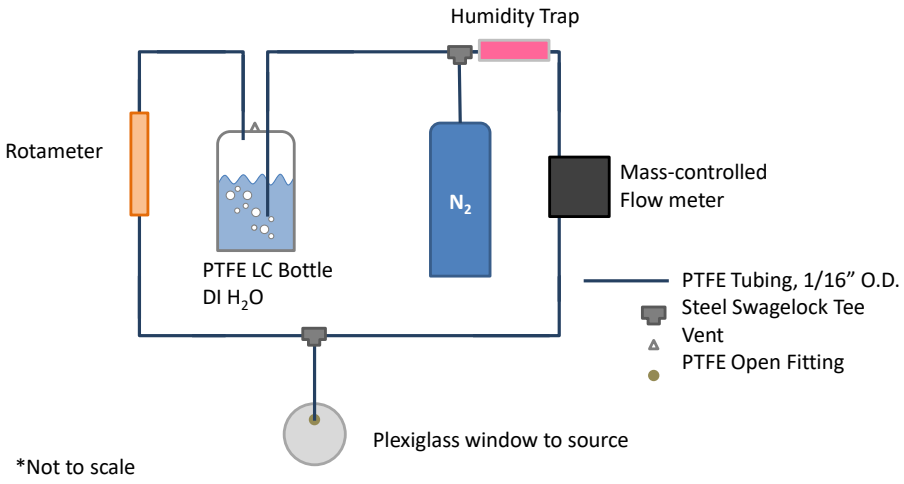

Figure S1. Schematic of the humidification system.

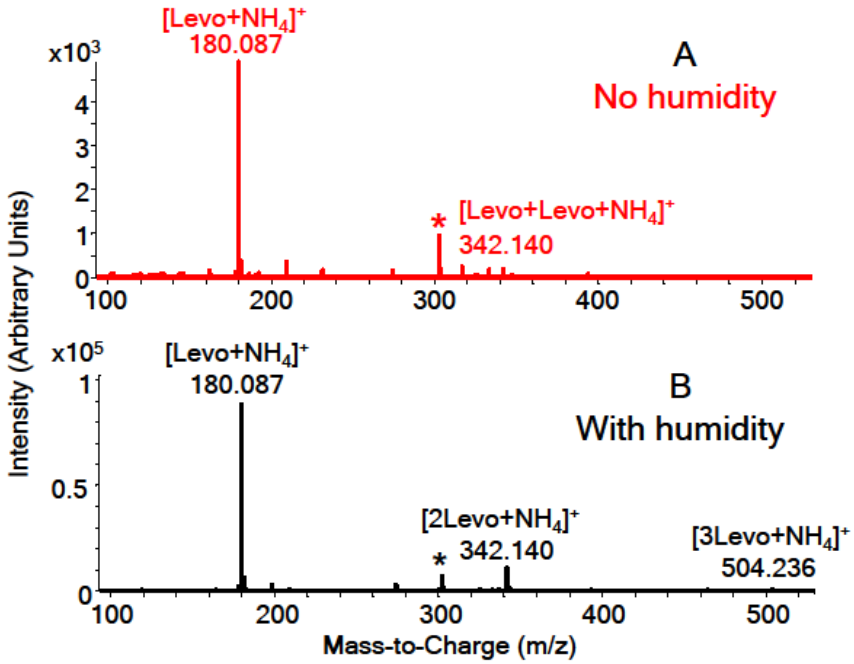

Figure S2. Mass spectra of levoglucosan (A) before and (B) after addition of water to the source.

CHAPTER 4

EVALUATION OF PRIMARY REACTION PATHWAYS IN THIN-FILM PYROLYSIS OF GLUCOSE USING ^{13}C-LABELING AND REAL-TIME MONITORING

A manuscript to be submitted to *ACS Sustainable Chemistry & Engineering*

Carolyn P. Hutchinson and Young Jin Lee

Abstract

There recently has been progress on the fundamental understanding of fast pyrolysis as a promising strategy for biorenewable energy. An example of this progress is the dissection of bulk-sum models into individual molecular reactions as an effort to explain and predict the product yields in biomass pyrolysis. However, rigorous efforts have been scarce to experimentally validate each molecular reaction in pyrolysis. In this work, we evaluate molecular reaction mechanisms in the pyrolysis of glucose labeled with ^{13}C on the C-1, C-3, or C-6 positions. We adopt a novel experimental system that we have recently developed to study isothermal reaction kinetics with a very short reactor residence time (~0.2 s) in virtual real-time, which is ideally suited to correlate the results with primary reactions in theoretical modeling. We were able to support the previously proposed primary reaction mechanism for $C_4H_8O_4$ (erythrose) but rejects those for $C_3H_6O_3$ (dihydroxyacetone and glyceraldehyde) and $C_3H_6O_2$ (acetol). Alternative reaction pathways proposed to explain our data suggest that retro aldol reaction is much more efficient than Grob fragmentation in general.

Introduction

Fast pyrolysis of lignocellulosic biomass offers a promising solution to the ever-growing demand for fossil fuels.[1-2] Cellulose, the most abundant (40-60 wt% typically) and least complex major component of lignocellulosic biomass, is most widely studied.[3-5] The reaction kinetics are often described by lump-sum models, the most representative of which is the Broido-Shafizadeh model.[4-8] In this model, cellulose is first transformed to "active cellulose" then converted to one of two lumped categories of products: volatiles (i.e., bio-oil) or solids and gases (i.e., char and non-condensable gases). While these lump-sum models provide empirical correlation for the overall yields, they do not explain the decomposition pathways in molecular detail. Furthermore, the kinetics parameters obtained with lump-sum models do not agree with one another, raising serious limitations of the model.[4-5, 9]

Recently, efforts have been made to address the shortcomings of the lump-sum model and provide molecular-level understanding of fast pyrolysis. Assary and Curtiss used quantum-chemical and statistical-mechanical calculations to model the decomposition of glucose and fructose.[10] Vasiliu et al. also used computational chemistry to predict the reactions of key biomass intermediates, including glucose.[11] Seshadri and Westmoreland used similar approach to model glucose pyrolysis.[12] A mechanistic model was proposed by Vinu and Broadbelt to explain cellulose pyrolysis using a complex network of elementary molecular reactions.[13] This was further refined by fitting into experimental data.[14-15] While this approach provides the first significant effort to understand molecular kinetics of all the products in fast pyrolysis, the proposed reaction mechanisms and kinetics parameters are yet to be validated individually. There have been

some previous efforts to study the elementary reactions in fast pyrolysis of glucose or small glucans using ^{13}C-labeling.[16-20] Partial mechanistic understanding could be made to qualitatively explain a portion of the pyrolysis reactions; however, the product distribution is obscured, mostly due to significant fragmentation and low mass resolution in typical GC-MS analysis.

It has been well known that glucose pyrolysis produces significantly different product distribution from that of cellulose pyrolysis mostly due to the lack of glycosidic bonds.[13] However, studying the mechanisms of glucose pyrolysis is still of significant interest since it is both the monomer unit of cellulose and an intermediate of cellulose pyrolysis. Sanders, et al. showed the same products are produced with different yields when the pyrolysis of monosaccharides is compared to the pyrolysis of cellulose.[21] Additionally, although cellulose pyrolysis reaction is dominated by glycosidic bond cleavage, many of the small molecular products occur from the same or similar intermediates of glucose pyrolysis.

We have recently developed an analytical instrumentation for the real-time monitoring of fast pyrolysis products.[22] By directly connecting a drop-in micropyrolyzer with a high-resolution time-of-flight mass spectrometer (TOF MS) through dopant-assisted atmospheric pressure chemical ionization (dAPCI), we can monitor each pyrolysis product in virtually real-time with 0.1 second temporal resolution. In our approach, the pyrolysis reaction occurs in isothermal kinetic conditions using thin-film pyrolysis, and the reactor residence time is minimized to ~0.2 s using film deposition on the outside of the cup. New insight has been obtained in molecular-level understanding of fast pyrolysis by studying the pyrolysis of glucose and its oligomers with various chain

lengths. Using this technology, here we investigate the elementary reaction mechanisms in glucose pyrolysis by labeling select positions with ^{13}C isotope. By monitoring whether the ^{13}C label is maintained in the products, several key reaction pathways in glucose pyrolysis could be tested for their support or invalidation. GC separation is also utilized when necessary to further separate structural isomers and obtain deeper insight into the mechanism.

Methods

Materials & Sample Preparation

Unlabeled ($^{12}C_6$-) glucose, unlabeled ($^{12}C_6$-) levoglucosan, and $^{13}C_6$-glucose were obtained from Sigma-Aldrich (St. Louis, MO). $^{13}C_6$-levoglucosan, ^{13}C-1-glucose, ^{13}C-3-glucose, and ^{13}C-6-glucose were obtained from Carbosynth, LLC (San Diego, CA). All carbohyrdates used had a minimum purity of 99%. Samples were introduced by preparing thin films on the upper outside rim of a deactivated stainless steel sample cup on one side and spotting $^{13}C_6$-levoglucosan on the other side as an internal standard. For real-time analysis, 0.5 μg of glucose (labeled or unlabeled) (0.5 μL of 1 mg mL^{-1} in water) and 0.05 μg of $^{13}C_6$-levoglucosan (0.5 μL of 0.1 mg mL^{-1}) were used, yielding a glucose film of approximately 4-5 μm thickness (calculated). For GC separation analysis, 15 μg of glucose (labeled or unlabeled) and 0.10 μg of $^{13}C_6$-levoglucosan were used by spotting multiple position along the outer rim. For $^{13}C_6$-glucose pyrolysis, unlabeled levoglucosan was spotted instead of labeled levoglucosan as an internal standard and time calibrant; otherwise the procedure is the same.

Mass Spectrometry Analysis

After the films were dried using an in-house vacuum, these cups are introduced to the μPy-dAPCI-TOF MS system (Figure S1) via an auto shot sampler (AS-1020E; Frontier Laboratories, Fukushima, Japan) and a drop-in micropyrolyzer (μPy) (3030S; Frontier) mounted on the inlet of a gas chromatograph (GC) (7890A; Agilent Technologies, Palo Alto, CA). For real-time analysis, a deactivated fused silica transfer line (SGE Incorporated, Pflugerville, TX) with 0.6 m length (100 μm I.D.) is used to directly connect GC injection port and a time-of-flight mass spectrometer (TOF MS) (Agilent 6224). The GC inlet, GC-APCI interface, μPy interface, and oven temperatures are all set to 280 °C and the inlet split is set at 100:1 (100 mL min^{-1} through the micropyrolyzer, 1 mL min^{-1} through the transfer line). The μPy furnace is maintained at 500 ºC. For GC separation, a low/mid-polarity column (ZB-1701, 30 m x 0.25 mm x 0.25 μm; Phenomenex, Torrance, CA) is used for the GC separation. The GC temperature was programmed to set at 35 °C for 1 min, ramped to 280 °C at 20 °C min^{-1}, then held for 3 min. A dopant-assisted APCI source is used with a GC-APCI interface (Agilent 3212) with ammonia (500 ppm in helium; Praxair, Hillside, IL) as a dopant gas. The ionization source is humidity controlled using a 1:1 mixed gas flow of dry nitrogen and fully humidified nitrogen bubbled through water.

Results and Discussion

A novel analytical system developed by our group for the study of biomass pyrolysis in real-time was used for the current study. The schematic diagram is shown in

Figure S1 and described in details elsewhere.[22] Briefly, biomass materials (glucose in this study) are pyrolyzed using a drop-in microfurnance and the pyrolyzates are immediately delivered by helium carrier gas to a TOF MS. We use thin-film pyrolysis to obtain a high heating rate (~5 ms to heat up to 500 °C)[23] and dAPCI as a soft ionization technique to ionize carbohydrate pyrolyzates as ammonium adducts without any fragmentation. This is in contrast to electron ionization (EI) commonly used in GC-MS which produces significant fragmentation and cannot trace each ion without chromatographic separation. Pseudo real-time monitoring of pyrolysis products is achieved by this combination of soft ionization of all the products and high-mass resolution TOF MS analysis. We load samples as a thin film, which not only ensures isothermal kinetics[24] but also minimizes pyrolysis occurring in the molten phase.[25] Additionally, the thin film is deposited on the top outside rim of the sample cups to reduce the reactor residence time to only ~0.2 s.[22] Secondary reactions can occur in the vapor phase either inside the reactor or in the transfer line. Because of the short reactor residence time (~0.2 s) and the low temperature in the dead zone (280 °C), we hypothesize that these secondary vapor phase reactions are minimal compared to primary pyrolysis. This is supported by the lack of oligomeric compounds (e.g., cellobiosan) in thin-film glucose pyrolysis.[22] Some pyrolysis reactions discussed in the current work, however, might still occur in the vapor phase mostly before escaping the reactor.

As described elsewhere,[22] glucose is pyrolyzed in less than half second in isothermal kinetics at 500 °C, and the time profile of each product could be monitored by tracing each ion signal with a narrow mass window (0.1 u). $^{13}C_6$-levoglucosan is spotted on the other side of the sample cup and used as a pyrolysis time calibrant, as it only

evaporates from the surface without pyrolysis. Prior to the pyrolysis of glucose labeled with ^{13}C at various carbon positions, the pyrolysis of unlabeled ($^{12}C_6$) and fully labeled ($^{13}C_6$) glucose was compared to test for any isotopic effects. Figure 1 shows overlaid temporal profiles of each pyrolysis product from $^{12}C_6$-glucose and $^{13}C_6$-glucose. There is no significant difference in the relative abundance between $^{12}C_6$- and $^{13}C_6$-pyrolysis products except for slight signal variation for some low abundance compounds (e.g., $C_3H_4O_2$). This suggests that isotopic labeling does not influence pyrolysis product yields (i.e., no kinetic isotope effect), and selective isotopic labeling can be applied in order to explore mechanistic pathways.

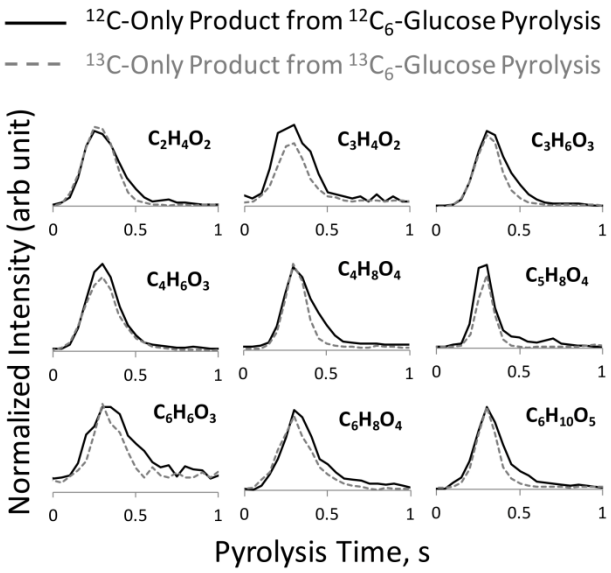

Figure 1. Real-time profiles of each product in the pyrolysis of $^{12}C_6$-glucose and $^{13}C_6$-glucose, normalized to the ion signals for internal standard of $^{13}C_6$- and $^{12}C_6$-levoglucosan, respectively.

Thin films of glucose labeled with stable ^{13}C on either the carbon-1, carbon-3, or carbon-6 positions were individually pyrolyzed and monitored by the dAPCI-TOF MS

system in order to explore reaction mechanisms. If the labeled carbon is maintained in a pyrolysis product, the isotopically labeled product (M+1 peak) will be detected; otherwise the unlabeled product (M peak) will be detected. When multiple, competing reactions occur, both M and M+1 ions can be detected with the product ratios corresponding to the ratio of reaction rates. There is contribution from natural ^{13}C isotope abundance to M+1 product yield (1.1% for each carbon), as well as contribution to M product yield from ^{12}C impurity in the stable-isotope labeled glucose (≤1%). The ^{12}C impurity has been measured to be 1 % for ^{13}C-1-glucose, 0.7 % for ^{13}C-3-glucose, and 0.6 % for ^{13}C-6-glucose according to direct infusion ESI-TOF MS analysis (Figure S2). Based on these findings, the contribution of natural ^{13}C or impurity ^{12}C is largely ignorable. It is difficult to accurately obtain product yields in this experiment due to the uncertainty in ionization efficiency. Under the assumption that the ionization efficiency is proportional to the number of carbons and the number of oxygens of each product, the yields of selected products in thin-film glucose pyrolysis are summarized in Table S1.

All C_6 products are simply produced by the loss of one, two, or three waters from glucose and are expected to exhibit only the M+1 ion regardless of which carbon is labeled. This is because all six carbons are maintained in the final products. Figure 2 shows the time profiles from $C_6H_{10}O_5$ (levoglucosan, *m/z* 180/181 as ammonium adduct) as an example of a C6 product. As expected, the pyrolysis of all three glucoses produced M+1 peak almost exclusively. There is an ignorable amount of M ion observed, mostly from ^{12}C impurity in the labeled glucose. All other C6 compounds such as $C_6H_8O_4$ (*m/z* 162/163 as ammonium adduct) and $C_6H_6O_3$ (*m/z* 144/145 as ammonium adduct) show

identical behavior. Though these C_6 compounds do not provide useful mechanistic information, they support the validity of the proposed method.

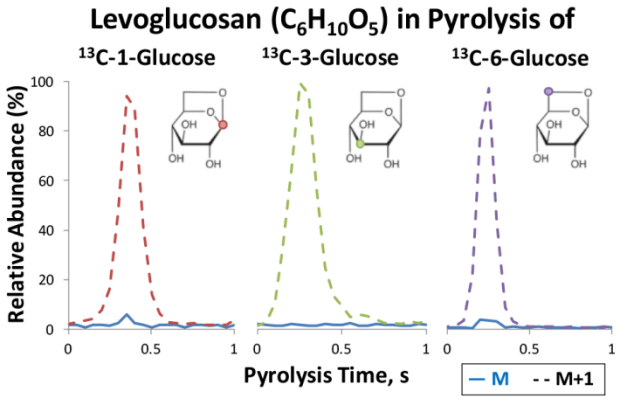

Figure 2. Real-time pyrolysis profiles of levoglucosan detected as an ammonium adduct, $[C_6H_{10}O_5+NH_4]^+$, at *m/z* 180 (M, solid) or *m/z* 181 (M+1, dashed) from the thin-film pyrolysis of glucose with ^{13}C label at carbon-1 (red), carbon-3 (green), or carbon-6 (purple) positions.

Erythrose is the only chemical composition of $C_4H_8O_4$ proposed to be present in the reaction pathway of glucose pyrolysis by Zhou et al.;[14] however, it has not been observed in Py-GC-MS data. It has been attributed largely to the instability of this compound and/or absence of EI-MS spectra in NIST library.[22] Scheme 1 is the proposed mechanism by Zhou et al.[14] for the formation of this C4 compound. Cyclic form of D-glucose is in equilibrium with linear form of D-glucose, which then breaks down via a retro aldol reaction to produce erythrose and glycolaldehyde. According to the mechanism, erythrose is expected to contain carbons 3-6 and glycolaldehyde should contain carbons 1 and 2. This means that when ^{13}C-3-glucose or ^{13}C-6-glucose is pyrolyzed, only the M+1 peak should be observed, and when ^{13}C-1-glucose is pyrolyzed, only the M peak should be observed for erythrose. The time profiles for the unlabeled and

labeled $C_4H_8O_4$ are shown in Figures 3 in the pyrolysis of ^{13}C-1-, ^{13}C-3-, and ^{13}C-6-glucose. The product is mostly unlabeled when ^{13}C-1-glucose is pyrolyzed (dominated by M), and the product is mostly labeled when ^{13}C-3-glucose or ^{13}C-6-glucose are pyrolyzed (dominated by M+1). Thus, our data support Scheme 1 is the major production pathway of $C_4H_8O_4$, as predicted by Zhou et al.

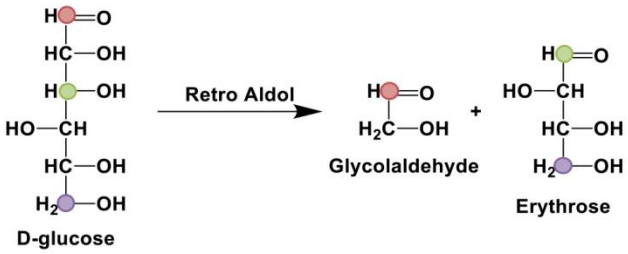

Scheme 1. Zhou et al. mechanism for the formation of erythrose ($C_4H_8O_4$).

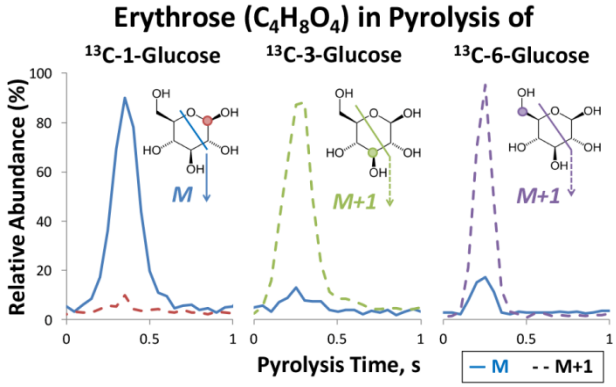

Figure 3. Real-time pyrolysis profiles of *m/z* 138 (M, solid) and *m/z* 139 (M+1, dashed) corresponding to the ammonium adduct of erythrose, $[C_4H_8O_4+NH_4]^+$, from the thin-film pyrolysis of glucose with ^{13}C label at the carbon-1 (red), carbon-3 (green), or carbon-6 (purple) positions.

In the Zhou et al. model,[14] there is only one reaction pathway that yields $C_3H_6O_3$, shown in Scheme 2. Linear form of D-glucose undergoes Grob fragmentation to produce pyruvaldehyde and glyceraldehyde; glyceraldehyde then isomerizes to form prop-1-ene which tautomerizes to form dihydroxyacetone. Dihydroxyacetone is assumed to be the

final product through isomerization because it is the only product they could detect in their Py-GC-MS analysis. All three $C_3H_6O_3$ isomers are made of carbons 1-3 and pyruvaldehyde ($C_3H_4O_2$) consists of carbons 4-6. Accordingly, this mechanism predicts to detect only the M+1 peak as the product of $C_3H_6O_3$ in the pyrolysis of ^{13}C-1- or ^{13}C-3-glucose, and only the M peak in the pyrolysis of ^{13}C-6-glucose, regardless which structural isomer of $C_3H_6O_3$ is detected. However, our experimental data is quite different from this prediction, as shown in Figure 4A. When ^{13}C-1- or ^{13}C-3-glucose is pyrolyzed, both M and M+1 ions are detected with a ratio of 2:1 and this ratio is reversed when ^{13}C-6-glucose is pyrolyzed. This suggests that there are at least two mechanisms leading to $C_3H_6O_3$, and only 1/3 of the products are in agreement with Zhou et al.

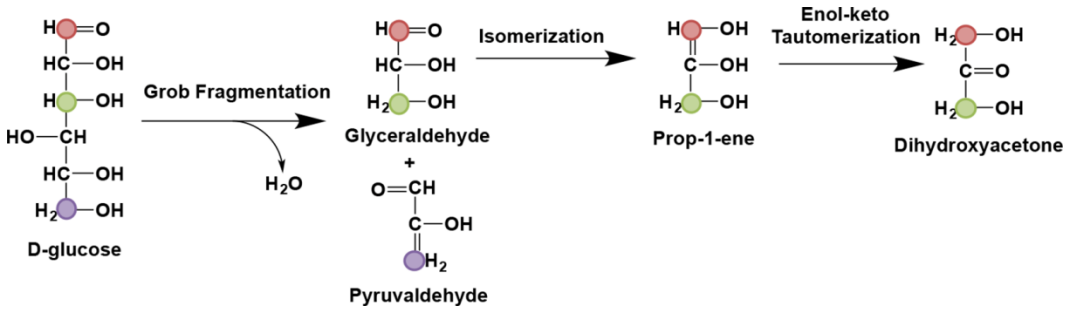

Scheme 2. Zhou et al. mechanism for the formation of $C_3H_6O_3$ (glyceraldehyde and its structural isomers).

The difference in the results from the proposed mechanism might be a consequence of structural isomers of $C_3H_6O_3$, which cannot be determined without chromatographic separation. GC separation is adopted by adding a GC column in place of the short transfer line. This allows for the separate detection of isomers but sacrifices real-time analysis. While three structural isomers for $C_3H_6O_3$ are proposed in glucose pyrolysis (Scheme 2), only two peaks are observed in μPy-GC-dAPCI-TOF MS. This occurs not only for

glucose but also cellobiose and cellotriose (Figure S3A). These two peaks are assigned as glyceraldehyde and dihydroxyacetone according to standard analysis (Figure S3B).

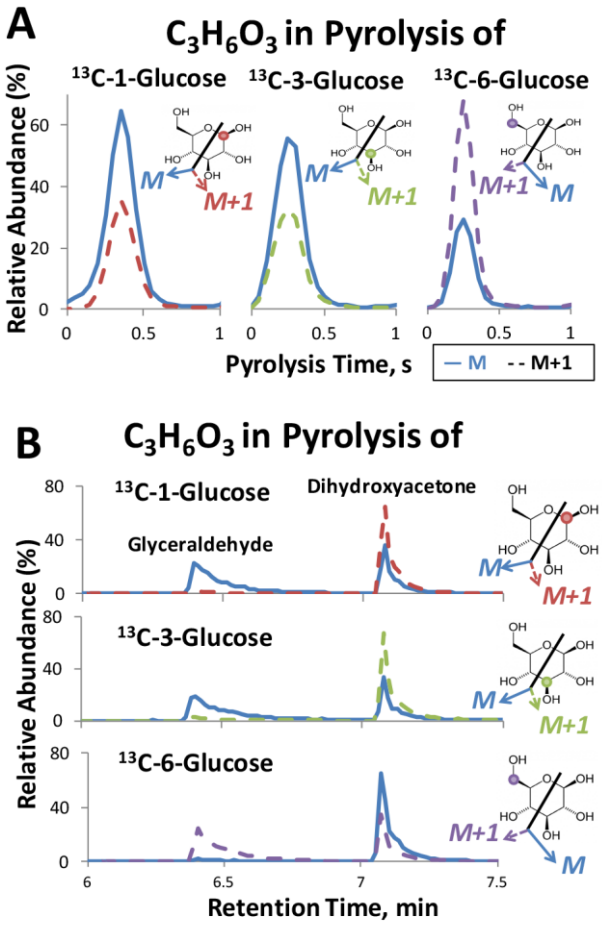

Figure 4. (A) Real-time pyrolysis profiles and (B) GC separated profiles of $C_3H_6O_3$ as an ammonium adduct, $[C_3H_6O_3+NH_4]^+$, at *m/z* 108 (M, solid) or *m/z* 109 (M+1, dashed) from the thin-film pyrolysis of glucose with ^{13}C label at the carbon-1 (red), carbon-3 (green), or carbon-6 (purple) positions.

Glyceraldehyde is an interesting compound; it is has not been reported in traditional Py-GC-MS of biomass or GC-MS of bio-oils due to its thermal instability resulting in short lifetimes in GC conditions and/or fragility in hard EI conditions resulting in spectra that could not be identified confidently. However, we could detect this compound with our

gentle dAPCI-TOF MS system with a short GC temperature program (~15 min). Equimolar amounts of glyceraldehyde and dihydroxyacetone standards were run on our GC-dAPCI-TOF MS system without pyrolysis, seen in Figure S3B, showing the survival of glyceraldehyde. There is a significant difference in the yields between the two isomers due to the survival differences in GC conditions. When equimolar amounts of glyceraldehyde and dihydroxyacetone are directly injected and analyzed with an FID connected to a catalytic PolyARC reactor,[26] approximately 14% of glyceraldehyde survives compared to dihydroxyacetone under identical conditions (Figure S3C), which is the same as the survival in GC-dAPCI-TOF MS. This is due to the fact that glyceraldehyde partially breaks down under typical GC conditions, most likely in the high temperature injection port.

Figure 4B shows the $C_3H_6O_3$ products in the pyrolysis of the three labeled glucoses after gas chromatographic separation; these appear at 6.40 and 7.08 min, corresponding to glyceraldehyde and dihydroxyacetone. The glyceraldehyde peak at 6.40 min shows only the M peak when ^{13}C-1- or ^{13}C-3-glucose is pyrolyzed and only the M+1 peak when ^{13}C-6-glucose is pyrolyzed. This suggests that glyceraldehyde is made of only carbons 4-6 and there is only one pathway to form glyceraldehyde, which is contradictory to Scheme 2. The dihydroxyacetone peak at 7.08 min has a 1:2 ratio of M to M+1 ions for ^{13}C-1- or ^{13}C-3-glucose pyrolysis and a 2:1 M to M+1 ratio for ^{13}C-6-glucose pyrolysis. This means that there are at least two reaction pathways leading to dihydroxyacetone, with the major pathway, which explains 2/3 of the products, potentially in agreement with the proposed mechanism in Scheme 2.

To explain glyceraldehyde composed of carbons 4-6, we propose an alternative mechanism as shown in Scheme 3. In this mechanism, linear form of D-glucose isomerizes to form linear form of D-fructose, which breaks apart into dihydroxyacetone with carbons 1-3 and glyceraldehyde with carbons 4-6 via a retro-aldol reaction. The proposed mechanism can explain all glyceraldehyde having carbons 4-6 and the majority of dihydroxyacetone with carbons 1-3 in Figure 4B. The minor amount of dihydroxyacetone with carbons 4-6 could be also explained as the partial isomerization of glyceraldehyde in Scheme 3. This mechanism is also proposed by Seshadri and Westmoreland as the most efficient breakdown reaction occurring from linear form of D-fructose.[12] Assary and Curtiss have also shown this pathway to be efficient.[10] The retro aldol reaction rate of Scheme 3 to form glyceraldehyde is much faster (331 s^{-1} at 500 °C)[12] than the reaction rate to form glyceraldehyde through Grob fragmentation in Scheme 2 (2.1 s^{-1} at 500 °C).[14] Glucose-to-fructose isomerization reaction (the first reaction of Scheme 3; 15.4 s^{-1} at 500 °C)[14] would be the rate determining step, but still the overall reaction rate (~14.7 s^{-1}; see supplementary discussion) would be faster than Scheme 2. They also predicted glyceraldehyde might efficiently fragment to form formaldehyde and ethene-diol (400 s^{-1} at 500 °C), which explains instability of glyceraldehyde at pyrolysis temperatures. However, our data suggests glyceraldehyde could still survive a very short reactor residence time in our instrumentation (0.2 s). In fact, $C_3H_6O_3$ is the product with the highest yield in thin-film glucose pyrolysis in real-time monitoring.[22] When we pyrolyzed thin film of glucose inside the cup (reactor residence time of ~0.6 s), we detect 1/3 as much glyceraldehyde and 1/2 as much dihydroxyacetone while more C6 products are detected (Figure S4). It should be noted

that this pathway, or any other pathways proposed later, is not the definitive mechanism but is strongly supported by our data and previous studies. We cannot exclude the possibility that other pathways may exist that can also explain our data.

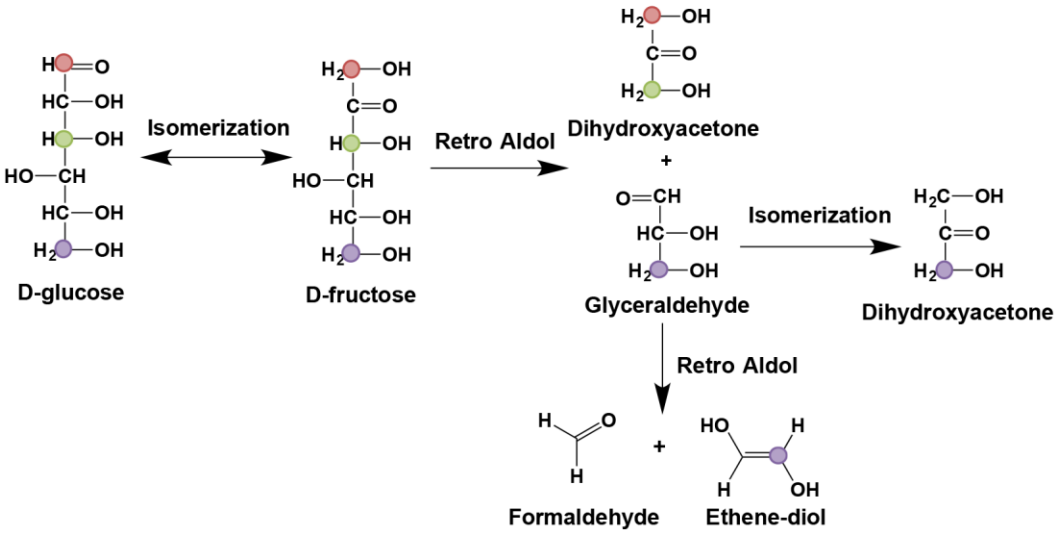

Scheme 3. Our proposed mechanism for the formation of $C_3H_6O_3$ (glyceraldehyde and/or dihydroxyacetone).

Acetol ($C_3H_6O_2$) is another product investigated to study the proposed mechanism. Two reaction pathways are proposed by Zhou et al. for this compound (Scheme 4).[14] One pathway has erythrose ($C_4H_8O_4$) as an intermediate; the pathway to form this product has previously been shown to be supported by our data (Scheme 1 and Figure 3). Erythrose can dehydrate, tautomerize, then decarbonylate to produce acetol (bottom pathway of Scheme 4). The other pathway (top pathway of Scheme 4) ultimately results in the same products of glycolaldehyde and acetol. In both the pathways, acetol is produced with carbons 4-6. However, our real-time analysis of ^{13}C-labeled $C_3H_6O_2$ almost completely disagrees with this mechanism (Figure 5A), with a majority of $C_3H_6O_2$ composed of carbons 1-3. To ensure that there were no additional isomers, gas

chromatographic separation was also performed (Figure 5B), and only a single chromatographic peak was observed at 4.03 min, which corresponds to acetol. This peak has the same M:M+1 ratio as that observed in the real-time data. This means that there are at least two reaction pathways to form acetol, and the dominant pathway utilizes carbons 1-3.

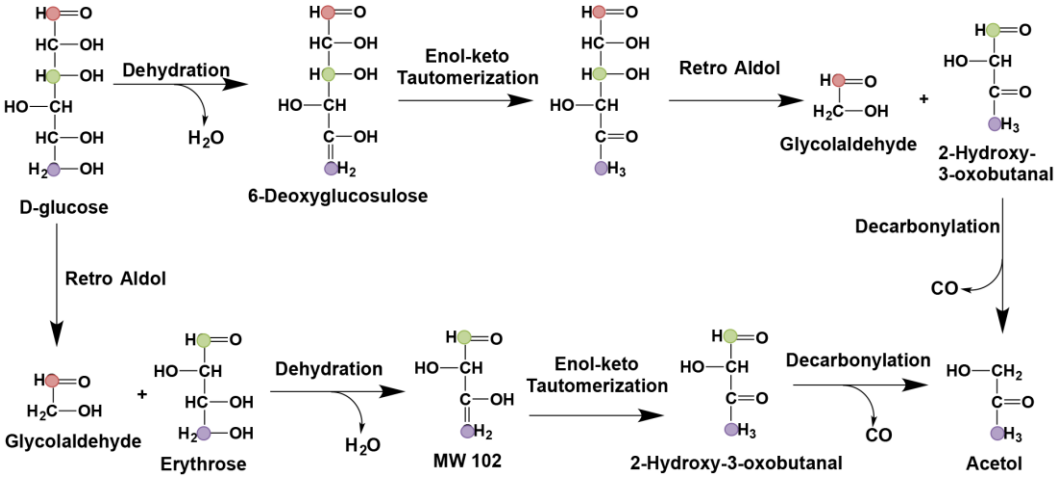

Scheme 4. Zhou et al. mechanism for the formation of $C_3H_6O_2$ (acetol).

We propose an alternative mechanism for the production of acetol as shown in Scheme 5, in which linear form of D-glucose isomerizes to linear form of D-fructose which then undergoes Grob fragmentation to produce acetol (carbons 1-3) and glyceraldehyde (carbons 4-6). This reaction mechanism is much simpler, only two steps from linear form of D-glucose, and expected to be more competitive than the pathway proposed by Zhou et al. in Scheme 4. In addition, isomerization to D-fructose has been shown to be quite efficient, and Scheme 3 could successfully explain the production of glyceraldehyde in Figure 4. It should be noted that this mechanism also produces glyceraldehyde with carbon 4-6. However, Scheme 3 is still considered to be the

dominant mechanism in the production of glyceraldehyde considering the much lower yield of acetol ($C_3H_6O_2$) compared to $C_3H_6O_3$ (only 4% of $C_3H_6O_3$ in TOF MS signal).

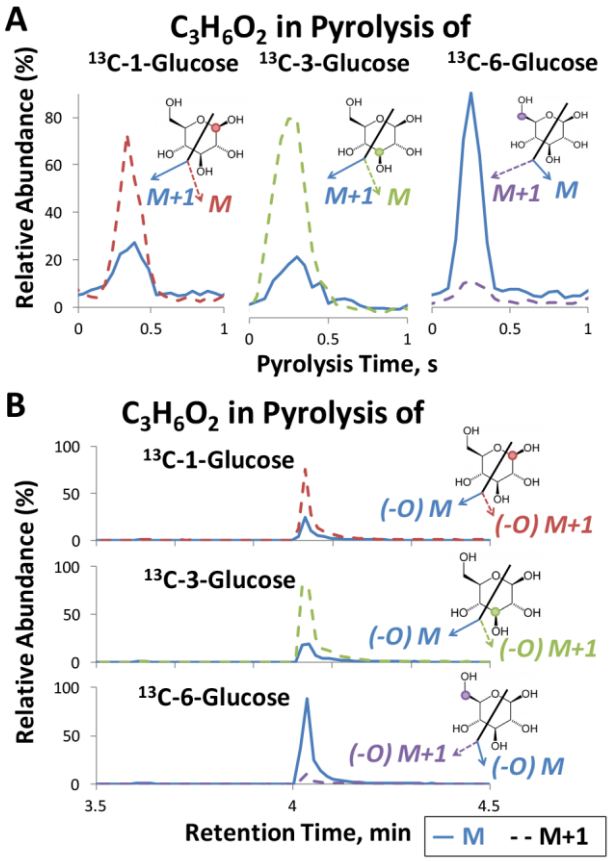

Figure 5. (A) Real-time profiles and (B) GC separated profiles of acetol as an ammonium adduct, $[C_3H_6O_2+NH_4]^+$, at *m/z* 92 (M, solid) and *m/z* 93 (M+1, dashed) from the thin-film pyrolysis of glucose with ^{13}C label on the carbon-1 (red), carbon-3 (green), or carbon-6 (purple) positions.

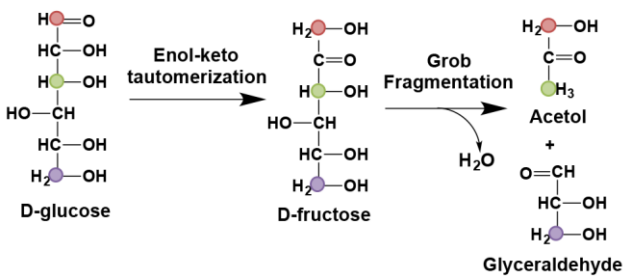

Scheme 5. Our proposed mechanism for the production of acetol ($C_3H_6O_2$).

The last compound we have closely examined was $C_2H_4O_2$, with glycolaldehyde as the dominant structural isomer, also confirmed with GC (not shown). Production of glycolaldehyde is possible through multiple reaction pathways, as can be also noted by Zhou et al.[14] As shown in Figure 6, there is 2:1 ratio of M to M+1 products for the pyrolysis of all three labeled glucoses. Among the eight mechanisms proposed by Zhou et al. leading to glycolaldehyde, two of them produce glycolaldehyde using carbons 1-2, two of them use carbons 3-4, and four of them use carbons 5-6.[14] Assary and Curtiss suggest six mechanisms for the formation of glycolaldehyde in their work; three of them use carbons 1-2, one uses carbons 3-4, and the other three use carbons 5-6.[10] Our data suggests that overall reaction pathways are equally competitive, resulting in almost equal distributions of glycolaldehyde regardless of ^{13}C position. This means that our data may not provide specific insight on the reaction mechanism for small one or two carbon products but can support the general trend for glycolaldehyde to be formed nonpreferentially from all carbon positions.

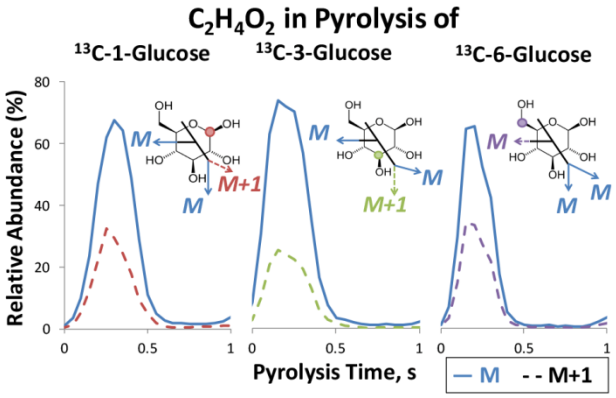

Figure 6. Real-time profiles of glycolaldehyde as an ammonium adduct, $[C_2H_4O_2+NH_4]^+$, at *m/z* 78 (M, solid) or *m/z* 79 (M+1, dashed) from the thin-film pyrolysis of glucose with ^{13}C label on the carbon-1 (red), carbon-3 (green), or carbon-6 (purple) positions.

Conclusions

By monitoring pyrolysis products of isotopically labeled glucose in virtually real-time, we have successfully evaluated a few elementary reactions in the pyrolysis of glucose with a reactor residence time of only 0.2 s. Our study supports the previously proposed retro aldol mechanism for the formation of erythrose but rejects the previously proposed Grob fragmentation for the formation of glyceraldehyde and dihydroxyacetone as well as a combined reaction of dehydration, tautomerization, retro aldol, and decarbonylation for acetol formation. Alternative mechanisms were proposed that can best explain our data: retro aldol reaction with fructose as an intermediate for glyceraldehyde formation and Grob fragmentation after tautomerization for acetol formation. If the proposed mechanisms are correct, overall this indicates that retro aldol reaction is a much more favored elementary reaction compared to Grob fragmentation. Acetol formation is an exception, where the previously proposed four consecutive reactions containing retro aldol is not as efficient as a simple two-step process with Grob fragmentation. This trend also agrees well with prior theoretical studies and the chemical reaction rates calculated from the previously reported Arrhenius parameters.

In spite of a few primary reactions successfully demonstrated, the number of mechanisms we could investigate in the current study is limited to only a few, partially due to the low abundance of some compounds and the use of only three isotopically labeled glucoses. The information obtained from this study could be used to correct reaction mechanisms and their parameters in theoretical modeling and lead to a better prediction of final product distributions.

Acknowledgements

This work is supported by National Science Foundation, Division of Chemical, Bioengineering, Environmental and Transport Systems, Energy for Sustainability Program.

Supporting Information (Description)

The supporting information is available free of charge.

Supplementary discussion on the reaction rate for glyceraldehyde formation; Figure S1, instrument schematic; Figure S2, ESI-TOF MS analysis of isotopically labeled glucoses; Figure S3, GC analysis of $C_3H_6O_3$ (A) with dAPCI-TOFMS in the pyrolysis of glucose, cellobiose, and cellulose, (B) with dAPCI-TOFMS of standards, and (C) with FID of standards; Figure S4, GC-dAPCI-TOFMS of $C_3H_6O_3$ in the pyrolysis of glucose thin films prepared inside and outside the sample cup; Table S1, carbon yields of selected products in the pyrolysis of glucose thin films; Table S2, Arrhenius reaction rates and rate parameters for glyceraldehyde formation.

References

1. Bridgwater, A. V., Review of fast pyrolysis of biomass and product upgrading. *Biomass & Bioenergy* **2012,** *38*, 68-94.

2. Huber, G. W.; Iborra, S.; Corma, A., Synthesis of transportation fuels from biomass: Chemistry, catalysts, and engineering. *Chem. Rev.* **2006,** *106* (9), 4044-4098.

3. Mettler, M. S.; Vlachos, D. G.; Dauenhauer, P. J., Top ten fundamental challenges of biomass pyrolysis for biofuels. *Energy Environ. Sci.* **2012,** *5* (7), 7797-7809.

4. Burnham, A. K.; Zhou, X.; Broadbelt, L. J., Critical Review of the Global Chemical Kinetics of Cellulose Thermal Decomposition. *Energy Fuels* **2015,** *29* (5), 2906-2918.

5. Di Blasi, C., Modeling chemical and physical processes of wood and biomass pyrolysis. *Prog. Energy Combust. Sci.* **2008,** *34* (1), 47-90.

6. Broido, A.; Nelson, M. A., Char Yield on Pyrolysis of Cellulose. *Combust Flame* **1975,** *24* (2), 263-268.

7. Bradbury, A. G. W.; Sakai, Y.; Shafizadeh, F., KINETIC-MODEL FOR PYROLYSIS OF CELLULOSE. *J. Appl. Polym. Sci.* **1979,** *23* (11), 3271-3280.

8. Shafizadeh, F.; Bradbury, A. G. W., THERMAL-DEGRADATION OF CELLULOSE IN AIR AND NITROGEN AT LOW-TEMPERATURES. *J. Appl. Polym. Sci.* **1979,** *23* (5), 1431-1442.

9. Varhegyi, G.; Jakab, E.; Antal, M. J., IS THE BROIDO-SHAFIZADEH MODEL FOR CELLULOSE PYROLYSIS TRUE. *Energy Fuels* **1994,** *8* (6), 1345-1352.

10. Assary, R. S.; Curtiss, L. A., Comparison of Sugar Molecule Decomposition through Glucose and Fructose: A High-Level Quantum Chemical Study. *Energ Fuel* **2012,** *26* (2), 1344-1352.

11. Vasiliu, M.; Guynn, K.; Dixon, D. A., Prediction of the Thermodynamic Properties of Key Products and Intermediates from Biomass. *J Phys Chem C* **2011,** *115* (31), 15686-15702.

12. Seshadri, V.; Westmoreland, P. R., Concerted Reactions and Mechanism of Glucose Pyrolysis and Implications for Cellulose Kinetics. *J. Phys. Chem. A* **2012,** *116* (49), 11997-12013.

13. Vinu, R.; Broadbelt, L. J., A mechanistic model of fast pyrolysis of glucose-based carbohydrates to predict bio-oil composition. *Energ Environ Sci* **2012,** *5* (12), 9808-9826.

14. Zhou, X. W.; Nolte, M. W.; Mayes, H. B.; Shanks, B. H.; Broadbelt, L. J., Experimental and Mechanistic Modeling of Fast Pyrolysis of Neat Glucose-Based Carbohydrates. 1. Experiments and Development of a Detailed Mechanistic Model. *Ind. Eng. Chem. Res.* **2014,** *53* (34), 13274-13289.

15. Zhou, X. W.; Nolte, M. W.; Shanks, B. H.; Broadbelt, L. J., Experimental and Mechanistic Modeling of Fast Pyrolysis of Neat Glucose-Based Carbohydrates. 2. Validation and Evaluation of the Mechanistic Model. *Ind. Eng. Chem. Res.* **2014,** *53* (34), 13290-13301.

16. Paine, J. B.; Pithawalla, Y. B.; Naworal, J. D.; Thomas, C. E., Carbohydrate pyrolysis mechanisms from isotopic labeling. Part 1: The pyrolysis of glycerin: Discovery of competing fragmentation mechanisms affording acetaldehyde and formaldehyde and the implications for carbohydrate pyrolysis. *J. Anal. Appl. Pyrolysis* **2007,** *80* (2), 297-311.

17. Paine, J. B.; Pithawalla, Y. B.; Naworal, J. D., Carbohydrate pyrolysis mechanisms from isotopic labeling. Part 2. The pyrolysis of D-glucose: General disconnective analysis and the formation of C-1 and C-2 carbonyl compounds by electrocyclic fragmentation mechanisms. *J. Anal. Appl. Pyrolysis* **2008,** *82* (1), 10-41.

18. Paine, J. B.; Pithawalla, Y. B.; Naworal, J. D., Carbohydrate pyrolysis mechanisms from isotopic labeling. Part 3. The Pyrolysis of D-glucose: Formation of C-3 and C-4 carbonyl compounds and a cyclopentenedione isomer by electrocyclic fragmentation mechanisms. *J. Anal. Appl. Pyrolysis* **2008,** *82* (1), 42-69.

19. Paine, J. B.; Pithawalla, Y. B.; Naworal, J. D., Carbohydrate pyrolysis mechanisms from isotopic labeling Part 4. The pyrolysis Of D-glucose: The formation of furans. *J. Anal. Appl. Pyrolysis* **2008,** *83* (1), 37-63.

20. Ponder, G. R.; Richards, G. N., A Review of Some Recent Studies on Mechanisms of Pyrolysis of Polysaccharides. *Biomass & Bioenergy* **1994,** *7* (1-6), 1-24.

21. Sanders, E. B.; Goldsmith, A. I.; Seeman, J. I., A model that distinguishes the pyrolysis of D-glucose, D-fructose, and sucrose from that of cellulose. Application to the understanding of cigarette smoke formation. *J Anal Appl Pyrol* **2003,** *66* (1-2), 29-50.

22. Hutchinson, C. P.; Cole, D. P.; Smith, E. A.; Lee, Y. J., Tracking Molecular Products in Fast Pyrolysis of Carbohydrates in Sub-second Temporal Resolution. *Acs Sustainable Chemistry & Engineering submitted*.

23. Mettler, M. S.; Mushrif, S. H.; Paulsen, A. D.; Javadekar, A. D.; Vlachos, D. G.; Dauenhauer, P. J., Revealing pyrolysis chemistry for biofuels production: Conversion of cellulose to furans and small oxygenates. *Energy Environ. Sci.* **2012,** *5* (1), 5414-5424.

24. Krumm, C.; Pfaendtner, J.; Dauenhauer, P. J., Millisecond Pulsed Films Unify the Mechanisms of Cellulose Fragmentation. *Chem. Mater.* **2016,** *28* (9), 3108-3114.

25. Paulsen, A. D.; Mettler, M. S.; Dauenhauer, P. J., The Role of Sample Dimension and Temperature in Cellulose Pyrolysis. *Energ Fuel* **2013,** *27* (4), 2126-2134.

26. Maduskar, S.; Teixeira, A. R.; Paulsen, A. D.; Krumm, C.; Mountziaris, T. J.; Fan, W.; Dauenhauer, P. J., Quantitative carbon detector (QCD) for calibration-free,

high-resolution characterization of complex mixtures. *Lab on a Chip* **2015,** *15* (2), 440-447.

Supporting Information

Supplementary Discussion Regarding Reaction Rate for Glyceraldehyde Formation

The first order reaction rate constant is often given by Arrhenius equation:

$$k = Ae^{-E_a/RT} \quad (1)$$

where E_a is activation energy, R is gas constant (8.314 J/mol), and T is absolute temperature (in K). A is the pre-exponential factor with the physical meaning of collision frequency for binary reactions and frequency for unimolecular reactions. Table S1 summarizes Arrhenius parameters for the formation of glyceraldehyde from D-glucose through Schemes 2 and 3. Reaction rate constant (k) is calculated according to equation (1) at the pyrolysis temperature of 500 °C. Grob fragmentation (Scheme 2) is proposed by Zhou et al.[1] for the glyceraldehyde formation, and the reaction rate constant is calculated as 2.13 s^{-1}. Retro aldol reaction from D-fructose to glyceraldehyde (Scheme 2) is proposed by Seshadri and Westmoreland,[2] and the reaction rate constant is calculated to be very high, 331 s^{-1}. Retro aldol reactions, in general, are very fast, and the rate constant is in the range of 6-2,570 s^{-1} for Zhou et al. and 27-2,591 s^{-1} for Seshadri and Westmoreland at 500 °C.

The isomerization reaction in Scheme 3 is the rate determining step for the formation of glyceraldehyde from D-glucose. The calculated isomerization reaction rate is reasonable for Zhou et al. (15.4 s^{-1}) but too low for Seshadri and Westmoreland (0.32 s^{-1}). The reaction rate of 0.32 s^{-1} corresponds to the half life time (i.e., ln2/k) of 2.2 s, but it is clear from our dataset that overall glucose pyrolysis is completed in less than a half second. Seshadri and Westmoreland also proposed water catalyzed isomerization reaction (i.e. bimolecular reaction), of which the upper limit for the pseudo first-order reaction

rate is calculated as 122 s^{-1} with the partial pressure of water as 1 atm. Hence, the isomerization reaction rate from Zhou et al. seems appropriate as it falls between the two extreme reaction rate constants by Seshardri and Westmoreland.

For the consecutive reaction, the overall reaction rate can be approximated from each half life time. Namely, $\tau_3 = \tau_1 + \tau_2$ where the half-life time of τ_i is given as $\ln 2/k_i$ for each reaction, k_1 and k_2 are rate constants of each consecutive reaction, and k_3 is the overall reaction rate constant. Hence, the overall reaction rate constant for the formation of glyceraldehyde through Scheme 3 can be estimated as $k_3 = 14.7\ s^{-1}$, from $1/k_3 = 1/(15.4\ s^{-1}) + 1/(331\ s^{-1})$, which is greater than Grob fragmentation of 2.13 s^{-1} and justifies Scheme 3 is the major reaction pathway. For the formation of glyceraldehyde and acetol in Scheme 5, the same calculation can be performed. In the assumption Grob fragmentation of Scheme 5 has the same reaction rate of Grob fragmentation of Scheme 2, the overall reaction rate constant for Scheme 5 can be calculated as 1.9 s^{-1}, from $1/k_3 = 1/(15.4\ s^{-1}) + 1/(2.13\ s^{-1})$, confirming this reaction is much slower than Scheme 3 and not a major pathway for glyceraldehyde, although it is the major pathway for acetol formation.

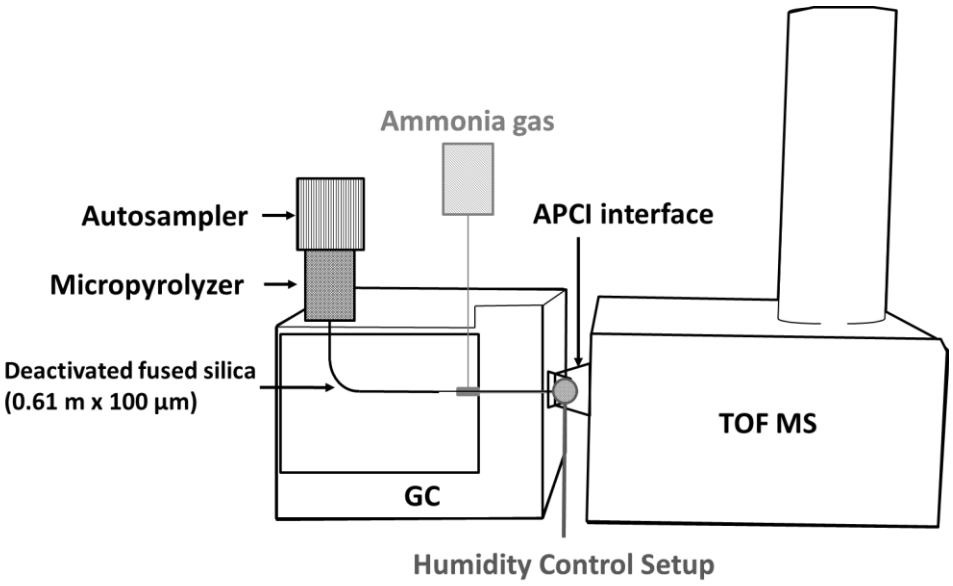

Figure S1. Schematic diagram of the instrument used in this study.

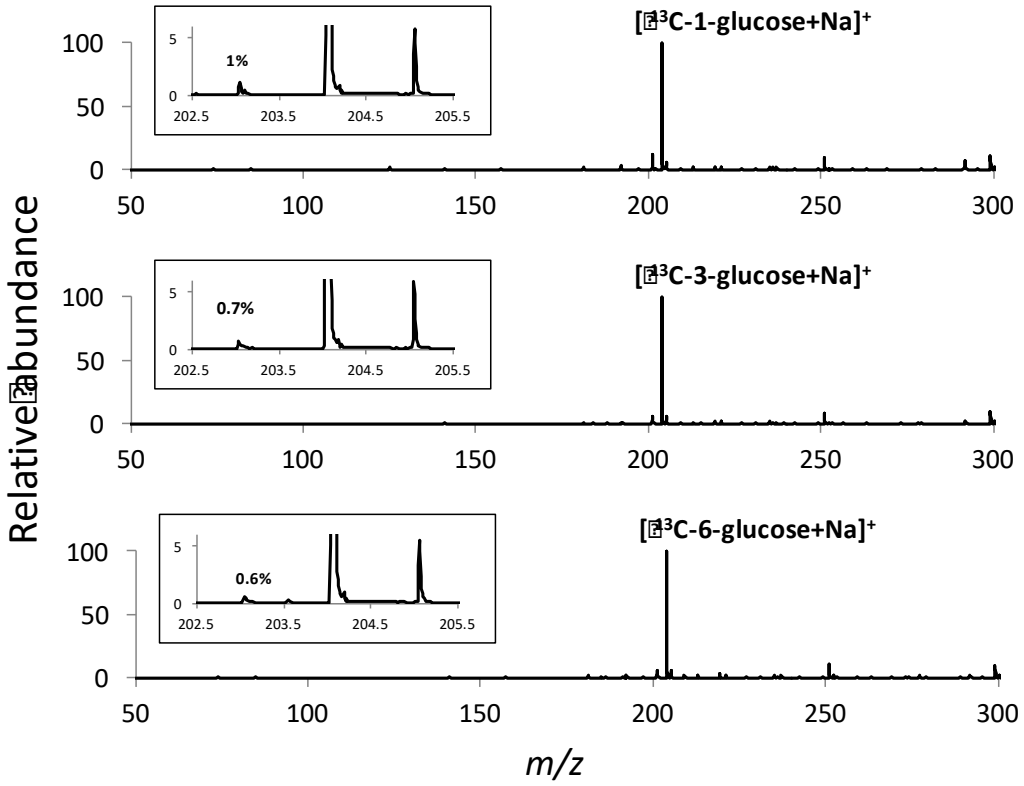

Figure S2. Direct infusion (+) ESI-TOF MS analysis of isotopically labeled glucoses. Insets are magnified views of respective ^{12}C peak.

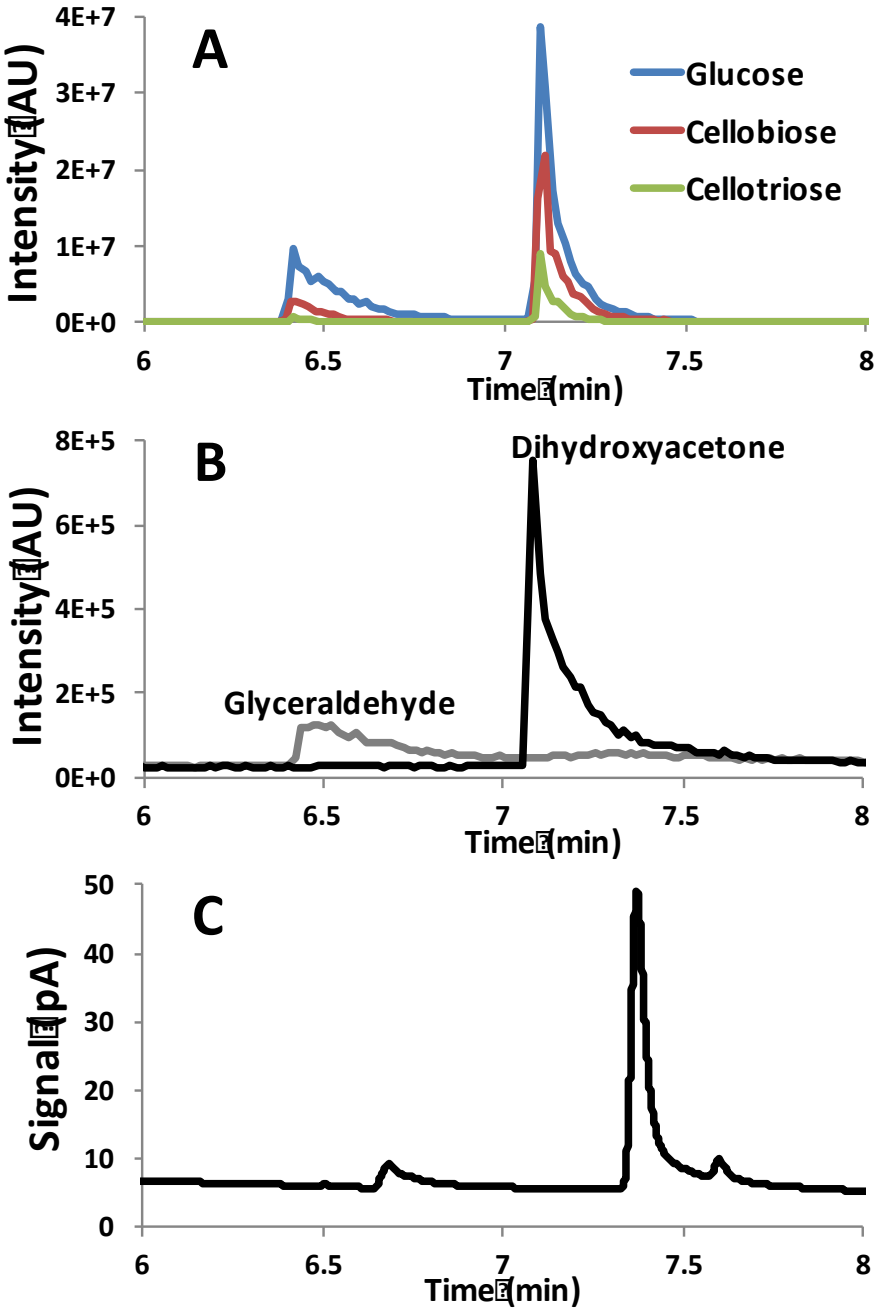

Figure S3. (A) Extracted ion chromatogram of $C_3H_6O_3$ as an ammonium adduct, $[C_3H_6O_3+NH_4]^+$, at *m/z* 108 in GC-dAPCI-TOF MS for the pyrolysis of 15 μg of glucose (red), cellobiose (green), and cellotriose (blue) showing the presence of both glyceraldehyde and dihydroxyacetone. Standard analysis of equimolar amounts of glyceraldehyde and dihydroxyacetone with (B) GC-dAPCI-TOF MS analysis and (C) GC-FID analysis. Note there is ~0.2 min time delay in FID.

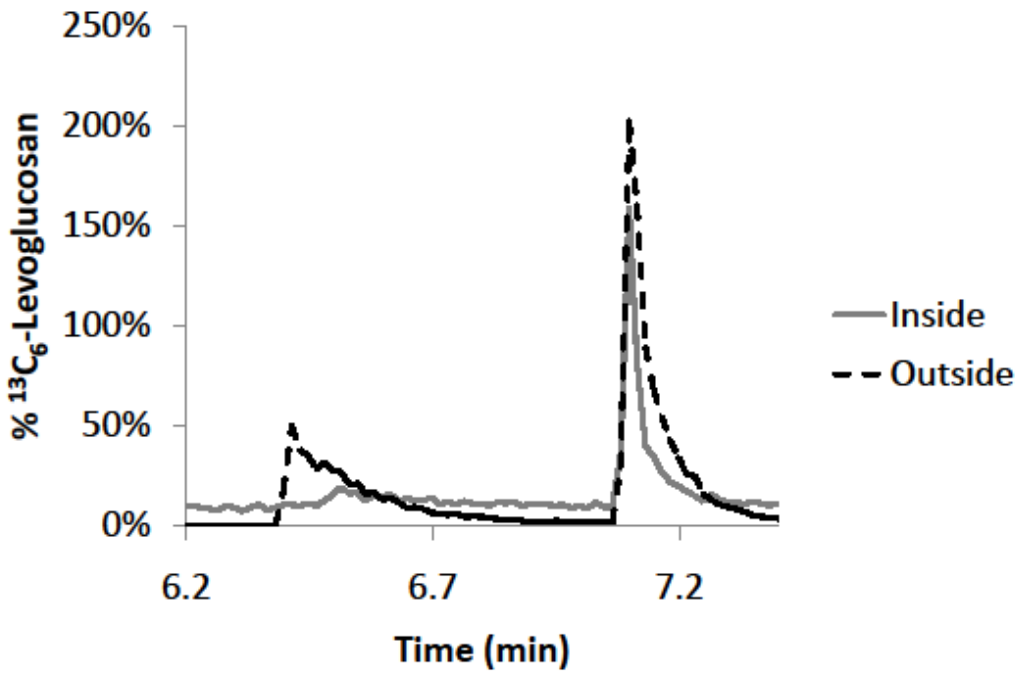

Figure S4. Extracted ion chromatograms of $C_3H_6O_3$ as an ammonium adduct, $[C_3H_6O_3+NH_4]^+$, at *m/z* 108 in Py-GC-dAPCI-TOF MS when glucose is spotted inside (grey, solid) and outside (black, dash) on the upper edge of a stainless steel sample cup.

Table S1. Carbon yield of select products in the pyrolysis of glucose thin film.

Chemical Composition	Known Products	% Carbon Yield (90% confidence interval)
$C_2H_4O_2$	glycolaldehyde	7.8 (1.6)
$C_3H_6O_3$	glyceraldehyde, dihydroxyacetone	16.6 (1.7)
$C_4H_6O_3$	-	2.8 (0.2)
$C_5H_6O_3$	-	1.1 (0.2)
$C_4H_8O_4$	erythrose	2.6 (1.2)
$C_6H_6O_3$	hydroxymethylfurfural, levoglucosenone	0.4 (0.1)
$C_5H_8O_4$	-	2.0 (0.4)
$C_6H_8O_4$	dianhydroglucopyranose	1.0 (0.3)
$C_6H_{10}O_5$	levoglucosan	2.1 (0.6)

* This data is obtained without GC separation but with high-resolution mass spectrometric separation of each product in the pyrolysis of glucose thin film. The ionization efficiency is assumed to be proportional to the product of the number of carbons and the number of oxygens, then normalized to the ionization efficiency of levoglucosan that was externally calibrated.

Table S2. Arrhenius reaction rates and rate parameters for glyceraldehyde formation.[a]

Reaction	***A*, s^{-1} [b]**	***E_a*, kcal/mol**	***k*, s^{-1}**	**Ref**
Grob fragmentation (1st rxn of Scheme 2): D-glucose → Glyceraldehyde + Pyruvaldehyde	1.5×10^{15}	52.5	2.13	Zhou
Isomerization (1st rxn of Scheme 3): D-glucose ↔ D-fructose	7.3×10^{11} 4.3×10^{10}	43.7 33.4	0.32 15.4	Seshadri Zhou
D-glucose + H_2O ↔ D-fructose + H_2O [b]	3.0×10^{11}	33.2	<122 [c]	Seshadri
Retro aldol (2nd rxn of Scheme 3): D-fructose → Dihydroxyacetone + Glyceraldehyde	3.87×10^{12}	35.6	331	Seshadri

a. Reaction parameters are from Zhou et al.[1] or Seshadri and Westmoreland,[2] and calculated only for unimolecular fragmentation at the temperature of 500 °C.
b. Pre-exponential *A* factor has the unit of s^{-1} for the unimolecular reaction and s^{-1} atm^{-1} for the bimolecular reaction. The only binary reaction here is water-assisted isomerization.
c. Bimolecular reaction rate for water-assisted isomerization cannot be calculated without the information on partial water pressure. Upper limit of pseudo first-order reaction rate was calculated for the local water pressure of 1 atm.

References

1. Zhou, X. W.; Nolte, M. W.; Mayes, H. B.; Shanks, B. H.; Broadbelt, L. J., Experimental and Mechanistic Modeling of Fast Pyrolysis of Neat Glucose-Based Carbohydrates. 1. Experiments and Development of a Detailed Mechanistic Model. *Ind. Eng. Chem. Res.* **2014,** *53* (34), 13274-13289.

2. Seshadri, V.; Westmoreland, P. R., Concerted Reactions and Mechanism of Glucose Pyrolysis and Implications for Cellulose Kinetics. *J. Phys. Chem. A* **2012,** *116* (49), 11997-12013.

CHAPTER 5

REAL-TIME MONITORING OF SINGLE PARTICLE PYROLYSIS FOR HERBACEOUS AND WOODY NATIVE BIOMASS WITH TIME-OF-FLIGHT MASS SPECTROMETRY

A manuscript to be submitted to *Journal of Analytical and Applied Pyrolysis*

Carolyn P. Hutchinson, Evan A. Larson, and Young Jin Lee

Abstract

Bio-oils from fast pyrolysis conversion of lignocellulosic biomass are a promising source of drop-in fuels and commodity chemicals. However, a significant bottleneck toward optimization of this renewable energy platform is the lack of fundamental, molecular-level understanding validated by experiments. The complexity of lignocellulosic biomass and a lack of appropriate instrumentation to perform the necessary measurements have prevented significant forward progress despite decades of research. Lignocellulosic biomass is composed of three main biopolymers (cellulose, hemicellulose, and lignin); the amount and composition of each vary depending on the type of biomass. In this work, single particles (< 20 µg) of herbaceous, hardwood, and softwood biomass are pyrolyzed and the pyrolyzates are analyzed in real-time without separation using a novel dopant-assisted atmospheric pressure chemical ionization source coupled to a time-of-flight mass spectrometry system. We are able to observe differences in total pyrolysis time as well as differences in the temporal profiles of pyrolyzates produced from the decomposition of each biopolymer. Observed differences are explained based on the lignin, cellulose, and hemicellulose content and composition.

Introduction

Thermochemical conversion of lignocellulosic biomass is promising as a supplement or replacement for petroleum fuels and products. Fast pyrolysis produces high yields (up to 60%) of condensables, called bio-oils, which can be upgraded to drop-in transportation fuels and commodity chemicals.[1-2] However, bio-oil suffers from several problems (e.g., high oxygen content, highly acidic, highly corrosive, high water content, poor long-term stability) which petroleum oil does not, and forward progress towards solving these issues has been stalled due to a lack of experimentally validated fundamental understanding.[2]

Lignocellulosic biomass is composed of three main biopolymers: cellulose, hemicellulose, and lignin. Additionally, there are pectins, proteins, and minerals present, though these are typically found in amounts small enough to be negligible.[3]. Hemicellulose and cellulose together create cross-linked fibrils, and hemicellulose is then usually covalently bound to lignin.[4] These three biopolymers determine many properties of plants, such as the flexibility of herbaceous biomass due to its low cellulose content compared to hemicellulose.

Cellulose is the simplest and most abundant biopolymer, made of linear chains of D-glucose units connected by β-1,4-linkages.[6-7] It has a well-defined structure, unlike hemicellulose and lignin. The bulk of molecular-level research has focused on cellulose. Historically, kinetic regimes have been described as lump-sum models with the Broido-Shafizadeh model being the most representative.[6] Several breakthroughs in the early 2010's resulted in the development of a mechanistic model based on glucose pyrolysis.[7-9] Our group has successfully applied novel instrumentation to the analysis of thin-film

pyrolysis of carbohydrates and isotopically labeled glucose to further develop these regimes. Hemicellulose and lignin have both undergone far less study than cellulose, however.

Hemicellulose is a branched heteropolymer with a diverse structure composed of several types of saccharides including pentoses and hexoses. Its composition varies between feedstocks and includes nearly all the D-pentose sugars found in plant matter. In different biomasses, hemicellulose varies greatly in terms of physical and physiochemical properties and structure due to the different monomers present, type of bonding with lignin, degrees of acetylation, and degrees of branching.[3,5] Xylans (predominant in hardwood and herbaceous hemicellulose)[5] can form ester-linkages with lignin while arabinoxylans (the major hemicellulose polysaccharide in herbaceous biomass)[3,5] covalently cross-link with lignin through ferulic acid groups.[3] Xyloglucans in softwood biomass hydrogen bond more strongly with cellulose then other common hemicelluloses subunits.

Hemicellulose research has been limited due to its complexity as well as a number of other reasons. Isolating hemicellulose without altering the chemical structure is not possible currently as the severity of isolation treatments greatly affects the structure and composition of the isolated hemicellulose (e.g., stripping off acetyl functionalities).[5] Most research has focused on commercially available hemicellulose and polysaccharide surrogates which do not satisfactorily represent the complexity of native hemicellulose. Theoretical studies have been conducted,[10-11] as have studies using surrogates and isolates despite their shortcomings.[12-16]

Lignin is a complex, unstructured phenol-based heteropolymer composed of three monolignol monomers whose structures are shown in Figure 1: *p*-coumaryl alcohol (H), coniferyl alcohol (G), and sinapyl alcohol (S). The amount and type of these monolignol monomers depends on the feedstock.[17] Herbaceous lignin contains H, S, and G; hardwood lignin contains S and G; softwood lignin contains G with a small amount of H.[17] Research on isolated lignin has been slightly more productive than hemicellulose research, though is currently limited mostly to theoretical studies, surrogates, and attempts to classify the lignome. Patwardhan et al. were able to gain some insights into the fast pyrolysis of corn stover lignin using micropyrolysis-GC-MS/FID, though they were unable to detect oligomers with these methods and did not suggest any molecular mechanisms.[18] Wang et al. looked at lignin polymers isolated with four different methods from pine wood, with similar limitations.[19] A number of studies using surrogate model compounds have attempted to satisfactorily provide a basis for molecular-level lignin behavior modeling.[20-22] A unique comparison of softwood, hardwood, and herbaceous lignin by Zhou et al. did provide insight into the impact of the monolignol monomer composition on the pyrolysis behavior of lignin isolates.[23] Little work has been conducted to attempt to study whole biomass in its native state.[2, 4-5, 7, 24-27]

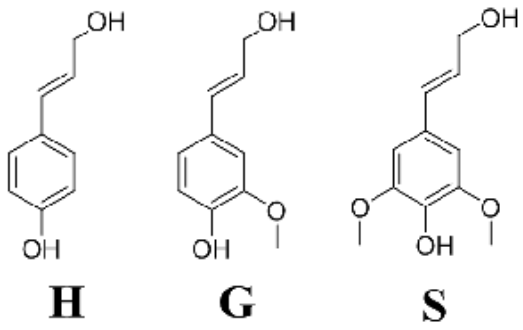

Figure 1. Monolignol monomers: *p*-coumaryl alcohol (H), coniferyl alcohol (G), sinapyl alcohol (S).

We have recently developed a novel analytical platform to address the issues facing the analysis of native biomass pyrolysis behavior. This is accomplished using real-time analysis with a high heating rate without necessitating GC separation. A drop-in microfurnance pyrolyzer is directly connected to a high resolution, high sensitivity, fast scanning time-of-flight mass spectrometer (TOF MS) through dopant-assisted atmospheric pressure chemical ionization (dAPCI). A GC oven is used to prevent condensation but no chromatographic column is used. This allows us to monitor each molecular product with subsecond temporal resolution for a small sample size.

Using this system, we investigate the molecular-level pyrolysis behavior of single particles of herbaceous, hardwood, and softwood whole biomass. By monitoring single particles of whole biomass, temporal profiles for pyrolyzates from cellulose, hemicellulose, and lignin can be derived. Relationships between lignin, cellulose, and hemicellulose content and the pyrolysis behavior can be elucidated from these temporal profiles. This provides unique insight into the fast pyrolysis behavior of different biomass types.

Experimental Section

Materials & Sample Introduction

$^{13}C_6$-levoglucosan (1,6-anhydro-β-glucopyranose) (>99% ^{13}C atom) was obtained from Omicron Biochemicals (South Bend, IN). Representative hardwood (red oak), softwood (loblolly), and herbaceous (corn stover) biomass were provided by the Brown group at the Bioeconomy Institute at Iowa State University. All wood samples were

debarked. The wood samples were ground and sieved; the corn stover was ball milled. The samples were pyrolyzed with no further processing.

Samples were introduced using deactivated stainless steel cups. A thin-film of 0.05 μg ^{13}C-levoglucosan was placed on the outside upper rim of the sample cup to serve as an internal standard for time correction and as an internal standard. This film was dried under a light vacuum for ~1 min. Particles of biomass were sorted for similar shape, color, and size. A single particle was selected and placed inside the sample cup using a short length of pulled fused silica capillary.

To ensure accurate time correction, two cups were dropped in sequence using an auto shot sampler (AS-1020E, Frontier, Fukushima, Japan) with a 0.1 min run time. The first cup only has the ^{13}C-levoglucosan film and the second cup has the biomass particle in addition to the ^{13}C-levoglucosan film. This provides a reproducible 135 second time between the two cups. In addition to the 6 s of run time, the extra 129 s is due to dead times for communication between the various components, ejecting the used sample cup, purging the holding chamber on the auto shot sampler, and other preparation time for the auto shot sampler and GC. Extracting the *m/z* 186 ($[^{13}C_6H_{10}O_5+NH_4]^+$) ion trace allows for correction of time-zero on the biomass cup (the second cup) since levoglucosan evaporates rather than pyrolyzes, providing an accurate time-zero to calibrate t_{drop}, t_{escape}, and t_{dead}, leaving only $t_{pyrolysis}$ and $t_{heating}$ left to take into account.

Mass Spectrometry Analysis

These cups were introduced to the μPy-dAPCI-TOF MS system via the auto shot sampler and a drop-in micropyrolyzer (3030S, Frontier) mounted on the inlet of a gas

chromatograph (7890A, Agilent, Palo Alto, CA). A deactivated fused silica transfer line (0.61 m, 100 μm inner diameter) is used to directly connect the GC injection port to a GC-APCI interface (Agilent 3212) a time-of-flight mass spectrometer (TOF MS) (Agilent 6224). The inlet, interface, and oven temperature are all set to 280 °C, and the inlet split is set at 100:1 (100 mL/min through the micropyrolyzer, 1 mL/min through the transfer line). Pre-heated ammonia (500 ppm in helium, 1 mL/min) is added as a dopant gas to the create a dopant-assisted APCI source (dAPCI). Ammonia is introduced as a sheath gas around the capillary so that it is heated to the same temperature as the column effluent. The ionization source is humidity controlled year-round with a simple, robust system built in-house utilizing dry and humidified nitrogen.

Results and Discussion

A novel analytical system developed by our group for studying biomass pyrolysis in real-time was used for the current study. The schematic diagram is shown in Figure S1 and described in detail elsewhere.[25] Briefly, biomass materials are pyrolyzed using a drop-in microfurnance which allows for extremely fast heating rates. The analytes travel through a short (0.6 m) deactivated fused silica transfer line in an oven held below the pyrolysis temperature of the majority of carbohydrates but warm enough to prevent condensation. This allows the compounds to elute without any separation with a residence time of less than 2 s.[25] The pyrolyzates are ionized with dopant-assisted atmospheric pressure chemical ionization (dAPCI) and introduced into a time-of-flight mass spectrometer (TOF MS). dAPCI is a soft ionization which, when ammonia gas is introduced as a dopant, which prevents fragmentation and allows for sub-second, pseudo

real-time monitoring using high mass resolution and fast scanning TOF MS. $^{13}C_6$-levoglucosan (0.05 μg) is applied as a thin-film on the outside upper edge of the sample cup to provide a pyrolysis time calibrant. The time profile of each pyrolyzate could be monitored by tracing each ion signal using a narrow mass window (0.1 u). When the critical size dimension (i.e., the one heat must transfer through for pyrolysis to occur) is small enough (< 70 μm)[9, 33], the time in the melt phase is nominal as the particle pyrolyzes nearly immediately from solid to gaseous products, minimizing melt phase reactions. Secondary vapor phase reactions cannot be avoided but they are minimized in our system by the short residence time (~0.2 s) and the temperature difference between the furnace and the dead zone of the transfer line.

Biomass particles were selected to have similar shape, dimensions, and color, as biomass is typically very heterogeneous on the particle level. The corn stover used was ball-milled and thus more homogeneous; a small amount (<20 μg) was placed into the $^{13}C_6$-levoglucosan labeled sample cup using a short piece of pulled fused silica capillary. The red oak and loblolly pine were both ground and sieved for a particle size less than 200 μm. Single particles with mass < 30 μg were placed in the bottom of $^{13}C_6$-levoglucosan labeled sample cups using pulled fused silica capillary. The sensitivity of dAPCI-TOF MS allows for the analysis of such small amounts, approximately 1/10 to 1/20 the typical load amount used for μPy-GC-FID or μPy-GC-MS studies with traditional electron ionization mass spectrometry.

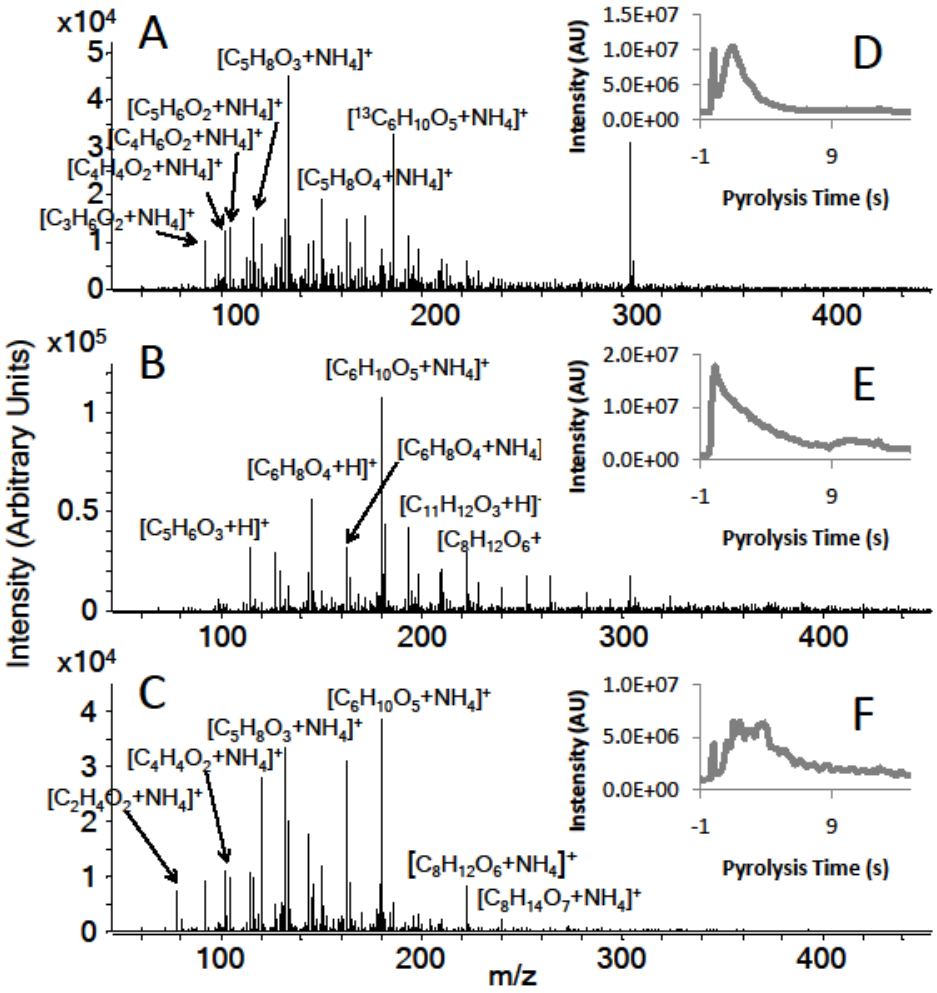

Figure 2. Averaged mass spectra (A-C) and total ion chromatograms (D-F) from pyrolysis of corn stover (A, D), red oak (B, E), and loblolly pine (C, F).

A representative mass spectrum for the pyrolysis of each biomass and the corresponding total ion chromatogram (TIC) is shown in Figure 2. The mass spectra are averaged from -0.2 s to twice the full width at half maximum (FWHM) of the pyrolyzate total ion chromatogram in order to capture a representative mass spectrum. The $FWHM_{TIC}$ are measured to be 1.75 s (corn stover), 2.5 s (red oak), and 4 s (loblolly pine). The increase in pyrolysis time may be due in part to increased lignin content in each since

corn stover contains the least lignin (12 wt%) while loblolly pine contains the most (16%) and the decreased availability of holocellulose for pyrolysis the lignin content causes. The mass spectrum of corn stover (Figure 2A) shows significant contributions from *m/z* 116.071, 134.081, and 150.076, corresponding to $[C_5H_6O_2+NH_4]^+$, $[C_5H_8O_3+NH_4]^+$, and $[C_5H_8O_4+NH_4]^+$ respectively. These small C5 compounds are produced from the pyrolysis of hemicelluloses; it is known that furans are more readily produced from sugars which enter pyrolysis as furans. The red oak mass spectrum (Figure 2B) is dominated by *m/z* 180.086, corresponding to $[C_6H_{10}O_5+NH_4]^+$ (levoglucosan), as well as *m/z* 99.045 ($[C_5H_6O_2+H]^+$), 115.039 ($[C_5H_6O_3+H]^+$), 145.050 ($[C_6H_8O_4+H]^+$), 222.098 ($[C_8H_{12}O_6+NH_4]^+$), and 252.109 ($[C_9H_{14}O_7+NH_4]^+$). These compounds are products of holocellulose pyrolysis; levoglucosan is produced from the pyrolysis of cellulose, the C5 compounds from the pyrolysis of hemicelluloses, and the larger compounds are saccharide oligomers. The mass spectrum of loblolly pine has major ions at *m/z* 102.056 ($[C_4H_4O_2+NH_4]^+$), 132.066 ($[C_5H_6O_3+NH_4]^+$), 162.076 ($[C_6H_8O_4+NH_4]^+$), 180.086 ($[C_6H_{10}O_5+NH_4]^+$), and 222.098 ($[C_8H_{12}O_6+NH_4]^+$). With the exception of $[C_6H_8O_4+H]^+$ which has been observed in the pyrolysis of isolated lignin, all the dominant ion contributions in any biomass are from holocellulose pyrolysis. Herbaceous biomass typically has a high hemicellulose content compared to its cellulose content, and hemicellulose preferentially forms C5 highly oxygenated compounds due to its largely xylan composition rather than the C6 sugaric compounds formed from the glucose-based cellulose. The higher abundance of oligomers in hardwood biomass is likely due to the significantly higher cellulose content (41 wt% compared to 29 wt% for herbaceous and 32 wt% for softwood). TGA has shown that cellulose takes the longest time of the three

main lignocellulose biopolymers to begin pyrolysis, resulting in more metastable intermediates observed in our instrumentation. Two metastable intermediates are observed in significant abundance from both woody feedstocks: $C_8H_{12}O_6$ and $C_9H_{14}O_7$. A table of all the major compounds with formulas is presented in the Supplementary Information (Table S1).

Compounds from the pyrolysis of holocellulose and previously identified in cellulose thin-film pyrolysis by our group were evaluated for differences in behavior. Their time profiles are evaluated using EICs over a narrow mass window of 0.1 u (Figure 3). These time profiles allow for further investigation into the behavior of these pyrolyzates. Specific *m/z* values can be monitored in extremely short time windows (0.05 s) due to the fast scanning speed of the TOF MS. Most compounds begin eluting after time-zero; however, each biomass has several compounds which have a small, narrow peak at around -0.1 s in addition to the later intense, broad peaks. This behavior is seen in $C_6H_{10}O_5$ and $C_6H_8O_4$ for corn stover, $C_6H_8O_4$ and $C_6H_6O_3$ for red oak, and $C_6H_{10}O_5$, $C_6H_8O_4$, $C_4H_6O_3$, and $C_3H_6O_3$ for loblolly pine. This early peak is likely caused by surface pyrolysis of exposed hemicellulose, which readily decomposes and is available on the surface of the biopolymer fibrils. Most pyrolyzates for corn stover begin to appear after 0.5 s and reach maxima around 1.25 to 1.5 s (Figure 3A). $C_4H_6O_3$ is an interesting exception, however; it begins to appear at 0.2s and reaches a maximum at 0.75 s. This behavior suggests that in herbaceous biomass it is preferentially produced from another source such as hemicellulose even though this compound has previously been observed in cellulose pyrolysis. Red oak holocellulose pyrolyzate time profiles are dominated by levoglucosan (Figure 3B). Levoglucosan and dianhydroglucopyranose display a bimodal

distribution with a first peak with FWHM of 4 s and maxima at 1.65 s with a second smaller peak at 10.37 s; hydroxymethyl furfural has a similar bimodal distribution except the first peak is narrower (FWHM 3.25 s) and the maximum occurs at 0.95 s. Loblolly pine has a similar behavior without the bimodal distribution for levoglucosan, dianhydroglucopyranose, hydroxymethyl furfural, and $C_4H_6O_3$ (Figure 3C). The similar behavior of these compounds in all three biomass types suggests that the type and composition of biomass has less effect on the products formed by cellulose pyrolysis but does determine how these pyrolyzates are able to escape the particle. Loblolly pine in particular, but red oak as well, show fluctuations indicative of aerosol ejection while the profile of corn stover pyrolysis is more similar to earlier thin-film experiments. To ensure that the difference in preparation between the ball-milled corn stover and the ground wood was not causing this, ground and sieved corn stover was pyrolyzed and the pyrolyzate behavior was extremely similar to the ball-milled corn stover. This means that the differences observed are caused by the structure and type of biomass rather than the preparation. Corn stover has a lower lignin content and much higher hemicellulose-to-cellulose ratio than red oak or loblolly pine, suggesting that low lignin and high hemicellulose content provide accessible cellulose for pyrolysis.

The time profiles of major compounds from lignin pyrolysis were compared in Figure 4. Since the lignin of each biomass varies based on the monolignol monomer composition, the phenolic profiles are expected to differ drastically. The phenolic compounds when corn stover is pyrolyzed, but the time profiles all have similar

characteristics as seen in Figure 4A. With the exception of one compound studied which begins to appear to 0.25 s, phenolic products begin to appear at 0.5 s. All low intensity compounds have a FWHM of 2.5 s and the high intensity compounds have a FWHM of 1 s. The phenolic compounds produced from red oak pyrolysis (Figure 4B) and loblolly pine (Figure 4C) are radically different from each other and from corn stover. The phenolic pyrolyzates from red oak begin to appear at -0.2 s and reach a maximum at -0.05 s with the exception of the most abundant pyrolyzate which reaches a maximum at 0.05 s. Loblolly pine phenolic pyrolyzates resemble the distribution of the cellulose sugaric pyrolyzates with a bimodal distribution consisting of a sharp peak at -0.1 s and a broad, fluctuating second peak between 0.6 s and 5.8 s. The varying behavior could be due to interactions between cellulose and lignin in the different feedstocks. Cellulose and lignin are present together in plant cell walls and together provide structural stability for the plant. Loblolly pine has the largest ratio of lignin-to-cellulose on a weight percent basis (0.5) while red oak has the lowest (0.31). Hardwoods also have less polar lignin than softwoods, meaning that it is less likely to form stable bonds with cellulose which must be broken before pyrolysis can proceed.

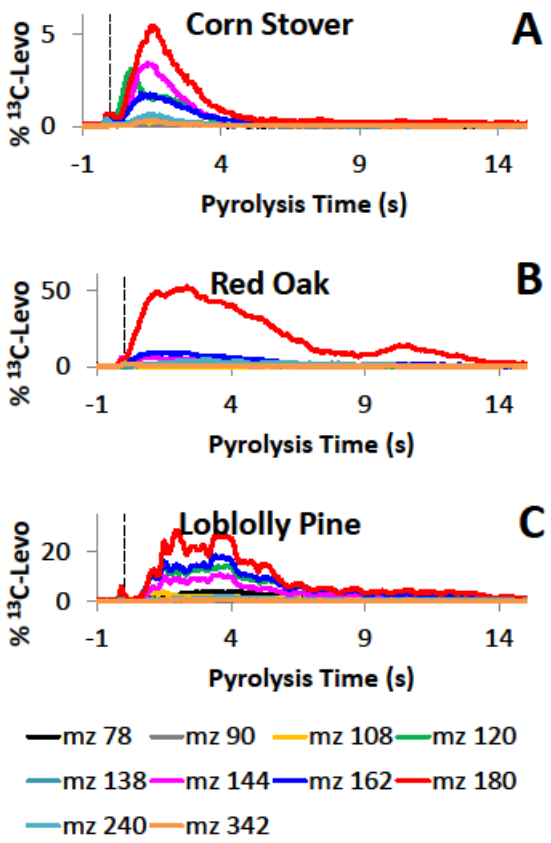

Figure 3. Time profiles for select compounds from pyrolysis of holocellulose in corn stover (A), red oak (B), and loblolly pine (C).

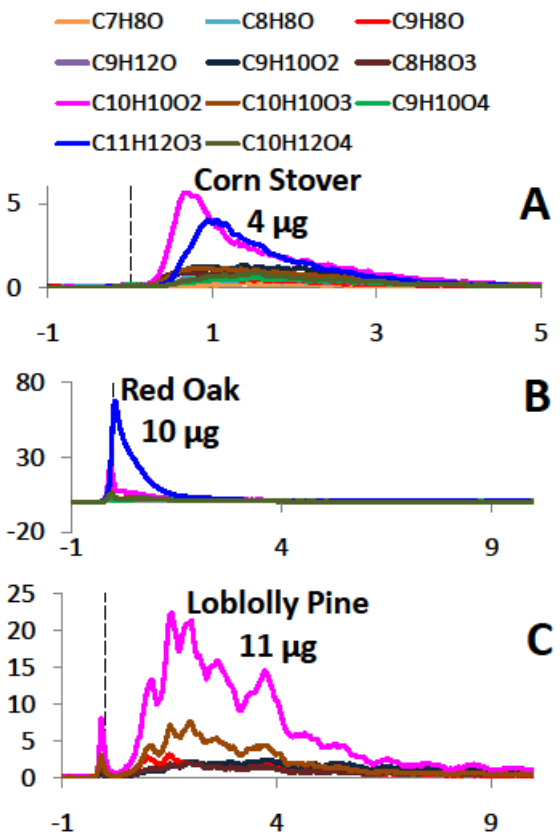

Figure 4. Time profiles for select phenolic compounds from pyrolysis of corn stover (A), red oak (B), and loblolly pine (C).

The most abundant compounds in the pyrolysis of each biomass are especially interesting. Occurring at *m/z* 193.086 and *m/z* 163.076, these ions are assigned as $[C_{11}H_{12}O_3+H]^+$ and $[C_{10}H_{10}O_2+H]^+$. The mass difference of 30.01 can be confidently assigned as CH2O corresponding to a methoxy loss. Since the monolignol monomers vary only by their methoxy functionalities, it is likely that these phenolic pyrolyzates are derived from the monolignol monomers. This hypothesis is supported by the fact that $[C_9H_8O+H]^+$ (*m/z* 133.065) is also present in corn stover and loblolly pine. However, the double bond equivalence value for these compounds is equal to 6, meaning that the central motif is more substituted than a phenol ring. Based on MS/MS data, the structures

are identified as a series of methoxy additions to 3H-inden-5-ol (Figure S2). Corn stover pyrolysis produces *m/z* 133.065, 163.076, and 193.086 corresponding to derivatives of H-, G-, and S-type lignin subunits respectively. Red oak pyrolysis produces *m/z* 163.076 and 193.086 from G- and S-type lignin subunits. Loblolly pine produces *m/z* 133.065 and 163.076 from H- and G-type lignin subunits.

The time profiles for the lignin-derived pyrolyzates of each biomass are also extremely different, suggesting differences in the accessibility of the lignin for pyrolysis. Corn stover lignin pyrolyzates appear after about 0.5 s and pyrolysis is complete shortly after (Figure 4A). Herbaceous lignin has strong ferulic acid cross-links with hemicelluloses, which has some hydrogen-bonding with cellulose. Red oak lignin pyrolyzates evolve immediately and complete in a short time (Figure 4B); hardwood is more nonpolar than softwood and is less strongly bound to hemicelluloses than herbaceous lignin. Thus, hardwood lignin is able to pyrolyze quickly. Loblolly pine lignin pyrolyzates exhibit an initial sharp peak near 0s then a second distribution with a large amount of irregular fluctuations throughout. The fluctuations have previously been attributed to aerosol ejections that occur when biomass spends adequate time in the molten phase. Softwood lignin is also more polar than hardwood lignin and thus can form non-covalent bonds with itself. Additionally, softwood hemicellulose, though not strongly covalently bound to lignin, is composed of hexoses unlike herbaceous or hardwood hemicelluloses; this allows softwood hemicellulose to form strong hydrogen bonds with cellulose.

Conclusions

In this work, we were successfully able to analyze and compare three different very small, representative samples of the major types of biomass (herbaceous, hardwood, softwood) in their native state in real-time using μPy-dAPCI-TOF MS, a novel analytical platform developed by our group. The sensitivity of this platform allows for the analysis of single particles (< 20 μg), one order of magnitude smaller than the amount needed for typical GC-MS analysis. The high mass resolution of the TOF MS does not necessitate GC separation and thus allows for real-time analysis. Differences in total pyrolysis time were observed; tentatively, increased pyrolysis time is correlated with increased lignin content as herbaceous biomass (corn stover) contains the least lignin and completes pyrolysis most quickly while softwood (loblolly pine) contains the most lignin and requires the longest time for pyrolysis to complete. Both woody biomass spectra see significant contributions from C6 and larger compounds from holocellulose pyrolysis. This is due to the high cellulose content in both woody biomasses. The herbaceous biomass spectrum is dominated by C5 and smaller compounds from hemicellulose. Metastable intermediates (e.g., $C_8H_{12}O_6$, $C_8H_{14}O_7$) can be observed with this method.

By extracting ion chromatograms over a small mass window (0.1 u) and correcting for time-zero, temporal profiles for pyrolyzates from the decomposition of holocellulose and lignin can be constructed. The differences in temporal profiles are likely due to differences in structure and in composition between the types of biomass. For example, hardwood lignin is more nonpolar than softwood lignin and the phenolic temporal profiles for red oak is narrow, beginning slightly before 0 s, while the phenolic temporal profiles for loblolly pine are much broader. A series of compounds with a 3H-

inden-5-ol central motif and methoxy additions derived from the monolignol monomers was discovered. SEM imaging of the biomass particles could help verify the impact of structure. TGA analysis of the biomass samples will help elucidate the impact of biopolymers on pyrolysis behavior. Detailed information on the prevalence of these cross-linkages is not widely available but would provide a better understanding of the molecular-level structure of native biomass. By expanding the study to include more biomass, more general conclusions about the pyrolysis behavior of different types of biomass will be able to be made.

Acknowledgments

This work is supported by National Science Foundation, Division of Chemical, Bioengineering, Environmental and Transport Systems, Energy for Sustainability Program. The authors thank Tannon Daugaard and Jake Lindstrom for the biomass samples and helpful discussions.

References

1. Dauenhauer, P. J.; Huber, G. W., Biomass at the shale gas crossroads. *Green Chem* **2014,** *16* (2), 382-383.

2. Mohan, D.; Pittman, C. U.; Steele, P. H., Pyrolysis of wood/biomass for bio-oil: A critical review. *Energ Fuel* **2006,** *20* (3), 848-889.

3. Vassilev, S. V.; Baxter, D.; Andersen, L. K.; Vassileva, C. G., An overview of the chemical composition of biomass. *Fuel* **2010,** *89* (5), 913-933.

4. Zhang, J.; Choi, Y. S.; Yoo, C. G.; Kim, T. H.; Brown, R. C.; Shanks, B. H., Cellulose-Hemicellulose and Cellulose-Lignin Interactions during Fast Pyrolysis. *Acs Sustain Chem Eng* **2015,** *3* (2), 293-301.

5. Zhou, X. W.; Li, W. J.; Mabon, R.; Broadbelt, L. J., A Critical Review on Hemicellulose Pyrolysis. *Energy Technol-Ger* **2017,** *5* (1), 52-79.

6. Burnham, A. K.; Zhou, X. W.; Broadbelt, L. J., Critical Review of the Global Chemical Kinetics of Cellulose Thermal Decomposition. *Energ Fuel* **2015,** *29* (5), 2906-2918.

7. Di Blasi, C., Modeling chemical and physical processes of wood and biomass pyrolysis. *Prog Energ Combust* **2008,** *34* (1), 47-90.

8. Kawamoto, H., Review of Reactions and Molecular Mechanisms in Cellulose Pyrolysis. *Curr Org Chem* **2016,** *20* (23), 2444-2457.

9. Paulsen, A. D.; Mettler, M. S.; Dauenhauer, P. J., The Role of Sample Dimension and Temperature in Cellulose Pyrolysis. *Energ Fuel* **2013,** *27* (4), 2126-2134.

10. Huang, J. B.; Liu, C.; Tong, H.; Li, W. M.; Wu, D., Theoretical studies on pyrolysis mechanism of xylopyranose. *Comput Theor Chem* **2012,** *1001*, 44-50.

11. Zhang, Z.; Liu, C.; Li, H. J.; Huang, J. B.; Huang, X. L., Theoretical Studies of Pyrolysis Mechanism of Xylan Monomer. *Acta Chim Sinica* **2011,** *69* (18), 2099-2107.

12. Patwardhan, P. R.; Brown, R. C.; Shanks, B. H., Product Distribution from the Fast Pyrolysis of Hemicellulose. *Chemsuschem* **2011,** *4* (5), 636-643.

13. Vinueza, N. R.; Kim, E. S.; Gallardo, V. A.; Mosier, N. S.; Abu-Omar, M. M.; Carpita, N. C.; Kenttamaa, H. I., Tandem mass spectrometric characterization of the conversion of xylose to furfural. *Biomass Bioenerg* **2015,** *74*, 1-5.

14. Wang, S. R.; Ru, B.; Dai, G. X.; Sun, W. X.; Qiu, K. Z.; Zhou, J. S., Pyrolysis mechanism study of minimally damaged hemicellulose polymers isolated from agricultural waste straw samples. *Bioresource Technol* **2015,** *190*, 211-218.

15. Wang, S. R.; Ru, B.; Lin, H. Z.; Luo, Z. Y., Degradation mechanism of monosaccharides and xylan under pyrolytic conditions with theoretic modeling on the energy profiles. *Bioresource Technol* **2013,** *143*, 378-383.

16. Wang, S. R.; Ru, B.; Lin, H. Z.; Sun, W. X., Pyrolysis behaviors of four O-acetyl-preserved hemicelluloses isolated from hardwoods and softwoods. *Fuel* **2015,** *150*, 243-251.

17. Kawamoto, H., Lignin pyrolysis reactions. *J Wood Sci* **2017,** *63* (2), 117-132.

18. Patwardhan, P. R.; Brown, R. C.; Shanks, B. H., Understanding the Fast Pyrolysis of Lignin. *Chemsuschem* **2011,** *4* (11), 1629-1636.

19. Wang, S. R.; Ru, B.; Lin, H. Z.; Sun, W. X.; Luo, Z. Y., Pyrolysis behaviors of four lignin polymers isolated from the same pine wood. *Bioresource Technol* **2015,** *182*, 120-127.

20. Amundson, L. M.; Gallardo, V. A.; Vinueza, N. R.; Owen, B. C.; Reece, J. N.; Habicht, S. C.; Fu, M. K.; Shea, R. C.; Mossman, A. B.; Kenttamaa, H. I., Identification and Counting of Oxygen Functionalities and Alkyl Groups of Aromatic Analytes in Mixtures by Positive-Mode Atmospheric Pressure Chemical Ionization Tandem Mass Spectrometry Coupled with High-Performance Liquid Chromatography. *Energ Fuel* **2012,** *26* (5), 2975-2989.

21. Haupert, L. J.; Owen, B. C.; Marcum, C. L.; Jarrell, T. M.; Pulliam, C. J.; Amundson, L. M.; Narra, P.; Aqueel, M. S.; Parsell, T. H.; Abu-Omar, M. M.; Kenttamaa, H. I., Characterization of model compounds of processed lignin and the lignome by using atmospheric pressure ionization tandem mass spectrometry. *Fuel* **2012,** *95* (1), 634-641.

22. Owen, B. C.; Haupert, L. J.; Jarrell, T. M.; Marcum, C. L.; Parsell, T. H.; Abu-Omar, M. M.; Bozell, J. J.; Black, S. K.; Kenttamaa, H. I., High-Performance Liquid Chromatography/High-Resolution Multiple Stage Tandem Mass Spectrometry Using Negative-Ion-Mode Hydroxide-Doped Electrospray Ionization for the Characterization of Lignin Degradation Products. *Anal Chem* **2012,** *84* (14), 6000-6007.

23. Zhou, S.; Xue, Y.; Sharma, A.; Bai, X. L., Lignin Valorization through Thermochemical Conversion: Comparison of Hardwood, Softwood and Herbaceous Lignin. *Acs Sustain Chem Eng* **2016,** *4* (12), 6608-6617.

24. Fan, Y. S.; Cai, Y. X.; Li, X. H.; Jiao, L. H.; Xia, J. S.; Deng, X. L., Effects of the cellulose, xylan and lignin constituents on biomass pyrolysis characteristics and bio-oil composition using the Simplex Lattice Mixture Design method. *Energ Convers Manage* **2017,** *138*, 106-118.

25. Horton, S. R.; Mohr, R. J.; Zhang, Y.; Petrocelli, F. P.; Klein, M. T., Molecular-Level Kinetic Modeling of Biomass Gasification. *Energ Fuel* **2016,** *30* (3), 1647-1661.

26. Teixeira, A. R.; Gantt, R.; Joseph, K. E.; Maduskar, S.; Paulsen, A. D.; Krumm, C.; Zhu, C.; Dauenhauer, P. J., Spontaneous Aerosol Ejection: Origin of Inorganic Particles in Biomass Pyrolysis. *Chemsuschem* **2016,** *9* (11), 1322-1328.

27. Paulsen, A. D.; Hough, B. R.; Williams, C. L.; Teixeira, A. R.; Schwartz, D. T.; Pfaendtner, J.; Dauenhauer, P. J., Fast Pyrolysis of Wood for Biofuels: Spatiotemporally Resolved Diffuse Reflectance In situ Spectroscopy of Particles. *Chemsuschem* **2014,** *7* (3), 765-776.

28. Mettler, M. S.; Mushrif, S. H.; Paulsen, A. D.; Javadekar, A. D.; Vlachos, D. G.; Dauenhauer, P. J., Revealing pyrolysis chemistry for biofuels production: Conversion of cellulose to furans and small oxygenates. *Energ Environ Sci* **2012,** *5* (1), 5414-5424.

29. Bahng, M. K.; Mukarakate, C.; Robichaud, D. J.; Nimlos, M. R., Current technologies for analysis of biomass thermochemical processing: A review. *Anal Chim Acta* **2009,** *651* (2), 117-138.

30. Huber, G. W.; Iborra, S.; Corma, A., Synthesis of transportation fuels from biomass: Chemistry, catalysts, and engineering. *Chem Rev* **2006,** *106* (9), 4044-4098.

31. Mettler, M. S.; Vlachos, D. G.; Dauenhauer, P. J., Top ten fundamental challenges of biomass pyrolysis for biofuels. *Energ Environ Sci* **2012,** *5* (7), 7797-7809.

32. Patwardhan, P. R.; Dalluge, D. L.; Shanks, B. H.; Brown, R. C., Distinguishing primary and secondary reactions of cellulose pyrolysis. *Bioresource Technol* **2011,** *102* (8), 5265-5269.

33. Krumm, C.; Pfaendtner, J.; Dauenhauer, P. J., Millisecond Pulsed Films Unify the Mechanisms of Cellulose Fragmentation. *Chem Mater* **2016,** *28* (9), 3108-3114.

Supplemental Information

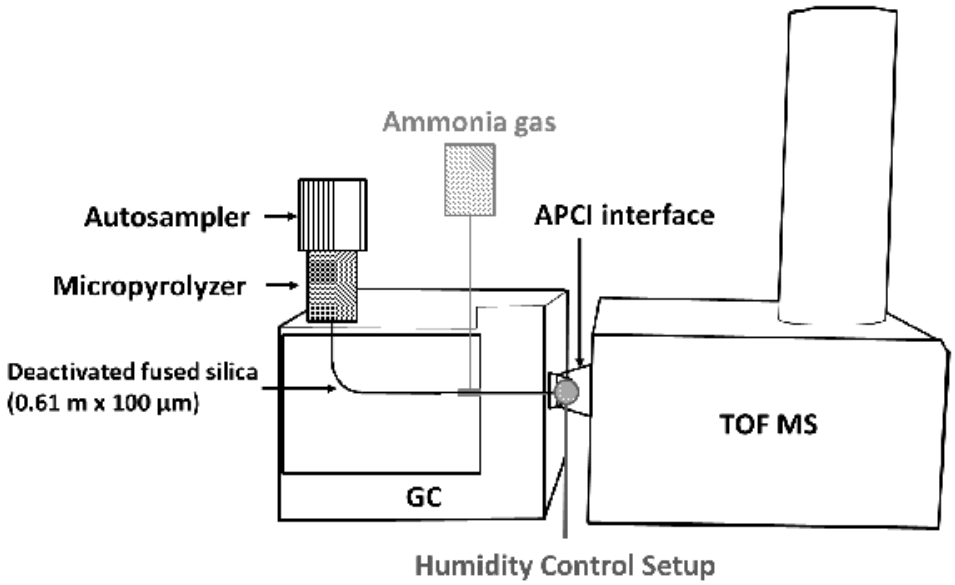

Figure S1. µPy-dAPCI-TOF MS schematic diagram

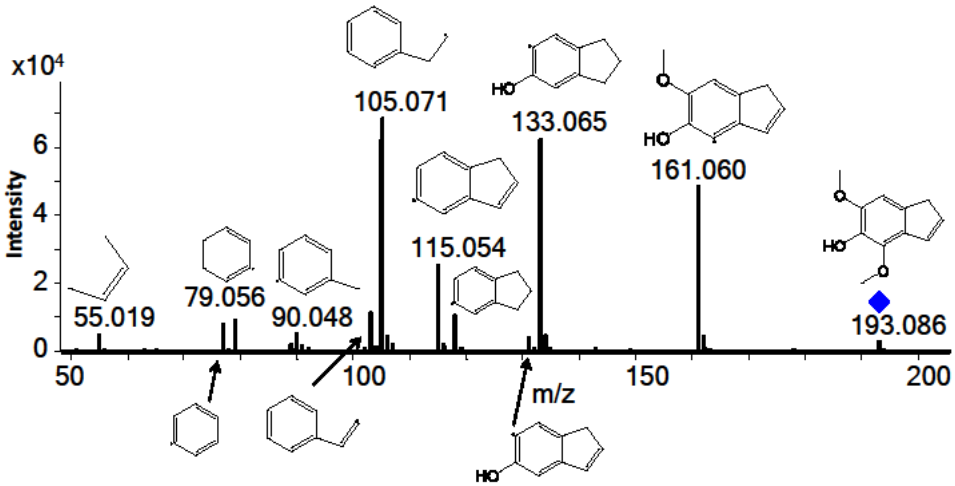

Figure S2. MS/MS of *m/z* 193, corresponding to $[C_{11}H_{12}O_3+H]^+$

Table S1. List of *m/z* values and formulas for compounds in biomass pyrolysis

m/z	Formula	Corn Stover	Red Oak	Loblolly Pine
78.057	C2H4O2			Y
92.071	C3H6O2	Y		Y
99.045	C5H6O2		Y	Y
102.056	C4H4O2	Y		Y
104.071	C4H6O2	Y		Y
108.066	C3H6O3			Y
113.060	C6H8O2	Y		
114.056	C5H4O2	Y		
114.089	C6H8O	Y		
115.039	C5H6O3	Y	Y	Y
116.071	C5H6O2	Y		Y
117.055	C5H8O3	Y	Y	
118.086	C5H8O2	Y		Y
120.066	C4H6O3	Y		Y
127.039	C6H6O3	Y	Y	Y
127.075	C7H10O2	Y		
128.071	C6H6O2	Y		
129.055	C6H8O3		Y	Y
130.051	C5H4O3	Y		Y
130.086	C6H8O2	Y		
132.066	C5H6O3	Y	Y	Y
133.067	C9H8O			Y
134.081	C5H8O3	Y	Y	Y
142.086	C7H8O2	Y		
143.035	C6H6O4		Y	
144.066	C6H6O3	Y	Y	Y
144.099	C7H10O2	Y		
145.050	C6H8O4		Y	Y
146.080	C6H8O3	Y	Y	Y
148.050	C6H10O3	Y		
150.076	C5H8O4	Y	Y	Y
151.076	C9H10O2	Y		Y
152.126	C6H14O3	Y		
153.055	C8H8O3	Y		Y
154.087	C8H8O2	Y		
155.070	C8H10O3	Y	Y	
156.101	C8H10O2	Y		
158.082	C7H8O3	Y		
160.061	C6H6O4			Y
160.097	C7H10O3	Y		
162.076	C6H8O4	Y	Y	Y
163.075	C10H10O2	Y	Y	Y
164.091	C6H10O4	Y	Y	

Table S1 continued

m/z	Formula	Corn Stover	Red Oak	Loblolly Pine
167.071	C9H10O3	Y	Y	
169.086	C9H12O3			Y
170.082	C8H8O3	Y		Y
172.097	C8H10O3	Y	Y	
174.077	C7H8O4		Y	
176.093	C7H10O4	Y		
178.070	C7H8O5		Y	Y
179.071	C10H10O3		Y	Y
180.087	C6H10O5	Y	Y	Y
181.088	C10H12O3	Y	Y	Y
182.102	C6H12O5		Y	
183.066	C9H10O4		Y	
183.102	C10H14O3		Y	
184.097	C9H10O3	Y		Y
186.107	13C6H10O5	INT STD	INT STD	INT STD
192.087	C7H10O5		Y	
193.086	C11H12O3	Y	Y	
194.093	C11H14O3	Y	Y	
195.100	C11H14O3	Y	Y	
196.096	C10H10O3	Y		Y
197.082	C10H12O4		Y	
198.102	C14H14O		Y	
198.111	C10H12O3	Y		Y
208.190	C10H22O3	Y		
209.081	C11H12O4	Y	Y	
210.098	C7H12O6		Y	
211.097	C11H14O4		Y	
212.126	C11H14O3	Y		
222.098	C8H12O6		Y	Y
222.101	C16H14O	Y		
223.098	C12H14O4	Y	Y	
228.123	C11H14O4	Y	Y	
240.110	C8H14O7		Y	
252.109	C9H14O7		Y	
264.109	C10H14O7		Y	
282.122	C18H18O3		Y	
294.126	C19H18O3		Y	
303.123	C17H18O5		Y	
304.248	C16H30O4	Y	Y	
305.251	C20H32O2	Y		
324.136	C23H14O		Y	
390.184	C28H20O		Y	

CHAPTER 6

GENERAL CONCLUSIONS

Summary and Conclusions

The work presented in this dissertation provides a strong foundation for applying atmospheric pressure ionization (API) in combination with high resolution mass spectrometry (HRMS) to build a molecular-level understanding of biomass pyrolysis with detail which cannot be achieved through typical analysis methods. This is achieved through novel ionization techniques and innovative analytical platforms. Combining soft, fragmentation-free ionization with high mass accuracy allows for separation-free chemical identification of the products of fast pyrolysis.

First, an ionization technique was explored to provide less specific ionization of biofuel compounds. Negative mode atmospheric pressure photoionization (APPI) was coupled with high resolution Fourier transform ion cyclotron resonance mass spectrometry (FT-ICR MS) to explore the molecular-level chemical composition of two nitrogen-rich switchgrass biofuels: fast pyrolysis bio-oils and gasification biotar. Negative APPI-FT-ICR MS was able to ionize a wide range of compounds with less specificity than positive APPI, positive electrospray ionization, or negative electrospray ionization.

Next, a series of three chapters explored an important analytical platform. Dopant-assisted atmospheric pressure chemical ionization (dAPCI) prevents the fragmentation which normally necessitates separation in traditional APCI as well as other MS techniques typically coupled with gas chromatography (GC). The role of water in the

ionization mechanisms is also explored. Even in the presence of the ammonia dopant, water plays an extremely important role. Thus, a humidification system was built in-house to provide ample, stable humidity to the source. This system has been in use for over two years now with excellent results. It is applied in the following two chapters.

Next, a micropyrolyzer (μPy) is placed on the back inlet of the GC. A short, deactivated fused silica transfer line to directly deliver pyrolyzates without separation, and selectively ^{13}C-labeled glucose is pyrolyzed in order to monitor the survival of the label on reaction products. Using the temporal profiles achieved from the dAPCI-TOF MS system, previously proposed primary reaction pathways can be supported or invalidated. For example, the proposed pathway for erythrose was supported while the pathway for dihydroxyacetone was invalidated. Dihydroxyacetone was found to be invalid due to limitation of traditional analysis techniques which are not present in the μPy-dAPCI-TOF MS system.

Finally, μPy-dAPCI-TOF MS is applied to single particles of native biomass for a unique comparison of herbaceous, hardwood, and softwood biomass. Differences in the temporal profiles of products from the decomposition of holocellulose and lignin can be observed. Fundamental studies such as this are extremely difficult with traditional analytical platforms due to sample load requirements, limitations in analyte identification, and a lack of real-time analysis. For example, hardwood phenolic products were observed immediately while herbaceous and softwood lignins required about half a second to appear, which may be due to the more nonpolar nature of hardwood lignin.

Future Directions

As this was the first rigorous application of this novel analytical platform, there are nearly limitless places to take it yet. For example, rigorous studies on the effects of thickness in cellulose pyrolysis could be possible due to the small sample load amount possible. Preliminary work has shown promising differences between even small but equal amounts of powder and film for cellulose and lignin. This is an important step in connecting thin-film kinetics to reactor kinetics, since reactors pyrolyze three dimensional particles which are heated in three dimensions, similar to small-scale powder pyrolysis in this system. The best results would be achieved by comparing thin-films, thick-films (films greater than the isothermal-kinetic limit), and powders of different dimensions to extract a full range of kinetics parameters and fully understand the effect that the powder structure has compared to the suspended and dried films.

Another important direction to take this project in is catalysis. Much fast pyrolysis research currently focuses on *in situ* catalysis due to the importance of upgrading bio-oil to achieve a usable transportation fuel or increase yields of value-added chemicals. By replacing the current single shot micropyrolyzer with a tandem micropyrolyzer, this system could easily be modified for analysis of catalysts in complementary ways to the engineers working to solve these problems.

Either direction will result in a huge, important impact in the field of fast pyrolysis. Atmospheric pressure ionization combined with high resolution mass spectrometry holds huge potential for solving the most pressing problems of fast pyrolysis. By answering fundamental, molecular-level questions, we are able to expand the knowledge base in ways that have not been possible for decades.

APPENDIX

TRACKING MOLECULAR PRODUCTS IN FAST PRYOLYSIS OF CARBOHYDRATES WITH SUB-SECOND TEMPORAL RESOLUTION

A manuscript to be submitted to *ACS Sustainable Chemistry & Engineering*

Carolyn P. Hutchinson[#,a], D. Paul Cole[#,b], Erica A. Smith[c], and Young Jin Lee[a,*]

a: Department of Chemistry, Iowa State University, Ames, IA 50011

b: Present address: Baxter Healthcare, Round Lake, IL, 60073, USA.

c: Present address: Phillips66, Bartlesville, OK 74004, USA.

#: Equally contributed to this work.

Abstract

Very little is known about the detailed chemical kinetics of pyrolysis reactions. We developed a new technique that allows for the monitoring of each molecular product from fast pyrolysis with 0.1 second temporal resolution. Molecular products in thin-film pyrolysis of a series of glucose-based carbohydrates were studied which revealed unprecedented details of the pyrolysis reaction process, including the time-scale of molecular product formation and the existence of metastable intermediates. Small carbohydrates are completely pyrolyzed within one second while glucose pyrolysis required only one-half second. In contrast, a surprising time delay of one second is observed for the thin-film pyrolysis of cellulose and α-cyclodextrin. The product yield distribution in the pyrolysis of various carbohydrates was compared with previous work,

and the difference was attributed to the reactor residence time, the presence of metastable intermediates, and identification difficulty in NIST library searches.

Introduction

Fast pyrolysis produces high yields of condensable vapors (bio-oils) which can be upgraded into drop-in fuels or commodity chemicals.[1-3] Fundamental understanding of fast pyrolysis is very limited despite three decades of research, mostly owing to the complexity of the pyrolysis process.[4] The kinetics of biomass pyrolysis has mostly been studied with global lump-sum models which ignore the chemical reactions of each molecular compound, leading to inconsistent kinetic parameters between measurements.[5] Recently, the Broadbelt group developed a mechanistic model for cellulose pyrolysis by dissecting pyrolysis reactions into hundreds of individual reaction steps.[6-8] This mechanistic approach provides predictive capabilities regarding the final product distribution and time evolution of each product. However, there are several critical limitations, including uncertainty of the proposed mechanisms and ambiguities in the Arrhenius rate parameters deduced from quantum mechanical calculations and fitting into experimental datasets. Furthermore, the model is built on idealistic situations without considering heating rate, phase transitions,[9] or aerosol formation/ejection[10] that occur in most experiments.

Some recent breakthrough technologies have dramatically improved our fundamental understanding of fast pyrolysis. Lédé and coworkers developed radiant flash pyrolysis using a focused xenon lamp, revealing the presence of non-volatile oligomers from immediately quenched intermediates.[11] Dauenhauer and coworkers used high-speed

photography to visualize aerosol ejection from boiling molten phase cellulose[9-10] and developed thin-film pyrolysis to study pyrolysis kinetics in isothermal conditions.[12] More recently, the Dauenhauer group developed a thermal pulsing reactor, called Pulse-Heated Analysis of Solid Reactions (PHASR), that can precisely control heating time within a millisecond timescale and analyze the product distributions with GC-MS.[13] This system was successfully applied to cellulose pyrolysis and demonstrated the size-dependence of reaction kinetics and temperature-dependent change of reaction mechanisms. Despite these recent technical advances, there currently is no tool available that can directly monitor each pyrolysis molecular product in real-time.

Here, we report an analytical platform to monitor each pyrolyzate in virtually real-time with sub-second temporal resolution. Combined with thin-film pyrolysis for isothermal kinetics conditions, we monitor the fast pyrolysis of a series of small carbohydrates (glucose, cellobiose, cellotriose, and cellotetraose). Additionally, fast pyrolysis of thin-film and powder of α-cyclodextrin and cellulose were studied to gain a better understanding of the size effect on reaction kinetics. Multiple insights were obtained from this study that could improve our fundamental understanding in biomass pyrolysis.

Experimental Section

Materials

Levoglucosan (1,6-anhydro-β-glucopyranose, Sigma-Aldrich, St. Louis, MO), glucose (Sigma-Aldrich), cellobiose (Fluka, St. Louis, MO), cellotriose (Carbosynth, San Diego, CA), cellotetraose (Santa Cruz Biotechnology, Dallas, TX), α-cyclodextrin

(Sigma-Aldrich), and cellulose (Sigmacell Type 20, Sigma-Aldrich) were purchased at the highest available purity. Isotopically-labeled $^{13}C_6$-levoglucosan (>99% ^{13}C atom) was purchased from Omicron Biochemicals (South Bend, IN) to serve as an internal calibrant.

Thin-film preparation

Samples were dissolved or suspended in water (Fluka LC-MS ChromaSolv) at a concentration of 1 mg mL^{-1}. Thin-films were prepared by transferring 0.5 µL of solution (0.5 µg sample loading) to the outside upper rim of 4 x 8 mm (diameter x height) cylindrical pyrolysis cups (Frontier) and placed under light house vacuum for 1 min to remove water. In all experiments, 0.05 µg of $^{13}C_6$-levoglucosan (0.5 µL of 0.1 mg mL^{-1} solution) was spotted on the opposite side of the sample cup as an internal standard. The ion signals of $^{13}C_6$-levoglucosan (*m/z* 186) was used to calibrate time-zero and quantify the amount of levoglucosan produced through pyrolysis. A good linearity was found for $^{13}C_6$-levoglucosan samples between 5-100 ng (R^2 = 0.995).

Metal contamination of raw materials

Sodium ion can leach from glass container at concentrations of 2-10 µM.[2] Mineral contaminations have been reported to affect fast pyrolysis product distributions at concentrations as low as 500 ppm (~0.05 wt%), particularly alkaline salts such as NaCl and KCl.[3] To minimize this effect, all samples were prepared in Teflon vials. Metal contaminants were quantified using inductively coupled plasma optical emission spectroscopy (ICP-OES; PerkinElmer Optima 8000; Waltham, MA) as shown in Table 1. All metal contaminations are present only in ignorable level. Cellulose was observed to have the highest concentrations of metal contaminants, which was further reduced by

washing with water and drying overnight at 35 °C. The washed cellulose was used for all subsequent experiments while all other samples were used as received.

Table 1. ICP-OES analysis results of metal contaminations in glucose-based carbohydrates used in the current study. Concentrations of inorganic ions are shown in ppb.

Sample	Na	K	Ca	Al	Mg
Levoglucosan	-	-	-	4.9	0.6
Glucose	-	-	1.7	3.2	0.5
Cellobiose	-	-	-	-	-
Cellotetraose	49.6	22.4	75.0	-	14.0
α-Cyclodextrin	-	-	7.8	1.6	2.9
Cellulose (unwashed)	780.1	233.2	57.2	44.7	7.9
Cellulose (washed)	25.6	-	20.4	-	4.8

* '-' indicates below the detection limit.

Real-time monitoring of thin-film pyrolysis

Experimental details can be found in Supplementary Information and briefly overviewed here as illustrated in Figure 1. A drop-in micropyrolyzer is mounted on a GC inlet and directly connected to a time-of-flight mass spectrometer (TOF MS) by a 0.6 m inert transfer line (photo with description in Figure S1). Samples are dropped via deactivated stainless steel cups into a preheated furnace to achieve extremely fast heating rates (>1,000,000 °C min^{-1}; ~5 ms to heat thin-films to 500 °C).[12] To achieve kinetically-limited isothermal condition,[12] we pyrolyze a thin-film (<5 μm) of material deposited on the sample cup surface in amounts as little as 50 ng. After arriving the bottom of the furnace, the thin-film is heated, pyrolyzed, and evaporated. Pyrolyzed vapors are carried

away by helium carrier gas to escape the reactor, and are delivered to the TOF MS. Each time component (T_{drop}, $T_{heating}$, $T_{pyrolysis}$, T_{evap}, and T_{escape} illustrated in Figure 1A) contributes to the total time that are being measured by TOF MS, as well as the dead time spent in the transfer line and TOF MS (T_{dead}). The transfer line is heated at 280 °C to avoid condensation. For a batch run of two consecutive thin-film levoglucosan, which is thermally stable and only evaporates at 500 °C, the time difference between the two peaks was very reproducible within 0.05 s (Figure 1B). This reproducibility allows us to calibrate T_{drop}, T_{escape} and T_{dead}, whereas $T_{heating}$ is ignorable for thin-film (~5 ms).[12] When the sample is loaded outside the cup on the top upper rim as a thin-film, the reactor residence time was found to be ~0.2 s, in contrast to ~0.6 s for a thin-film inside the bottom (Supplementary Info and Figure S2).

TOF MS is a fast-scanning, high resolution mass spectrometer which can trace each molecular product with accurate mass ($\Delta m \leq 10$ ppm). Pyrolysis products are ionized by dopant-assisted atmospheric pressure chemical ionization (dAPCI) with ammonia gas serving as a dopant,[14] which produces no fragmentation and dramatically increases ion signals mostly as ammonium adducts for highly oxygenated compounds (i.e., $[M+NH_4]^+$). Figure 1C shows the mass spectrum of thin-film pyrolysis of glucose as an example. Because of the high mass accuracy, we could directly determine the chemical compositions of all the peaks, as we have demonstrated the similar approach but with GC separation in catalytic pyrolysis of cellulose.[14] The C3 product ($C_3H_6O_3$, dihydroxyacetone and its structural isomers), half of glucose and the result of ring breakage, is most dominant, followed by similar amounts of $C_2H_4O_2$ (e.g., glycolaldehyde), $C_4H_8O_4$ (e.g., erythrose), and $C_6H_{10}O_5$ (levoglucosan and its structural

isomers). $^{13}C_6$-levoglucosan is also observed at *m/z* 186.107; this was deposited on the opposite side of the outer rim of sample cup from the glucose sample for the purpose of time calibration and quantification. Figure 1D shows the time profiles of a few representative pyrolysis products of glucose by tracing each peak with narrow mass window (±0.05 u). Here, the timescale is calibrated with the peak time of $^{13}C_6$-levoglucosan as time-zero, which, after calibration, corresponds to the pyrolysis time ($T_{pyrolysis}$) since it corrects for T_{drop}, T_{escape}, T_{dead}, $T_{heating}$, and T_{evap} (Figure 1A). It is possible that evaporation times might be slightly different for other pyrolyzates compared to levoglucosan, but we hypothesize the difference is ignorable at this high temperature.

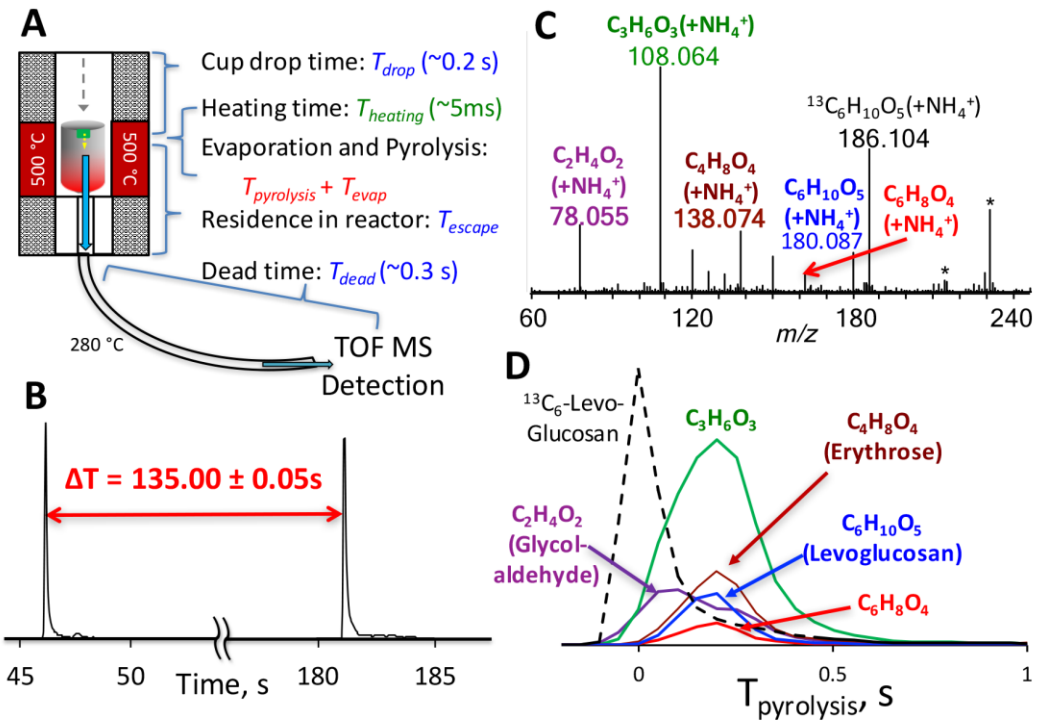

Figure1. Experimental overview of thin-film pyrolysis with subsecond time resolution. (A) Schematic diagram illustrating each time component contributing to the total measurement time. (B) Time difference between two consecutive runs of $^{13}C_6$-levoglucosan in batch mode is reproducible within 0.05 s. (C) Mass spectrum of thin-film glucose pyrolysis averaged over $T_{pyrolysis}$ of -0.2 to 1 s. (D) Time profiles of each product in thin-film pyrolysis of 0.5 µg glucose and 0.05 µg $^{13}C_6$-levoglucosan. *: Contamination peak.

Results and Discussion

Real-Time Monitoring in Fast Pyrolysis of Glucose-Based Carbohydrates

The temporal profiles for the thin-film pyrolysis of glucose shown in Figure 1D provide several key insights about the pyrolysis process. First, there are slight differences between the pyrolysis times of each reaction product. For example, ~0.1 s for $C_2H_4O_2$ and ~0.2 s for $C_3H_6O_3$, $C_4H_8O_4$, and $C_6H_{10}O_5$. The difference becomes clearer for larger carbohydrates (Figure 2) and suggests the pyrolysis reaction does not occur with the first-order kinetics even for simple glucose pyrolysis. This indicates a failure of the lump-sum model and confirms the need to understand each reaction at the molecular level as suggested by the Broadbelt group.[6-8] However, our experimental data do not agree with the Broadbelt model in fine detail. Glucose pyrolysis occurs much faster (<0.5 s) than predicted by them (>2 s) and some product yields do not match (further discussed later). The fact that the actual pyrolysis occurs much faster than predicted indicates many of the reaction parameters used in the Broadbelt model are either underestimated for frequency factors or overestimated for activation energies.

The shortcomings of the theoretical model are largely attributed to 1) the imperfection of the proposed reaction mechanisms (e.g., missing reactions[15]) and 2) incorrect reaction parameters. The latter is especially significant because many of the reaction parameters were obtained by fitting to experimental data from pyrolysis-GC-MS analysis of 200-500 μg of material. Such large amounts of powder piled inside the sample cup leads to the significant sample dimension of ~0.5 mm and result in non-isothermal kinetics,[12, 16] while isothermal kinetics are inherently assumed in the model. There will be a significant temperature gradient within the samples with non-isothermal kinetics both

for conductive[16] and convective heating.[17] It is known that isothermal thin-film pyrolysis dramatically reduces the levoglucosan yield compared to bulk pyrolysis (27 and 48 %C in thin-film and powder cellulose pyrolysis, respectively).[12, 16]

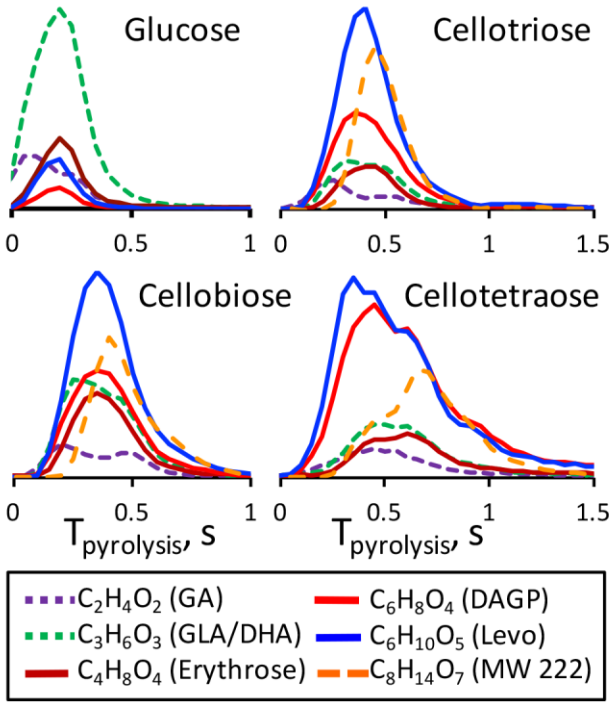

Figure 2. Time profiles of select products in thin-film pyrolysis of 0.5 μg glucose, cellobiose, cellotriose, and cellotetraose.

There also are other limitations in fitting theoretical modeling to pyrolysis-GC-MS data. Many of the pyrolysis products are not present in the EI-MS library and cannot be identified.[14] Furthermore, thermally unstable compounds cannot survive typical GC-MS condition and will not appear in the spectrum. For example, glyceraldehyde ($C_3H_6O_3$) is predicted in the reaction mechanism of Zhou et al.,[7] but not present in their experimental data. Hence, it is assumed to isomerize to dihydroxyacetone, the only compound with the chemical composition of $C_3H_6O_3$ in their experimental data but with

extremely low yield (0.11 %C). Glyceraldehyde is unstable at high temperatures and is difficult to detect with traditional GC-MS. However, thermally unstable pyrolysis products can be still detected in our instrumentation as long as they can survive for 0.2 s in the reactor at 500 °C and 0.3 s in the transfer line at 280 °C. High yields of $C_3H_6O_3$ in our data can be explained as mostly coming from glyceraldehyde before they further break into smaller products. Zhou et al. seems to have underestimated the overall reaction rate of glucose pyrolysis by ignoring the high primary yield of glyceraldehyde. We confirmed the presence of glyceraldehyde in glucose pyrolysis by adding a short GC separation in our instrumentation and comparing with the standards.[15]

To understand the influence of glycosidic bonds on reaction mechanisms, several glucose-based carbohydrates with various chain lengths were pyrolyzed and their temporal profiles are compared in Figure 2. In the pyrolysis of larger carbohydrates, levoglucosan ($C_6H_{10}O_5$) is much more abundant than $C_3H_6O_3$ due to the readily cleavable glycosidic bonds. In the pyrolysis of glucose, the only reaction pathway to form levoglucosan is a water loss which might be slow. As the chain length increases from glucose to cellotetraose, so does the broadening of temporal profile as well as the pyrolysis time. This is because for larger molecules it takes longer for thermal energy to be distributed as vibrational degree of freedom increases, and there are many more reactions competing with each other. The difference between pyrolysis times for each product is clearer for larger carbohydrates, but there is a change in the trend. For cellobiose pyrolysis, small products (C2, C3) are produced earlier with peak positions of 0.2-0.25 s and larger products (C6) appear later at the peak positions of ~0.35 s. For cellotetraose, however, the C6 products are observed at 0.35-0.45 s, similar to or slightly

earlier than small products appearing at 0.45-0.6 s. This suggests the presence of multiple mechanisms and increased contribution from glycosidic bond cleavage as the chain length increases. For example, bimodal distribution is observed for $C_2H_4O_2$ (mostly glycolaldehyde), which can be produced either by directly breaking the glucose ring appearing earlier or consecutively after glycosidic bond cleavage.

The presence of the C8 compound, $C_8H_{14}O_7$, in the pyrolysis of cellobiose or larger carbohydrates is quite interesting, which has not been reported in any pyrolysis-GC-MS studies. This compound must be thermally unstable and would not survive typical Py-GC-MS conditions. We could not find this product when we ran μPy-GC-dAPCI-TOF experiments by attaching a GC column to our system (Figure S3). Hurt et al. have detected this compound in on-line pyrolysis MS of cellobiose.[18] They used a fast heating pyroprobe in an APCI interface to directly inject early pyrolysis products to an ion trap MS. This approach is complementary to our system, as they can detect early pyrolysis products with a life time shorter than ~0.2 s but cannot accurately monitor their time evolution because of significant heating lag (0.5 s to heat up to 500 °C). They observed $C_8H_{14}O_7$ as the most abundant product, and determined its structure to be glucopyranosylglycolaldehyde from the combined study of MS/MS, pyrolysis of ^{13}C-labeled cellobiose, and quantum chemical calculation.[19] The production of this compound can be explained as two consecutive retro aldol reactions, losing two glycolaldehydes as shown in Scheme 1. Unlike other products, $C_8H_{14}O_7$ appears after ~0.2 s of time delay rather than immediately (Figure 2), which is the characteristic of consecutive reactions and agrees with Scheme 1. As a consequence, its pyrolysis peak time also appears later than the others. Glycolaldehydes produced in the first and the second reactions of Scheme

1 have different time scales, as well as another glycolaldehyde produced for the conversion of $C_8H_{14}O_7$ to levoglucosan (the third reaction in Scheme 1), contributing to the bimodal distribution of glycolaldehyde and the shift of the average pyrolysis time in Figure 2.

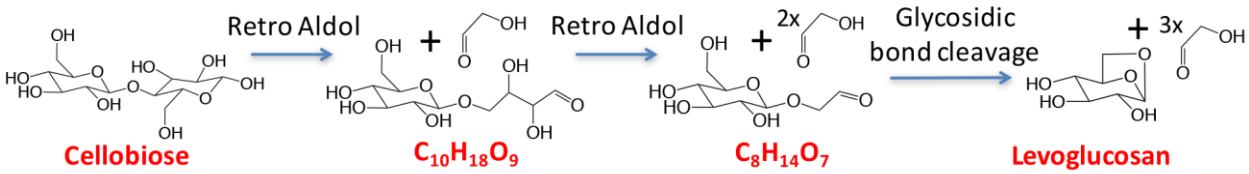

Scheme 1. Pyrolysis reaction pathway to yield $C_8H_{14}O_7$ and its decomposition to levoglucosan.

Quantitative Product Yields in Fast Pyrolysis of Glucose-based Carbohydrates

Product yields are difficult to measure accurately in our experiment because the ionization efficiency of each product is unknown and subject to experimental conditions. We tried several different methods to calibrate ionization efficiencies, such as comparing TOF MS to catalytic conversion FID[20] with GC separation for standard samples or the pyrolysis products of glucose and cellulose. Unfortunately, we could not obtain reliable calibration due to the low signals and peak overlap in GC-FID and run-to-run variation with minute sample amount. From this set of experiments, it was consistent that the ionization efficiencies of small products are lower than that of levoglucosan. For example, $C_3H_6O_3$ (glyceraldehyde and its structural isomers) has an ionization efficiency in the range of 10-45% of levoglucosan. The efficiency for ammonium adduct formation is mostly affected by the molecular size and ammonium ion affinity in dAPCI conditions. As the zeroth approximation, we hypothesized the ionization efficiency is proportional to

the number of carbons (as a measure of molecular size) as well as the number of oxygens (as a measure of ammonium ion affinity) in the pyrolysis product, which is then compared to that of levoglucosan. For example, the ionization efficiency of $C_3H_6O_3$ is approximated to be 30% of levoglucosan.

As levoglucosan does not pyrolyze but only evaporates, the absolute quantification can be made with the standard either externally or internally. The calibration curve was made with $^{13}C_6$-levoglucosan for the amount of 5-100 ng (R^2 = 0.995) and used to calculate the levoglucosan yield. Then, the yields of other pyrolyzates were calculated from the above approximation in ionization efficiencies. Internal and external calibration agree with each other, but external calibration was less susceptible to the experimental errors. Table 2 shows the carbon yield of major products in thin-film pyrolysis of glucose and its oligomers obtained by our direct real-time monitoring, compared with thin-film pyrolysis and powder pyrolysis in the literature obtained by GC-FID/MS.[7, 12, 21] It should be noted that our carbon yields have systematic errors due to the assumption made for ionization efficiency, except for levoglucosan, and but the trends for a series of carbohydrates should still hold for the same chemical compound. All three experiments used the same type of micropyolyzers, a single shot pyrolyzer from Frontier Laboratories (Model 2020S for Mettler et al. and Zhou et al., and Model 3030S for ours), but there was significant difference in the sample amount: only 0.5 μg by us and ≥ 200 μg by others. The most significant difference is the reactor residence time, 0.2 s in ours vs ~0.6 s in others (explained in Figure S2). Additionally, other experiments experience the loss of non-volatile and unstable products (Table 2 and Figure S3). Thin-film pyrolysis occurs in isothermal kinetics conditions, whereas the sample dimension is

known to greatly affect the product distribution in powder pyrolysis, as discussed in the previous section.

Levoglucosan ($C_6H_{10}O_5$) yield is low in the pyrolysis of glucose but increases as the chain length in all experiments shown in Table 2; 2.1 to 20.1 %C in our data, 5.6 to 28.4 %C in thin-film pyrolysis by Mettler et al., and 13.7 to 57.3 %C in powder pyrolysis by Zhou et al. This trend is quantitatively well correlated between the two thin-film pyrolysis data, except for the pyrolysis of α-cyclodextrin (7.8 versus 25.5 %C). Mettler et al. found close correlation in the product yields of thin-film pyrolysis between α-cyclodextrin and cellulose, and suggested α-cyclodextrin could be used as a surrogate of cellulose pyrolysis.[12] However, we find some difference in the yields of larger products, such as levoglucosan, $C_6H_8O_4$ and $C_8H_{14}O_7$. This indicates that the pyrolysis of α-cyclodextrin is slightly different from cellulose in the first sub-second. With a longer reactor residence time in Mettler et al., ~0.6 s instead of ~0.2 s, $C_8H_{14}O_7$ or other larger intermediates would decompose into levoglucosan (Scheme 1), which will be further discussed in the next section.

Table 2. Carbon yield (in percent initial carbon) in the pyrolysis of glucose and its oligomers[a].

Chemical Composition[b]	Thin-film pyrolysis: This work / Mettler et al.[12, 21]						Powder pyrolysis: Zhou et al.[7]	
	Glucose	Cellobiose	Cellotriose	Cellotetraose	α-Cyclodextrin	Cellulose	Glucose	Cellulose
$C_2H_4O_2$	7.8 (1.6) 6.7 (0.6)	7.2 (0.7) 5.8	4.8 (0.2) 6.4	7.2 (1.8) 5.9	6.9 (0.8) 8.8 (0.8)	5.7 (0.8) 8.5 (0.4)	4.3	5.5
$C_3H_6O_3$	16.6 (1.7) -	7.8 (1.0) -	5.2 (0.5) -	3.6 (0.2) -	2.0 (0.2) -	1.3 (0.3) -	0.11	0.05
$C_4H_6O_3$	2.8 (0.2) -	7.7 (0.4) -	7.8 (1.0) -	7.8 (0.7) -	8.8 (0.7) -	4.0 (0.4) -	0.14	0.08
$C_5H_6O_3$	1.1 (0.2) -	1.8 (0.1) -	2.2 (0.2) -	2.6 (0.2) -	3.5 (0.5) -	2.2 (0.4) -	0.26	0.62
$C_4H_8O_4$	2.6 (1.2) -	4.7 (0.8) -	2.3 (1.2) -	1.8 (0.3) -	0.8 (0.3) -	0.4 (0.3) -	-	-
$C_6H_6O_3$	0.4 (0.1) 12 (1)	1.6 (0.4) 15.3	2.4 (0.3) 13.5	2.6 (0.4) 10.5	5.3 (0.8) 4.0 (0.2)	4.6 (1.3) 4.2 (0.1)	7.9	1.5
$C_5H_8O_4$	2.0 (0.4) -	1.5 (0.1) -	1.5 (0.3) -	1.1 (0.1) -	0.8 (0.1) -	0.7 (0.2) -	-	-
$C_6H_8O_4$	1.0 (0.3) 1.6	5.8 (1.0) 2.6	7.8 (1.3) 3.0	8.4 (0.6) 3.7	15.1 (1.8) 7.9	7.3 (1.0) 5.9	0.56	7.4
$C_6H_{10}O_5$	2.1 (0.6) 5.6 (1.1)	8.3 (1.7) 9.7	9.3 (2.1) 9.4	7.3 (1.0) 9.1	7.8 (1.6) 25.5 (1.0)	20.1 (2.8) 28.4 (2.0)	13.7	57.3
$C_8H_{14}O_7$	0.03 (0.03) -	3.5 (0.2) -	4.0 (0.8) -	2.5 (0.8) -	3.3 (0.7) -	0.8 (0.2) -	-	-
$C_{12}H_{20}O_{10}$	- -	0.04 (0.01) -	0.07 (0.02) -	0.07 (0.09) -	0.15 (0.07) -	0.39 (0.32) -	-	-

a. Our %C yield is calculated assuming the ionization efficiency is proportional to the product of the number of carbons and the number of oxygens, normalized to the ionization efficiency of levoglucosan that was externally calibrated. The wt % data of Zhou et al. was converted to %C yield. The numbers in the parenthesis is 90% confidence interval.

b. Our study cannot distinguish structural isomers, but can directly determine chemical compositions. For the data of others, pyrolysis products with the same chemical composition were summed together. Following is the known representative products for each chemical composition, ignoring positional isomers: $C_2H_4O_2$, glycolaldehyde, acetic acid; $C_3H_6O_3$, glyceraldehyde, dihydroxyacetone; $C_5H_6O_3$, dianhydroxylose; $C_4H_8O_4$, erythrose; $C_6H_6O_3$, hydroxymethylfurfural, levoglucosenone; $C_6H_8O_4$, dianhydroglucopyranose; $C_6H_{10}O_5$, levoglucosan; $C_8H_{14}O_7$, glucopyranosyl-glycolaldehyde; $C_{12}H_{20}O_{10}$, cellobiosan.

The smallest product we can detect, $C_2H_4O_2$, shows similar yield between the two thin-film pyrolysis experiments. It is mostly glycolaldehyde, although acetic acid is also present with a much lower yield. The agreement is remarkable in spite of very rough correction for the ionization efficiency, and they both have minimal change as the chain length. The effect of the reactor residence time seems to have minimal impact in this case. The longer residence may result in the decomposition of some glycolaldehyde to one carbon products such as carbon monoxide; however, such a loss might be supplemented by the breakdown of intermediate compounds such as $C_8H_{14}O_7$ in Scheme 1.

The yield for $C_6H_6O_3$ agrees relatively well between the two thin-film pyrolysis for α-cyclodextrin and cellulose, but Mettler et al. shows much higher yields for small oligosaccharides (10.5-15 %C compared to 0.4-2.6 %C in ours). It might be related with the reaction mechanism. The major structural isomer of $C_6H_6O_3$, hydroxymethylfurfural (HMF), can be produced through the isomerization to linear structure[7] or glycosidic bond cleavage.[12] The former mechanism is expected to be dominant for glucose and small carbohydrates (i.e., ring opening at the end chain) and slow as it requires rearrangement. In contrast, the latter mechanism is expected to be dominant for α-cyclodextrin and cellulose and faster as it is initiated by the direct glycosidic bond cleavage. This is in agreement with Table 2 in that the reactor residence time has minimal effect for the fast reaction in α-cyclodextrin and cellulose, but makes a difference for the slow reaction in small oligosaccharides, especially low yields for the short reactor residence time.

Some chemical compounds are uniquely observed in our dataset, such as $C_3H_6O_3$, $C_4H_6O_3$, and $C_4H_8O_4$. It is attributed to the instability of these compounds and/or absence

in NIST EI-MS library. We could detect these compounds and determine their chemical compositions thanks to a short reactor residence time, soft dAPCI ionization, and high-resolution MS measurement. $C_4H_6O_3$ is recognized in the data set of Zhou et al. as an unknown compound with MW of 102. The yield for $C_3H_6O_3$ dramatically decreases from 16.6 to 1.3 %C as the contribution from glycosidic bond increases. The major primary product of $C_3H_6O_3$ is glyceraldehyde, which is unstable at high temperatures and easily breaks into smaller products with a longer reactor residence time.[15] Most of the product yields in powder pyrolysis are quite different from thin-film pyrolysis, but general trend between glucose and cellulose pyrolysis mostly agrees with thin-film pyrolysis by Mettler et al. For example, the yield increases for levoglucosan ($C_6H_{10}O_5$) and dianhydroglucose ($C_6H_8O_4$) and decreases for hydroxymethylfurfural ($C_6H_6O_3$) as the chain length.

Real-Time Monitoring of α-Cyclodextrin and Cellulose

The most dramatic result was found when we pyrolyzed thin-film cellulose and thin-film α-cyclodextrin, as shown in Figure 3. For both cellulose and α-cyclodextrin, no products appear for the first second, then each pyrolysis product shows up with relatively similar temporal profiles. This time delay is unique to cellulose and α-cyclodextrin, and is not found in small carbohydrates (Figure 2). Cellulose and α-cyclodextrin have no or few end-chains unlike other small carbohydrates and are composed mostly of glycosidic bonds. Cellulose has a crystalline structure with strong hydrogen bonding between cellulose molecules and α-cyclodextrin is known to crystallize from water as a hexahydrate with interlocking hydrogen bonding.[22] We hypothesize that this network of hydrogen bonding needs to be broken apart, or "zipped off", along with partial mid-chain

breakages to transform to an intermediate state, which corresponds to "active cellulose"[23] or molten phase,[9] before volatile pyrolyzates are produced. The lack of distinct differences between the temporal profiles might be due to the fact that their detection is not limited by reaction kinetics but rather vaporization or escape from the molten phase. Some peak fluctuations, especially in the pyrolysis of larger amounts, are attributed to mostly coming from the aerosol ejections,[9-10] which are not reproducible between runs.

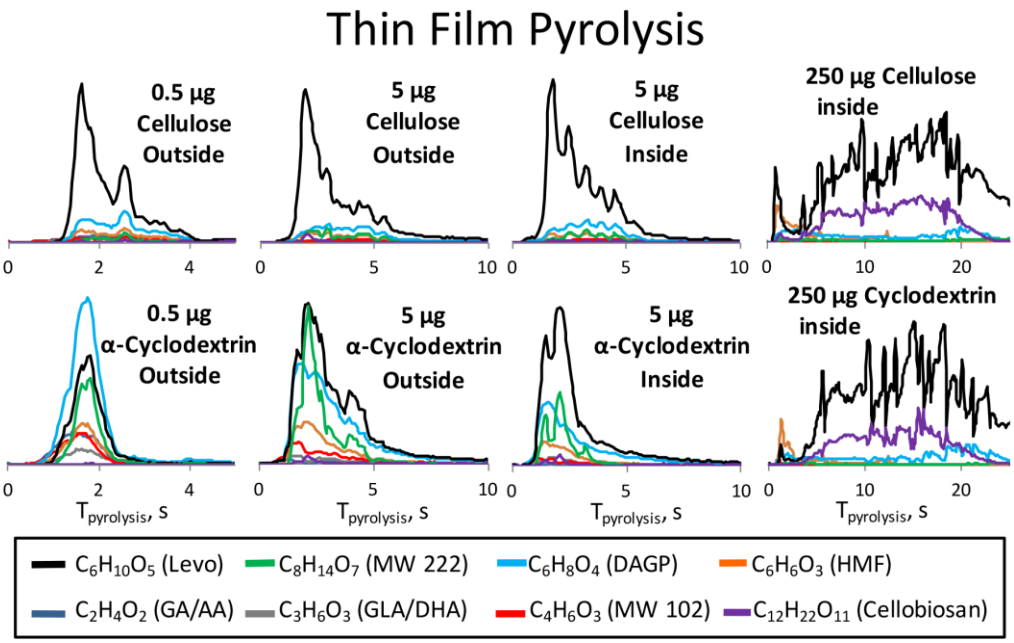

Figure 3. Temporal profiles in various amounts of thin-film pyrolysis of cellulose (top) and α-cyclodextrin (bottom). "Outside" indicates thin-film deposited on the top outer rim of sample cups and "Inside" indicates thin-film deposited at the bottom inside of sample cups.

Despite both carbohydrates having the same time delay of one second, the relative product yields are quite different between cellulose and α-cyclodextrin. Especially when small amounts are deposited on the outside of the sample cup (left four figures in Figure 1), much higher yields of dianhydroglucopyranose ($C_6H_8O_4$) and intermediate product

($C_8H_{14}O_7$) are observed in α-cyclodextrin compared to cellulose. This is in contrast to Mettler et al.,[12] where α-cyclodextrin was suggested as a surrogate for cellulose pyrolysis considering the similarity in product distribution in thin-film pyrolysis. It is, again, attributed to the reactor residence time difference. For example, intermediate product ($C_8H_{14}O_7$) in thin-film pyrolysis of α-cyclodextrin might further break apart to yield levoglucosan ($C_6H_{10}O_5$) when subjected to sufficient reactor residence time. In fact, when thin-film of α-cyclodextrin is pyrolyzed inside the cups (right four figures in Figure 2), much less intermediate product is observed and the product distribution is more similar between α-cyclodextrin and cellulose. Powder pyrolysis inside the sample cup also shows similarity between cellulose and α-cyclodextrin (Figure S4). As the amount of material increases, it takes longer for pyrolysis to complete for both thin-film and powder. The overall pyrolysis time (>20 s) for a large amount of sample (250 μg) is attributed to the inefficient heating of unpacked particles[16] and/or the longer time necessary for the pyrolyzates to escape from the molten phase. It should be noted, however, that the actual pyrolysis time of this dimension in pilot scale reactors, such as fluidized bed reactors, would not be as much significant because conduction heating is three-dimensional in those situations rather than one-dimensional as in the current study.

Cellobiosan ($C_{12}H_{20}O_{10}$) is non-volatile and cannot be observed in typical GC-MS or Py-GC-MS analysis, unless volatilized through off-line derivatization,[10] but is observed in our dataset for large carbohydrates (Table 2). The yield for cellobiosan is highest with α-cyclodextrin and cellulose, and increases significantly when a large amount of materials are pyrolyzed for both thin-film and powder pyrolysis (Figure 3 and Figure S4). Since it is non-volatile, cellobiosan is unable to escape the reactor through

vaporization but must be a result of aerosol ejection.[9-10] This indicates another advantage of this instrumentation since it has the capability to detect non-volatile compounds in addition to unstable intermediates.

Conclusions

We have developed a new analytical platform that can monitor the molecular products in the fast pyrolysis of biomass in almost real-time. Several new insights have been obtained by applying it to the pyrolysis of glucose-based carbohydrates. The major findings include: 1) the pyrolysis of small carbohydrates occurs much faster than previously expected, as little as one-half second for glucose pyrolysis, 2) the existence of "metastable" intermediates was confirmed that was previously reported by Hurt et al. in the pyrolysis of cellobiose under ambient condition,[18] 3) one second of significant time delay was observed in thin-film pyrolysis of cellulose and α-cyclodextrin, which was attributed to the transition to molten phase, and 4) significant difference is observed in the distribution of product yields between ours and Mettler et al., and explained mostly coming from the difference in reactor residence time. With the advent of this and other modern technological developments, we envision a full fundamental understanding of the complex biomass pyrolysis would become possible in the near future that will lead to the better control of the product yield distributions.

Acknowledgements

This work is supported by National Science Foundation, Division of Chemical, Bioengineering, Environmental and Transport Systems, Energy for Sustainability Program.

References

1. Bridgwater, A. V., Review of fast pyrolysis of biomass and product upgrading. *Biomass & Bioenergy* **2012,** *38*, 68-94.

2. Huber, G. W.; Iborra, S.; Corma, A., Synthesis of transportation fuels from biomass: Chemistry, catalysts, and engineering. *Chem. Rev.* **2006,** *106* (9), 4044-4098.

3. Vispute, T. P.; Zhang, H.; Sanna, A.; Xiao, R.; Huber, G. W., Renewable Chemical Commodity Feedstocks from Integrated Catalytic Processing of Pyrolysis Oils. *Science* **2010,** *330* (6008), 1222-1227.

4. Mettler, M. S.; Vlachos, D. G.; Dauenhauer, P. J., Top ten fundamental challenges of biomass pyrolysis for biofuels. *Energy Environ. Sci.* **2012,** *5* (7), 7797-7809.

5. Burnham, A. K.; Zhou, X.; Broadbelt, L. J., Critical Review of the Global Chemical Kinetics of Cellulose Thermal Decomposition. *Energy Fuels* **2015,** *29* (5), 2906-2918.

6. Vinu, R.; Broadbelt, L. J., A mechanistic model of fast pyrolysis of glucose-based carbohydrates to predict bio-oil composition. *Energy Environ. Sci.* **2012,** *5* (12), 9808-9826.

7. Zhou, X.; Nolte, M. W.; Mayes, H. B.; Shanks, B. H.; Broadbelt, L. J., Experimental and Mechanistic Modeling of Fast Pyrolysis of Neat Glucose-Based Carbohydrates. 1. Experiments and Development of a Detailed Mechanistic Model. *Ind. Eng. Chem. Res.* **2014,** *53* (34), 13274-13289.

8. Zhou, X.; Nolte, M. W.; Shanks, B. H.; Broadbelt, L. J., Experimental and Mechanistic Modeling of Fast Pyrolysis of Neat Glucose-Based Carbohydrates. 2. Validation and Evaluation of the Mechanistic Model. *Ind. Eng. Chem. Res.* **2014,** *53* (34), 13290-13301.

9. Dauenhauer, P. J.; Colby, J. L.; Balonek, C. M.; Suszynski, W. J.; Schmidt, L. D., Reactive boiling of cellulose for integrated catalysis through an intermediate liquid. *Green Chemistry* **2009,** *11* (10), 1555-1561.

10. Teixeira, A. R.; Mooney, K. G.; Kruger, J. S.; Williams, C. L.; Suszynski, W. J.; Schmidt, L. D.; Schmidt, D. P.; Dauenhauer, P. J., Aerosol generation by reactive boiling ejection of molten cellulose. *Energy & Environmental Science* **2011,** *4* (10), 4306-4321.

11. Lede, J.; Blanchard, F.; Boutin, O., Radiant flash pyrolysis of cellulose pellets: products and mechanisms involved in transient and steady state conditions. *Fuel* **2002,** *81* (10), 1269-1279.

12. Mettler, M. S.; Mushrif, S. H.; Paulsen, A. D.; Javadekar, A. D.; Vlachos, D. G.; Dauenhauer, P. J., Revealing pyrolysis chemistry for biofuels production: Conversion of cellulose to furans and small oxygenates. *Energy Environ. Sci.* **2012,** *5* (1), 5414-5424.

13. Krumm, C.; Pfaendtner, J.; Dauenhauer, P. J., Millisecond Pulsed Films Unify the Mechanisms of Cellulose Fragmentation. *Chem. Mater.* **2016,** *28* (9), 3108-3114.

14. Cole, D. P.; Lee, Y. J., Effective evaluation of catalytic deoxygenation for in situ catalytic fast pyrolysis using gas chromatography–high resolution mass spectrometry. *J. Anal. Appl. Pyrolysis* **2015,** *112*, 129-134.

15. Hutchinson, C. P.; Lee, Y. J., Evaluation of Primary Reaction Pathways in Thin-Film Pyrolysis of Glucose Using 13C Labeling and Real-Time Monitoring. *submitted*.

16. Paulsen, A. D.; Mettler, M. S.; Dauenhauer, P. J., The Role of Sample Dimension and Temperature in Cellulose Pyrolysis. *Energy Fuels* **2013,** *27* (4), 2126-2134.

17. Zhang, J.; Nolte, M. W.; Shanks, B. H., Investigation of Primary Reactions and Secondary Effects from the Pyrolysis of Different Celluloses. *Acs Sustainable Chemistry & Engineering* **2014,** *2* (12), 2820-2830.

18. Hurt, M. R.; Degenstein, J. C.; Gawecki, P.; Borton Ii, D. J.; Vinueza, N. R.; Yang, L.; Agrawal, R.; Delgass, W. N.; Ribeiro, F. H.; Kenttämaa, H. I., On-Line Mass Spectrometric Methods for the Determination of the Primary Products of Fast Pyrolysis of Carbohydrates and for Their Gas-Phase Manipulation. *Anal. Chem.* **2013,** *85* (22), 10927-10934.

19. Degenstein, J. C.; Murria, P.; Easton, M.; Sheng, H.; Hurt, M.; Dow, A. R.; Gao, J.; Nash, J. J.; Agrawal, R.; Delgass, W. N.; Ribeiro, F. H.; Kenttaemaa, H. I., Fast Pyrolysis of C-13-Labeled Cellobioses: Gaining Insights into the Mechanisms of Fast Pyrolysis of Carbohydrates. *J. Org. Chem.* **2015,** *80* (3), 1909-1914.

20. Maduskar, S.; Teixeira, A. R.; Paulsen, A. D.; Krumm, C.; Mountziaris, T. J.; Fan, W.; Dauenhauer, P. J., Quantitative carbon detector (QCD) for calibration-free, high-resolution characterization of complex mixtures. *Lab on a Chip* **2015,** *15* (2), 440-447.

21. Mettler, M. S.; Paulsen, A. D.; Vlachos, D. G.; Dauenhauer, P. J., The chain length effect in pyrolysis: bridging the gap between glucose and cellulose. *Green Chem.* **2012,** *14* (5), 1284-1288.

22. Klar, B.; Hingerty, B.; Saenger, W., TOPOGRAPHY OF CYCLODEXTRIN INCLUSION COMPLEXES .12. HYDROGEN-BONDING IN THE CRYSTAL-STRUCTURE OF ALPHA-CYCLODEXTRIN HEXAHYDRATE - THE USE OF A MULTICOUNTER DETECTOR IN NEUTRON-DIFFRACTION. *Acta Crystallogr. Sect. B-Struct. Commun.* **1980,** *36* (MAY), 1154-1165.

23. Shafizadeh, F.; Chin, P. P. S., THERMAL DETERIORATION OF WOOD. *Abstracts of Papers of the American Chemical Society* **1976,** *172* (SEP3), 37-37.

Supporting Information

Micropyrolysis-dopant-assisted APCI-TOF MS

Thin-film pyrolysis was conducted using a micropyrolyzer-time-of-flight mass spectrometer shown in Figure S1. Samples were pyrolyzed using a drop-in microfurnace pyrolyzer (AS-1020E auto shot sampler and 3030S micropyrolyzer; Frontier Laboratories, Fukushima, Japan) with a preheated furnace temperature of 500 °C. Pyrolysis vapors are transported by ultrahigh purity helium carrier gas at a flow rate of 1 mL min^{-1} through a short deactivated fused silica transfer line (0.6 m; SGE Incorporated, Pflugerville, TX) with the GC oven (Agilent 7890A, Palo Alto, CA) temperature set at 280 °C to prevent condensation. Products were ionized by dopant-assisted atmospheric pressure ionization (dAPCI) and detected using a high-resolution Agilent 6200 TOF MS ($m/\Delta m$ ~7,000 at *m/z* 200) scanning over a mass range of *m/z* 60-1000 at a scan speed of 20 Hz (0.05 s per spectra).

APCI is a soft ionization technique commonly used for LC-MS but produces significant fragmentation when coupled with a GC interface. We use ammonia gas as a dopant to improve sensitivity and minimize fragmentation, as previously described.[1] Briefly, preheated ammonia (500 ppm in He; Praxair, Dansbury, CT) flows into the source chamber at 1 mL min^{-1} as a sheath gas and is introduced to APCI ion source interface. Ammonium ions formed by corona discharge (1 kV) ionize analytes through ammonium adduct formation for carbohydrate-type compounds, forming a stable adduct ion with almost no fragmentation. Humidity influences ion signals, especially in winter time when lab air is very dry, and a humidity control setup was used to by infusing N_2-bubbled water vapor into the source at 1:1 ratio with dry N_2 (not shown in Figure 1).

Multiple samples were run as a batch mode with 0.1 min run time each. The time difference between levoglucosan peak maxima is very reproducible (Δt = 135.00 s) when two consecutive sample cups of thin-film levoglucosan were dropped in batch mode. The time error is minimal (± 0.05 s) and simply comes from the TOF MS scanning time. The extra 129 s is due to the dead time for the communication between autosampler, mass spectrometer, and computer, as well as the preparation time for the autosampler, including ejecting the used sample cup; however, this time is very reproducible.

Measurement of reactor residence time

To estimate the residence time of pyrolysis vapor inside the reactor, two consecutive cups of thin-film levoglucosan was dropped into the furnace in batch mode using an autosampler, with the thin-film deposited on the top outside rim for the first sample and on various positions for the second (Figure S2). We expect almost no reactor residence time for the sample deposited at the bottom of the cup, because we observed no pyrolysis product when glucose is deposited at the bottom of the cup (data not shown). Compared to levoglucosan deposited at the bottom position (Figure S2A), it takes 0.2 s longer when the second one is deposited at the top outside rim of the cup (Figure S2B), suggesting the reactor residence time is ~0.2 s at the position. In contrast, when levoglucosan thin-film is deposited inside the cup at the bottom, the time profile is significantly broader, ~0.6 s compared to ~0.2 s, and it takes average of ~0.6 s to escape the reactor (Figure S2C). The broadening in temporal profiles for the sample inside the cup is attributed to gas turbulence for the carrier gas to carry away pyrolyzates. All our experiments, unless otherwise noted, were performed with a thin-film of 0.5 μg materials

deposited on the outer top corner of sample cup and expected to have the reactor residence time of ~0.2 s.

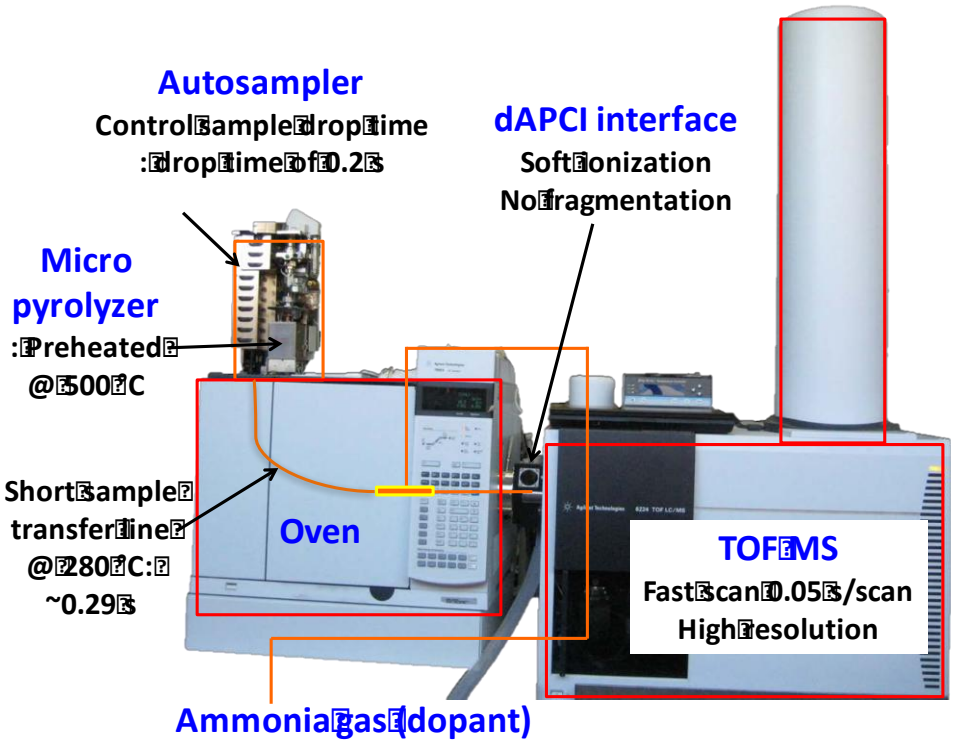

Figure S1. Micropyrolyzer-dAPCI-TOF MS system with a short description for each compartment.

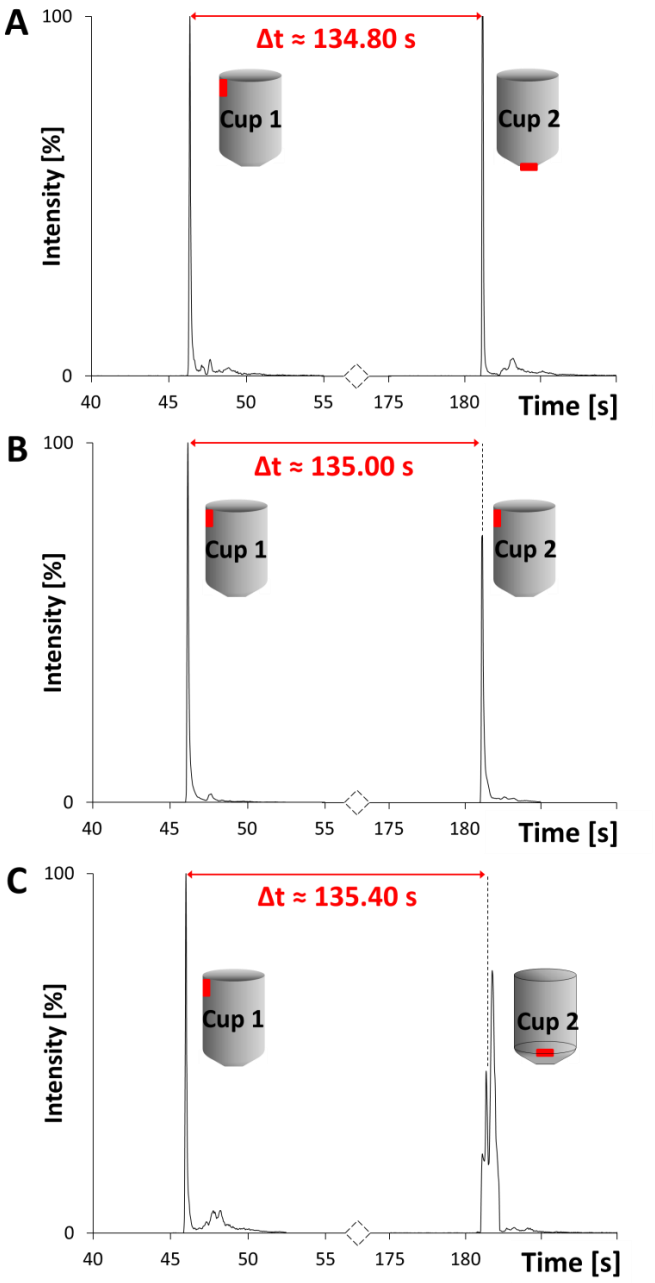

Figure S2. The elution time changes depending on the thin-film positions. The extracted ion chromatograms (EICs) of isotopically-labeled $^{13}C_6$-levoglucosan ($[^{13}C_6H_{10}O_5+NH_4]^+$, *m/z* 186.107) in thin-film pyrolysis at 500 °C with the spotting location (red mark) of cup 2 as **(A)** outside bottom, **(B)** outside upper rim, and **(C)** inside bottom. The time difference (Δt) is calculated by peak maximum except for **(C)**, which is peak area center due to peak broadening and irregularity.

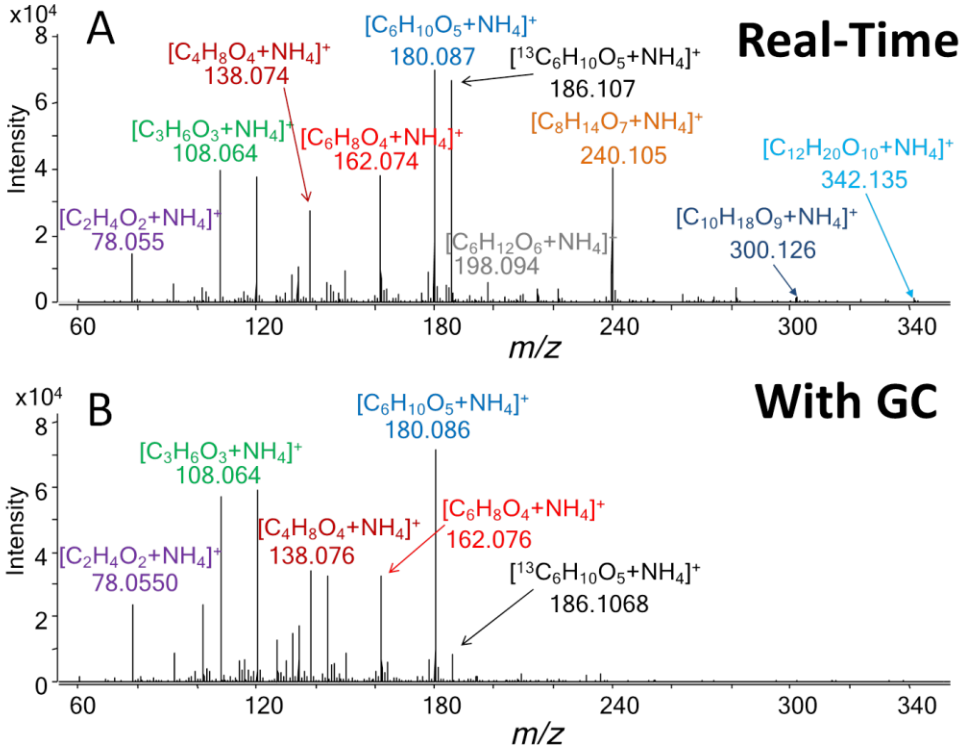

Figure S3. Summed mass spectra of cellobiose fast pyrolysis without and with GC separation. Non-volatile and/or unstable products ($C_8H_{14}O_7$, $C_{10}H_{18}O_9$, $C_{12}H_{20}O_{10}$) are missing with GC.

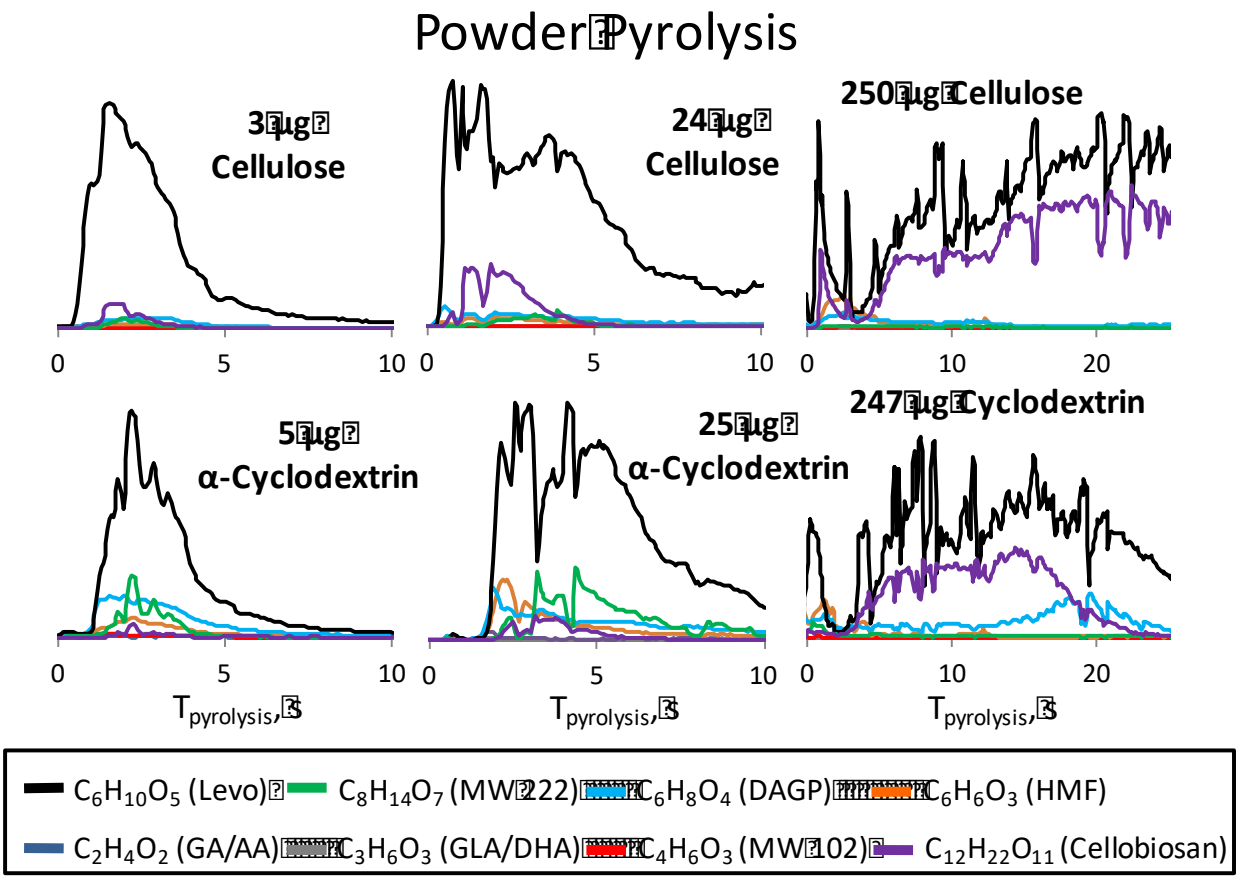

Figure S4. Temporal profiles of powder pyrolysis of various amounts of cellulose (top) and α-cyclodextrin (bottom). All samples were placed inside the cups.

References

1. Cole, D. P.; Lee, Y. J., Effective evaluation of catalytic deoxygenation for in situ catalytic fast pyrolysis using gas chromatography–high resolution mass spectrometry. *J. Anal. Appl. Pyrolysis* **2015,** *112*, 129-134.

2. Gao, S.; Zhang, Z.-P.; Karnes, H. T., Sensitivity enhancement in liquid chromatography/atmospheric pressure ionization mass spectrometry using derivatization and mobile phase additives. *J. Chromatogr. B* **2005,** *825* (2), 98-110.

3. Patwardhan, P. R.; Satrio, J. A.; Brown, R. C.; Shanks, B. H., Influence of inorganic salts on the primary pyrolysis products of cellulose. *Bioresour. Technol.* **2010,** *101* (12), 4646-4655.

4. Hurt, M. R.; Degenstein, J. C.; Gawecki, P.; Borton Ii, D. J.; Vinueza, N. R.; Yang, L.; Agrawal, R.; Delgass, W. N.; Ribeiro, F. H.; Kenttämaa, H. I., On-Line Mass Spectrometric Methods for the Determination of the Primary Products of Fast Pyrolysis of Carbohydrates and for Their Gas-Phase Manipulation. *Anal. Chem.* **2013,** *85* (22), 10927-10934.

5. Degenstein, J. C.; Murria, P.; Easton, M.; Sheng, H.; Hurt, M.; Dow, A. R.; Gao, J.; Nash, J. J.; Agrawal, R.; Delgass, W. N.; Ribeiro, F. H.; Kenttaemaa, H. I., Fast Pyrolysis of C-13-Labeled Cellobioses: Gaining Insights into the Mechanisms of Fast Pyrolysis of Carbohydrates. *J. Org. Chem.* **2015,** *80* (3), 1909-1914.